eman ta zabal zazu

UPV EHU

Magnetic properties of Co on different environments

Iker Gallardo

PhD THESIS

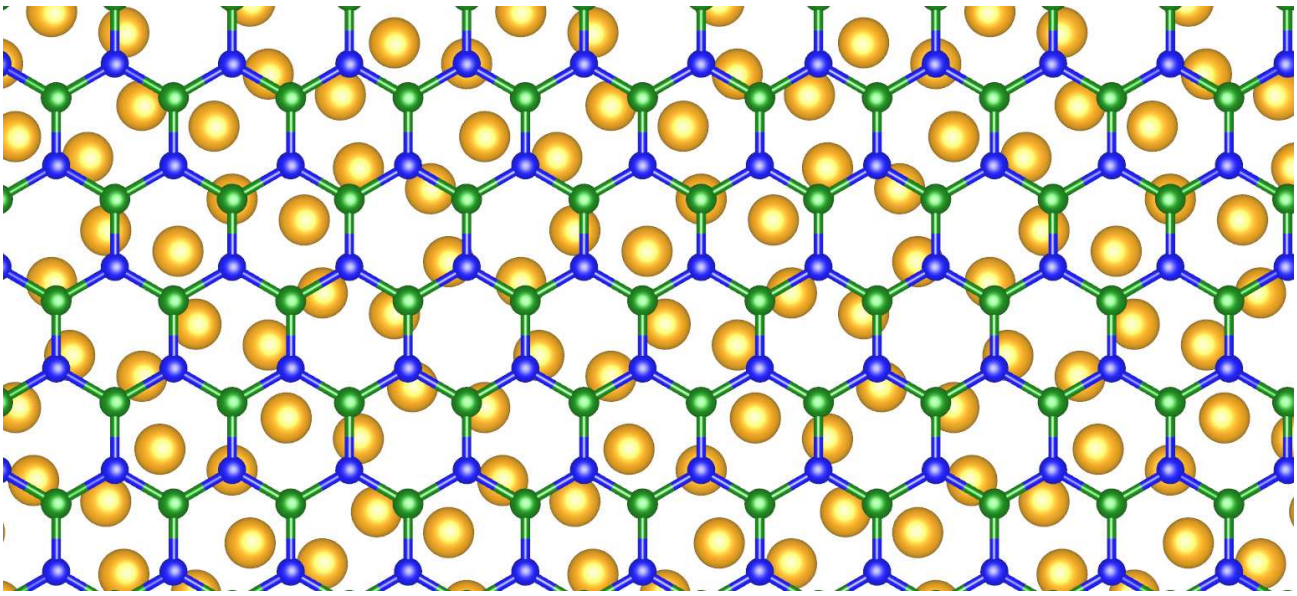

Thesis supervisors:

Prof. Andres Arnau Pino **Dr. Fernando Delgado Acosta**

2019

Acknowledgments

En primer lugar me gustaría mostrar mi más sincera gratitud a mis dos directores, Andres Arnau Pino y Fernando Delgado Acosta. Ha sido un verdadero privilegio tener la oportunidad de aprender y trabajar con dos grandes pérsonas y científicos como vosotros.

En segundo lugar, y como no podría ser de otra forma, tengo que agradecer enormemente a mi familia todo el apoyo incondicional dado durante este tiempo, y en particular a mis padres, Marga y Maxi, por todo el esfuerzo que han realizado para que pueda estar donde estoy.

Then, I would like to thanks Dr. Moritz Müller, who appeared and picked me up in the worst period of my PhD.

I thank also Dr. Stefano Rusponi and all people involved en our collaboration about the adsorption site of Co for spreading your knowledge with me and giving me the chance to be part of the paper.

Además, quiero agradecer también a Iñaki Piquero y Jorge Lobo por las discusiones sobre el estado de superficie del Au(111) y el buen trabajo realizado.

Next, I would like to thanks all people from CFM and DIPC that I met during this years for creating a really nice environment to work. I really enjoy this time with you.

También me gustaría agradecer al club Elgoibarko SANLO E.K.T. y todas las personas del club por acogerme desde el principio como a uno más y permitirme despejarme cuando más lo necesitaba practicando el deporte que más me gusta.

Azkenik, hiru pertsona oso berezi gelditzen zaizkit eskertzeko. Beraiek gabe ez nuke inoiz fisika ikasiko eta ez nintzateke hemen egongo. Mila esker Joseja Huerta, Eli Zugasti eta Juanba Artola; zuekin eman bainituen nire lehengo urratsak zientziaren munduan.

Resumen

El rápido avance tecnológico de las últimas decadas y el gran impacto que tiene la información en la sociedad actual crean la necesidad de buscar nuevas formas más eficientes de almacenar la información. La cantidad total de información almacenada en el mundo ha pasado de 1 ZB (10^{21} B) en 2009 a alrededor de 20 ZB en 2017, y se espera que siga creciendo, superando los 160 ZB en 2025. Este aumento se ha visto enormemente favorecido por la aparición de nuevas tecnologías como los coches autónomos, la inteligencia artficial y electrodomésticos inteligentes. Todos estos avances necesitan procesar una cantidad enorme de información que tiene que ser almacenada de alguna forma.

Hoy en día, la información se almacena en tres tipos de dispositivos: ópticos, eléctricos y magnéticos. Los dispositivos más comunes y de más capacidad son los dispositivos de almacenamiento magnéticos. Éstos almacenan la información en forma de dominios magnéticos localizados en un material magnético. La información de estos dominios se lee y escribe mediante una cabeza que detecta y modifica la magnetización de dicho dominio. Este tipo de tecnología se emplea en los discos duros, las bandas magneticas (tarjetas de crédito) y las memorias RAM (*random access memory*) magnéticas o MRAM. Generalmente, la capacidad de un dispositivo magnético aumenta cuanto más pequeño sean los dominios. Los dispositivos convencionales tienen la capacidad de almacenar alrededor de 1 Pbit/m^2 (10^{16} bit/m^2), lo que significa que cada dominio ocupa unos 100 nm^2 de la superficie magnética. En última instancia, el tamaño límite de estos dominios sería el límite atómico.

El objetivo de esta tésis es estudiar estos dominios magnéticos en el límite atómico. Para ello es necesario estudiar como son las interacciones magnéticas a escala atómica. En sólidos, la interacción entre átomos vecinos es tan fuerte que los cambios en un átomo se reflejan en los de su entorno. Esto hace que sea complicado alcanzar el límite atómico. Por ejemplo, el bit más pequeño que se ha conseguido crear es de unos 12 átomos.

El tamaño del dominio magnético no es el único factor a tener en cuenta a la hora de construir un dispositivo de almacenamiento magnético. Esos mo-

mentos magnéticos tienen que ser estables durante un largo periodo de tiempo para no perder la información. La barrera de anisotropia magnética (MAE) determina la estabilidad del dominio magnético frente a fluctuaciones. A escala atómica, una MAE alta requiere una combinación de un acoplamiento espín-órbita fuerte y un campo cristalino adecuado. Los átomos de transición $3d$, a pesar de tener un acoplamiento espín-órbita relativamente bajo, pueden tener valores bastante altos de la MAE en circunstancias especiales, tal y como veremos para el Co. Además de una MAE grande, es necesario que el momento magnético no se pierda debido a la interacción con electrones de conducción o fonones del substrato. Estas interacciones con el substrato se pueden evitar, o por lo menos reducir, usando laminas delgadas de carácter aislante que reducen las interacciones entre el substrato y los momentos magnéticos. Una de estas laminas aislantes es la monocapa de nitruro de boro hexagonal (h-BN), que se puede depositar sobre superficies metálicas como el Ir o el Ru.

En esta tésis desarrollamos un nuevo método teórico y lo comparamos con otros métodos y resultados experimentales. Este nuevo método deriva un campo cristalino (CF) a partir de cálculos de la teoría del funcional de la densidad (DFT), para posteriormente introducirlo en un modelo de Hubbard multiorbital. Los cálculos DFT se hacen con el código de ondas planas *Vienna Ab-initio Simulation Package* (VASP), para después, mediante un cambio de base a orbitales de Wannier maximalmente localizados (MLWF), derivar un Hamiltoniano que es el que utilizaremos como CF. El cambio de base de ondas planas a MLWF, lo hacemos con el código *Wannier90*, el cual nos permite escribir el Hamiltoniano de interacción en la nueva base. Este Hamiltoniano es todavía demasiado grande para poder introducirlo en el modelo de Hubbard. Por lo tanto, primero identificamos cuales son los orbitales localizados en el átomo magnético y detectamos que orbitales se hibridizan más con ellos. Después, aplicando el método perturbativo de Feshbach-Schur, derivamos el Hamiltoniano efectivo en el espacio reducido y lo introducimos en el modelo de Hubbard. El objetivo principal de este modelo es representar el espectro de baja energía lo mejor posible, incluyendo excitaciones de espín. Este modelo incluye la interacción de Coulomb, el campo cristalino, el acoplamiento espín-órbita y un término de Zeeman. Todos estos términos se derivan de forma analítica, a excepción del campo cristalino, que depende del entorno donde se encuentra el átomo magnético. Una vez obtenido el campo cristalino, resolvemos el modelo de Hubbard mediante el método de interacción de configuraciones (CI). Este método construye la matriz Hamiltoniana a partir de cada una de las posibles configuraciones con un número de electrones fijo, teniendo en cuenta el principio de exclusión de Pauli. Después, obtenemos el espectro de baja energía.

En este trabajo utilizamos este nuevo método para obtener el espectro de baja energía de átomos aislados de Co sobre una monocapa de h-BN. Para ello, primero tenemos que comprobar que con los cálculos DFT estamos simulando correctamente el h-BN. Estos cálculos DFT nos dan que el h-BN es un material aislante con un *gap* de energía en el punto K de 4.66 eV y un parámetro de red de 2.51 Å en línea con resultados previos de DFT. Luego, en una supercelda 4×4 de h-BN, colocamos el Co sobre los dos sitios más favorables del h-BN: sobre un átomo de N (*atop N*) y sobre el centro del hexagono formado por la red (*hollow*). Tras una relajación, vemos que ambos sitios de absorción del átomo de Co están bastante cerca en energía (389 meV a favor del sitio *hollow*), tienen una ocupación de los orbitales d de 7.8 electrones y una magnetización de alrededor de 2 μ_B, lo cual es compatible con un espín $S = 1$. Además, la densidad de estados proyectados sobre los orbitales d del átomo de Co muestra una hibridación débil entre los diferentes orbitales $3d$ del átomo de Co y estados $2p$ del h-BN. En el caso *atop N*, estas hibridaciones corresponden a estados d_{z^2} del átomo de Co con estados p_z del átomo de N que tiene debajo. Por el contrario, en el caso *hollow*, los estados d_{xz} y d_{yz} del átomo de Co hibridizan con los estados p_z de los 3 átomos de N y los 3 átomos de B que forman el hexagono en el que se encuentra. Añadiendo el acoplamiento espín-órbita a estos cálculos DFT (DFT+SOC), reducimos la diferencia energética entre ambos sitios de absorción a 316 meV. Además, obtenemos que para el sitio *atop N*, el Co tiene un eje de cuantización fácil en la dirección perpendicular al plano del h-BN, con una MAE de 1.5 meV. Mientras, para el sitio *hollow*, obtenemos que el eje perpendicular es un eje difícil con una MAE de 0.43 meV. Posteriormente, a partir de los cálculos DFT sin polarización de espín para ambos sitios de absorción, hacemos el cambio de base a MLWF en la supercelda 3×3 y comprobamos que los orbitales d del átomo de Co tienen forma de orbitales d átomicos. Seguidamente, reducimos el Hamiltoniano de Wannier y lo introducimos en el modelo multiorbital de Hubbard para obtener el espectro de baja energía. Los resultados obtenidos con el nuevo método concuerdan cualitativamente con los obtenidos mediante los cálculos DFT+SOC. En ambos casos se obtiene que el sitio *atop N* tiene un eje de magnetización fácil perpendicular al plano y que el *hollow* tiene un eje difícil. Con la nueva metodología los valores de la MAE son un orden de magnitud más grandes (mayor que 30 meV y unos 3 meV para el *atop N* y el *hollow*, respectivamente). La razón principal de este desacuerdo en la magnitud de la MAE podría radicar en que los cálculos DFT+SOC infravaloran el momento orbital, por lo que la MAE obtenida de estos cálculos es demasiado pequeña. Por esto, necesitamos comparar el nuevo método con otra aproximación diferente. En este caso, optamos por introducir el CF en nuestro modelo de Hubbard con una aproximación de

cargas puntuales. Las posiciones y las cargas las derivamos de los cálculos DFT anteriores. En este caso, el acuerdo también es cualitativamente bueno, puesto que reproducimos los ejes fáciles y difíciles para el sitio *atop N* y *hollow*, respectivamente. El valor de la MAE es de unos 13 meV para el sitio *atop N* y unos 5 meV para el *hollow*. De este último cálculo con el modelo de cargas puntuales derivamos un Hamiltoniano de espín y extraemos los parámetros de anisotropía.

En nuestro caso, como disponemos de resultados experimentales de espectroscopía de absorción de Rayos X (XAS), dicroísmo circular magnético en absorción de Rayos X (XMCD) y dicroísmo linear magnético en absorción de Rayos X (XMLD) sobre el h-BN/Ir(111) y h-BN/Ru(0001), nos centramos en las propiedades del Co en estos dos substratos. Para simular el sitio de absorción del átomo de Co en los experimentos, primero debemos ver como se comporta el h-BN en estas superficies. Los cálculos DFT muestran que, en el caso de la superficie de Ir(111), el h-BN se absorbe a unos 3.1 Å de altura sobre la superficie y que se mantiene prácticamente plano. Esto nos lleva a pensar que en Co/h-BN/Ir(111) se comporte de forma parecida al caso sin Ir(111), y por lo tanto, que el sitio de absorción sea *hollow*. El Ru(0001), al ser más reactivo que el Ir(111), interacciona más con el h-BN y le da una corrugación mucho mayor. Así, en este caso, estudiamos los dos sitios de absorción del Co a distantas alturas del h-BN con respecto de la superficie de Ru(0001). Las energías relativas obtenidas de los cálculos DFT muestran que el sitio *hollow* en la region del h-BN lejana, y el *atop N* en la región cercana, son los más favorables, pero con diferencias de energías en límite de la fiabilidad de los cálculos DFT. Por eso prefirimos combinar los datos experimentales con los resultados del modelo multiorbital de Hubbard para determinar el sitio de absorción en h-BN/Ru(0001). Con respecto a los experimentos, los datos de XAS en ambas superficies son compatibles con una ocupación de 8 electrones en la capa d del átomo de Co, compatible con el espín $S = 1$ que hemos obtenido de los cálculos DFT anteriores. Además, los experimentos de XMCD y XMLD mustran una anisotropía magnética de unos 13.7 meV para el Co/h-BN/Ru(0001) y una anisotropía despreciable para el Co/h-BN/Ir(111). Posteriormente, usando unos ajustes de multipletes simulando que el átomo de Co está en posición *atop N*, vemos que el estado fundamental del Co/h-BN/Ru(0001) es un doblete con $S_z = \pm 1$ y $L_z = \pm 1.42$, y el excitado un singlete con $S_z = 0$ y $L_z = -0.02$. Estos resultados concuerdan plenamente con los resultados que hemos obtenido con nuestro modelo de Hubbard usando las cargas puntuales para el sitio *atop N* en h-BN. Nuestro modelo muestra un doblete fundamental con $S_z = \pm 0.96$ y $L_z = \pm 1.04$, y un singlete excitado con $S_z = -0.09$ y $L_z = 0.09$, además de una MAE de unos 13 meV. Los ajustes de multipletes para el Co/h-

BN/Ir(111) muestran un singlete fundamental con $S_z = 0.003$ y $L_z = 0.022$, y un doblete excitado con $S_z = \pm 0.92$ y $L_z = \pm 1.13$, solamente 0.7 μeV por encima. En este caso, el acuerdo con nuestro modelo para el sitio *hollow* no es tan bueno, puesto que las cargas puntuales nos llevan a un singlete fundamental con $S_z = 0.19$ y $L_z = 0.61$, y un doblete excitado con $S_z = 0.76$ y $L_z = 1.44$, unos 5 meV por encima. En el caso del *atop N* con el Co/h-BN/Ru(0001), el buen acuerdo se debe a que el campo cristalino en el sitio *atop N* es creado principalmente por el átomo de N de debajo, y apenas se ve afectado por pequeñas variaciones del entorno. Sin embargo, en el caso *hollow*, el CF es bastante más débil debido a que las cargas de los átomos vecinos tienden a crear un CF nulo sobre el Co. Además, es posible que el momento magnético del Co se anule debido a la interacción con el substrato metálico. Esto hace que el sitio *hollow* sea mucho más sensible a las variaciones del entorno, asi como a la corrugación.

Por lo tanto, también es importante estudiar como son este tipo de interacciones a la hora de diseñar un nuevo dispositivo de almacenamiento magnético. A menudo, las interacciones con el substrato metálico suelen involucrar a electrones de superficie. Estos estados de superficie son producto de soluciones a la ecuación de Schorödinger de una partícula con vector de onda imaginaria en regiones donde se ha abierto un gap de energía. La energía con la que aparecen estos electrones superficiales se puede controlar mediante la absorción de diferentes nanoestructuras, propiciando la transferencia de carga o el confinamiento de los electrones a una región determinada de la superficie. Respecto a la transferencia de carga, dependiendo de que nanoestructura se absorba sobre la superficie, ésta puede coger electrones, bajando la energía de los electrones superficiales, o donar electrones, aumentando la energía. En el caso del confinamiento, al reducir la región en la que aparecen los electrones superficiales, en todos los casos aumentará la energia en la que aparecen.

Además de estudiar las propiedades del Co sobre el h-BN, en la tesis también analizamos un caso reciente donde, sin haber transferencia de carga, la energía de los electrones superficiales baja, a pesar del confinamiento demostrado experimentalmente. Esta bajada de energía se ha medido en redes organometálicas nanoporosas (MONN) como el Ph6Co o el Ph3Co sobre la superficie de Au(111). Estas MONN están formadas por las moléculas dicarbonitrilo-terfenilo (Ph3) o dicarbonitrilo-sexifenilo (Ph6) y átomos de Co como enlaces de las moléculas formando una estructura con nanoporos hexagonales. Los poros del Ph6Co son más grandes que los del Ph3Co, al ser el Ph6 una molécula más grande que el Ph3. Sin embargo, el estado de superficie del Au(111) baja más, respecto a la cara original, con el Ph3Co que con el Ph6Co. Para simular este sistema, usamos una lámina de 4 capas de

Au(111) y pasivamos una de las caras con átomos de H. Comprobamos que este modelo funciona, poniendo sobre la otra cara una monocapa molécular de pirazina. La monocapa molécular actua como un aislante, confinando el estado de superficie y aumentando su energía en comparación con la cara sin la monocapa. Posteriormente, colocamos sobre superficie de Au(111) un átomo de Co en superceldas 2×2, 3×2 y 3×3 a una distancia de 2.5 Å. Esta distancia es superior a la distancia de absorción óptima para simular que está en el régimen de acoplamiento débil. De los cálculos DFT sin polarización de espín vemos que, en el caso de la supercelda 2×2, la bajada es mayor que en la 3×2. En ésta, a su vez, es mayor que en la 3×3. Con estos resultados confirmamos la bajada del estado de superficie y vemos que ésta bajada es mayor cuanto mayor es la concentración de átomos de Co. En los MONN de los experimentos, vemos que ésta relación también es válida, ya que en el caso del Ph3Co, al tener los poros mas pequeños, la concentración de átomos de Co es mayor, y la bajada del estado de superficie también es mayor. Además, la extrapolación lineal de los resultados DFT, dan un acuerdo muy bueno con las mediciones experimentales. Confirmamos que con cálculos polarizados en espín obtenemos los mismos resultados, y seguidamente, sustituimos el átomo de Co por el de Au y aumentamos la distancia a 3 Å para colocarlo en el régimen de acoplamiento débil. En este caso volvemos a obtener una bajada del estado de superficie mayor en la supercelda 2×2, que en la 3×3. Luego, hacemos lo mismo para un átomo de Cu a 3 Å de una lámina de 4 capas de Cu(111), pasivada con átomos de H por el lado contrario, con los mismos resultados. Finalmente, acercamos al átomo de Cu a la superficie de Cu(111), hasta 2.5 Å, y vemos que el peso del estado de superficie se divide en dos bandas: una componente se mezcla con las bandas d de valencia de la lámina de Cu(111) y el otro por encima del nivel de Fermi. Por lo tanto, podemos decir que este efecto de la bajada del estado de superficie es un efecto que se da cuando se absorben ciertos metales de transición en el regimen de acoplamiento débil sobre algunas superficies metálicas, debido a que el estado enlazante todavía mantiene el carácter del estado de superficie. Sin embargo, al aumentar el acoplamiento, el estado enlazante va perdiendo el carácter de estado de superficie, mientras el estado antienlazante lo va ganando, subiendo en energía.

Contents

List of Figures

Chapter 1

INTRODUCTION

The Data Age is approaching. The fast-paced technological evolution during the last decades challenges us to think about the impact of data management and the need of new technological routes to store data. The amount of stored data has grown exponentially in recent years, from 1 ZB (10^{21} B) in 2009 to around 20 ZB in 2017, and it is predicted to continue growing, reaching 160 ZB in 2025[1]. This is favoured by the appearance of new technological applications such as autonomous cars, artificial intelligence and smart home devices, which are likely going to transform the way we live. These advances are based on processing huge amounts of data that need to be stored somehow.

Nowadays, there are three types of devices to store all this data: optical, electrical and magnetic storage devices. Optical devices, such as CDs or DVDs, have a reflective surface which is divided into small sections that can contain a hole or not. Each of the sections is a bit which is readable with a laser beam. This devices are still alive due to music, video and videogames industries. Electric storage devices use small floating-gate-transistors, like USB memories or SD cards. These transistors can store an electric charge for an extended period of time without a power supply. They have a limited number of write/erase cycles, but they are small and cheap, thus representing perfect portable devices.

Magnetic storage devices store data as a localized magnetic domain in a magnetic medium. This type of storage is the oldest and has the greatest capacity. Information is written and read from the medium by a read-and-write-head, which detects and modifies the magnetisation of a specific magnetic domain below it. There are two magnetization polarities for the domains, which represent either 0 or 1 in a binary system. Magnetic storage is used in hard disks, Magnetic Random Access Memories (MRAM) and magnetic stripes to store data.

Focusing on hard disks, the ferromagnetic material is a thin film, 10-20 nm in depth, deposited on a non-magnetic circular substrate, usually aluminium alloy, glass or ceramic, and protected with an outer layer of carbon. This disk is called platter and modern hard disks have several platters. Each magnetic platter has one head mounted in an actuator arm, who moves the heads on an arc over some the platters as they spin. Modern commercial devices made in this way have reached areal data densities above 10 Pbit/m^2 (10^{16} bit/m^2)[2], which means that the size of each bit is around 100 nm^2.

As mentioned at the beginning, we need devices with larger storage capacities to store the increasing amount of data being created in the upcoming years. This goal can be achieved, in the case of hard disks, by increasing the areal data density of platters, i.e., reducing the size of each bit.

In theory, the ultimate size of a magnetic domain is the atom. In solids, the interaction between neighbour atom is so strong that changes in one atoms are reflected in neighbouring atoms. Thus, each magnetic moment needs to be far enough from the neighbouring magnetic moments to permit a local manipulation without affecting its neighbourhood. This condition make difficult to achieve the ultimate size limit. In laboratory conditions, magnetic bits as small as 12 atoms have been built[3, 4, 5, 6].

However, the size is not the only important feature for a magnetic domain. The stability of those magnetic moments depend on additional factors. The Magnetic Anisotropy Energy (MAE) determines the stability of a magnetic moment against fluctuations. At the microscopic scale, a large spin-orbit coupling and a suitable crystal field may yield to a large MAE[7, 8]. Although spin-orbit coupling in late $3d$-transition metal atoms is relatively weak, they can show very large MAE values when they are adsorbed under special circumstances, as it is the case of Co single atoms and nanostructures on Pt single crystals[9, 10].

But a large MAE does not guarantee stability. The spin lifetime of Co atoms on Pt(111) is sub-nanosecond and do not show hysteresis, even at sub-Kelvin temperatures[11]. These observations highlight that spin scattering with conduction electrons and substrate phonons is detrimental to the stability of the magnetic moment of isolated impurities. Furthermore, atomic-scale magnetic moments can be quenched when interacting with itinerant electrons, as Shockley surface electrons, on a nearby metal, leading to the formation of Kondo singlets[12].

Thus, in order to obtain stable nanomagnets, large MAE and weak electronic and phonon interactions with the surroundings are essential [6, 7, 8]. Thin decoupling layers can be introduced to reduce the hybridization of the $3d$ or $4f$ adsorbates with the metallic substrate, thus protecting the magnetic moments from destabilizing scattering processes, while still allowing for large

values of the MAE. Examples of metallic substrates with decoupling layers are: MgO on Ag(001)[7, 13, 14], graphene on Pt(111)[15], graphene on Ir(111) and Ru(0001)[16, 17] or h-BN on Rh(111)[18, 19]. For instance, in the case of h-BN/Rh(111)[19], hydrogenated cobalt complexes are adsorbed atop N sites of the h-BN lattice, showing relatively large out-of-plane MAE.

From the experimental point of view, there are three frequently used experiments that can measure the MAE of magnetic impurities adsorbed on surfaces: X-ray Magnetic Circular Dichroism (XMCD), Inelastic Electron Tunnelling Spectroscopy (IETS) and Scanning Tunneling Microscopy induced Electron Spin Resonance (STM-ESR). In order to interpret XMCD data, electronic multiplet calculations and sum rules analysis are needed[20, 21], with some fitting parameters needed to determine the crystal field and spin-orbit coupling strength. The other experiments, IETS[22] and STM-ESR[23], yields the spin excitation energies of a single or a few magnetic coupled atoms. The magnetic anisotropy is then described in terms of some characteristic parameters by using a phenomenological spin Hamiltonian [7, 13, 19, 24, 25]. STM-ESR adds the extreme energy resolution of magnetic resonance, which is only limited by the decoherence rate $1/T_2$, while still conserving the atomic resolution of STM. Unfortunately, this technique has only been applied successfully to MgO/Ag(001) substrate[7, 23].

From the theoretical point of view, Density Functional Theory (DFT) calculations including Spin-Orbit Coupling (DFT+SOC) allow an estimation of the MAE, but, in general, MAE is strongly underestimated. This stands on the overestimation of the quenching of the orbital momentum[26, 27, 28]. Recently, a new approach[29, 30] to calculate the MAE has been developed. This new approach consist on using DFT calculations to estimate the crystal field, and then, to construct a many-body multiorbital Hamiltonian including the obtained crystal field, spin-orbit and electron correlation effects. At the atomic-scale, magnetic moments of adsorbed atoms can be quenched due to spin scattering events with conduction electrons from the surface. Thus, surface states also play an important role in the stability of the magnetic moment, especially if they hybridize with states from the magnetic adatom. So it is important to understand how the hybridization occurs and how to control it.

As their name indicates, surface states are 2D states located at the surface of a solid, generated by the symmetry breaking of the crystal in the surface. It is possible to split surface states into two groups: Shockley surface states[31] and Tamm surface states[32]. Shockley surface states emerges from the description of *sp*-bands, while Tamm surface states form from d and f-bands. So the possible hybridizations are different for each group.

Surface states have influence on the electronic and magnetic properties of

the surface and the superstructures grown on them by different mechanism. One of this mechanism is the charge transfer between the surface state and the adsorbate, which can happen in both directions. In the case of Na or Cs on Cu(111)[33, 34, 35], the surface state is shifted down in energy due to the electron that it takes from the adsorbate. On the contrary, an electron may also go from the surface to the adsorbate, like in TTF-TCNQ overlayer on Au (111)[36], where the surface state is shifted up.

Confinement is another mechanism that allows the control of the surface state. This is made usually by growing on the desired surface a vast range of nanoporous networks, from hydrogen or halogen bonded molecular networks[37, 38] to metal-organic superstructures[39, 40], as organic molecules scattered on a surface where electrons are confined into the pores of the network. This mechanism push the surface state upward in energy, likewise a quantum box.

In order to study the surface state experimentally, a combination of Angle Resolved Photo-Emission Spectroscopy (ARPES) technique with Electron Plane Wave Expansion (EPWE) simulations[41] is used, as well as the Fourier-Transform Scanning Tunnelling Spectroscopy (FT-STS)[42]. From the theoretical point of view, performing DFT calculations to obtain the bandstructures of the system is a good choice to model the surface state using the passivated slab proposed by Gonzalez-Lacunza[43].

This thesis is organized in the following way. A brief introduction to the theory of solids is given in chapter 2. In particular, DFT calculations and MLWFs are introduced, focusing on solving the Schrödinger equation for a solid in the plane-wave basis set, as it is implemented in the *Vienna Ab-initio Simulation Package* (VASP) code[44, 45, 46] and changing the basis to the MLWFs basis set using the *Wannier90* code[47]. Following the approach developed in the group of Fernandez-Rossier[29, 30], this basis change will provide the crystal field that we will use to construct a many-body multiorbital Hamiltonian.

The main results of the thesis will be splitted into chapter 3 and 4. Chapter 3 describes Co adatom on different adsorption sites of h-BN using different theoretical methods. The first method will be using only DFT calculation including spin-orbit coupling. In second place, we will construct a many-body multiorbital Hamiltonian based on two different approaches to the crystal and ligand fields: an effective tight-binding Hamiltonian in the basis of MLWFs and a point charge model. Finally, we will derive a spin Hamiltonian and compare the results obtained with all the approaches.

In chapter 4, we will compare results from the previous chapter with XAS, XMCD and XMLD experimental data for Co on h-BN/Ir(111) and h-BN/Ru(0001) provided by S. Rusponi from the group of H. Brune. XMCD

and XMLD experiments show a big difference in the magnetic properties of Co atom depending on the metallic substrate, even though the occupation of *d*-shell of Co remains the same. We will use our DFT calculations to shed light on the role of the metallic substrate. In the case of the Ir(111) substrate, we will see that the h-BN is almost flat, while on the Ru(0001) substrate it is highly corrugated. This different corrugations, the adsorption site of Co may be affected on h-BN/Ru(0001), changing the adsorption site.

On chapter 5, we will focus on the Shockley surface state of Au(111) and Cu(111) and how it is affected by the adsorption of different type of adsorbates, from adatoms to molecular overlayers. We will compare our findings with ARPES data provided by I. Piquero-Zulaica from the group of J. Lobo. The experiment shows a counter-intuitive downward shift of the surface state of Au(111) and Cu(111) surfaces when Co-dicarbonitrile-terphenyl (Ph3Co) and Co-dicarbonitrile-sexyphenyl (Ph6Co) networks are grown on the surface, while the downward shift is bigger for Ph3Co network. Our model, consisting on a hydrogen passivated slab[43], permits the understanding of this effect and we will discuss the conditions to see it in other systems.

Then, chapter 6 will summarize the main conclusions of the investigations combining results from different chapters.

Finally, we have two appendixes. In appendix A, we explore the limitations of the MLWFs method in the 4×4 supercell of h-BN. Finally, in appendix B, we study the case of Fe on h-BN.

Chapter 2

THEORETICAL METHODS

This chapter introduces the theoretical framework. Throughout the thesis we will use atomic units ($m_e = e = \hbar = 1$) unless otherwise stated.

2.1 Basic quantum mechanics for solids

Formally speaking, solid materials are composed of N_i ions and n_e electrons. This means that we have to consider our system as a many-body system with $N_i + n_e$ particles. The properties of such a system can be described by the time-dependent Schrödinger equation,

$$i\frac{\partial\Psi\left(\{\mathcal{R}\},t\right)}{\partial t} = \hat{H}\Psi\left(\{\mathcal{R}\},t\right), \tag{2.1}$$

where $\Psi(\{\mathcal{R}\},t)$ is the many-body time-dependent wavefunction, with $\{\mathcal{R}\}$ representing spacial coordinates of all particles in the system. So, if $\Psi(\{\mathcal{R}\},t)$ is known for a system, static and dynamic properties of all important physical observables are available. $\hat{H}$ is the Hamiltonian operator, which consist of the kinetic and potential energy terms, describing interactions between all particles in the system. In the absence of an external field, the Hamiltonian is given:

$$\hat{H} = \hat{T}_i + \hat{T}_e + \hat{V}_{ii} + \hat{V}_{ee} + \hat{V}_{ie}. \tag{2.2}$$

$\hat{T}_i$ and $\hat{T}_e$ terms correspond to kinetic energy of ions and electrons, respectively, and can be expressed as the sum of kinetic energy of each ion or electron

$$\hat{T}_i = -\sum_{\alpha}^{N_i}\frac{\mathbf{P}_\alpha^2}{2M_\alpha} \tag{2.3}$$

and

$$\hat{T}_e = -\sum_{\nu}^{n_e} \frac{\mathbf{p}_\nu^2}{2}, \tag{2.4}$$

where the indices α and ν run over ions and electrons, respectively.

The other three terms correspond to the Coulomb repulsion between ions, $\hat{V}_{ii}$, and electrons, $\hat{V}_{ee}$ and Coulomb attraction of ions and electrons, V_{ie}:

$$\hat{V}_{ii} = \frac{1}{2}\sum_{\alpha\neq\alpha'}^{N_i} \frac{Z_\alpha Z_{\alpha'}}{|\mathbf{R}_\alpha - \mathbf{R}_{\alpha'}|}, \tag{2.5}$$

$$\hat{V}_{ee} = \frac{1}{2}\sum_{\nu\neq\nu'}^{n_e} \frac{1}{|\mathbf{r}_\nu - \mathbf{r}_{\nu'}|} \tag{2.6}$$

and

$$\hat{V}_{ie} = -\sum_{\alpha,\nu}^{N_i,n_e} \frac{Z_\alpha}{|\mathbf{R}_\alpha - \mathbf{r}_\nu|} \tag{2.7}$$

where M_α and Z_α are respectively the mass and atomic number of each ion. $\mathbf{R}_\alpha$ and $\mathbf{P}_\alpha$ denote the sets of position and momentum of ions and $\mathbf{r}_\nu$ and $\mathbf{p}_\nu$ for electrons.

2.1.1 The Born-Oppenheimer approximation

Born and Oppenheimer proposed a scheme for separating the motion of nuclei from that of electrons[48]. This is based on the fact that the time scale associated to the motion of nuclei is usually much longer than that associated to electrons. The origin of this is the difference in mass between nuclear particles and electrons. In the case of Hydrogen atom, the most unfavourable case, the mass ratio is 1:1836, which is less than 0.1%. So, from a classical point of view, the speed of the electron is much higher than that of the nuclei. Born and Oppenheimer introduced the mass ratio perturbatively in the time-dependent Hamiltonian and they showed that different electronic stationary states do not mix due to the interaction with the nuclei. Therefore, the electrons do not undergo transitions between stationary states.

In principle, this approach is also valid for molecules, insulating and semiconducting systems. There the smallest electronic excitation is given by the energy gap, which is typically a few eV, while for the nuclear motion, excitations are at least two orders of magnitude smaller. For metallic systems, the relevant energy scale is dictated by plasmon (collective charge oscillations), which is typically of the order of few eV. So electrons can be thought

of as instantaneously following the motion of nuclei, while remaining always in the same stationary state of the electronic Hamiltonian. In other words, electrons adjust their wavefunction instantaneously according to the nuclear motion

$$\Psi\left(\{\mathcal{R}\},t\right)=\sum_{n}\chi_{n}\left(\mathbf{R},t\right)\psi_{n}\left(\mathbf{R},\mathbf{r}\right), \tag{2.8}$$

where $\chi_n(\mathbf{R},t)$ are the wavefunctions that describe the evolution of nuclei in each one of the electronic eigenstates $\psi_n(\mathbf{R},\mathbf{r})$. These electronic states satisfy the time-independent electronic Schrödinger equation

$$\hat{h}_{e}\psi_{n}\left(\mathbf{R},\mathbf{r}\right)=E_{n}\left(\mathbf{R}\right)\psi_{n}\left(\mathbf{R},\mathbf{r}\right), \tag{2.9}$$

where $\hat{h}_e$ is the electronic Hamiltonian:

$$\hat{h}_{e}=\hat{T}_{e}+\hat{V}_{ee}+\hat{V}_{ie}=\hat{H}-\hat{T}_{i}-\hat{V}_{ii}. \tag{2.10}$$

In eq. (2.9) nuclear coordinates $\mathbf{R}$ enter as parameters. As $\psi_n(\mathbf{R},\mathbf{r})$ are solutions of the time-independent electronic Schrödinger equation corresponding to a particular nuclear configuration, the expansion described in eq. (2.8) is always mathematically possible. Therefore, we need to know the nuclear and electronic wavefunctions. So, we will start obtaining the nuclear wavefunction.

The total nuclear wavefunction can be considered as an incoherent superposition of individual nuclear wave packets;

$$\chi_{n}\left(\mathbf{R},t\right)=\prod_{\alpha=1}^{P}\chi_{n}^{(\alpha)}\left(\mathbf{R},\mathbf{R}^{(\alpha)}\left(t\right),t\right), \tag{2.11}$$

where $\mathbf{R}^{(\alpha)}(t)$ are the centres of each individual wave packets. As nuclear masses are quite large, these individual wave packets are strongly localized around their centres. Therefore, atomic nuclei are treated as classical particles. It is worthy mentioning that eq. (2.11) does not include correlations between different nuclei. So, the time-dependent Schrödinger equation for nuclear wavefunction is

$$i\frac{\partial\chi_{m}\left(\mathbf{R},t\right)}{\partial t}=\left[-\sum_{\alpha=1}^{P}\frac{1}{2M_{\alpha}}\nabla^{2}+\tilde{\epsilon}_{n}\left(\mathbf{R}\right)\right]\chi_{m}\left(\mathbf{R},t\right), \tag{2.12}$$

with

$$\tilde{\epsilon}_{n}\left(\mathbf{R}\right)=\epsilon_{n}\left(\mathbf{R}\right)+\sum_{\alpha=1}^{P}\frac{1}{2M_{\alpha}}\langle\psi_{q}|\nabla_{\alpha}^{2}|\psi_{q}\rangle. \tag{2.13}$$

The second term is the correction due to the dependence of electronic wavefunction on nuclear coordinates, which is proportional to the electron mass. This correction, in the most unfavourable case, is smaller than 0.5%. Therefore, it is usually neglected in the Born-Oppenheimer approximation.

Introducing eq. (2.11) into eq. (2.12) and taking the mean values, one can find the following Newtonian equation of motion:

$$M\frac{d^2\langle\mathbf{R}\rangle}{dt^2} = -\langle\nabla\epsilon_n\left(\mathbf{R}\right)\rangle, \tag{2.14}$$

where $\epsilon_n(\mathbf{R})$ is the potential. In the classical nuclei approximation, the mean value of the position operator $\langle\mathbf{R}\rangle$ is identified with the coordinates of the classical particle. This equation is solved by numerical integration methods in *ab-initio molecular dynamics*. Imposing $\nabla\epsilon_n\left(\mathbf{R}\right) = 0$, we can get the solution corresponding to a *geometrical optimization*.

2.1.2 Density Functional Theory

The Born-Oppenheimer approximation reduces the dimensionality of the problem solving the nuclear part of the eigenstate, but the electronic part still remains unsolved. Due to electron-electron interaction term in the electronic Hamiltonian, there is no general solution for eq. (2.9). One method to overcome this problem is to use Density Functional Theory (DFT). DFT consist in using the electron density as key quantity in the many-body problem instead of electronic wavefunctions, which reduces the degrees of freedom from $3n_e$ to only 3.

The electron density is defined as follows:

$$n\left(\mathbf{r}\right) = \int d\mathbf{r}_2 \ldots d\mathbf{r}_{n_e} |\psi\left(\mathbf{r}, \mathbf{r}_2, \ldots, \mathbf{r}_{n_e}\right)|^2, \tag{2.15}$$

where the parametric dependence of the electron density on the ionic positions is assumed, i.e. $n(\mathbf{r}) \equiv n(\mathbf{r}, \mathbf{R})$. This relation can be reversed, except of a phase of the wavefunction, so from the ground-state density, $n_0\left(\mathbf{r}\right)$, it is possible to get the ground-state electronic wavefunction, $\psi_0\left(\mathbf{R}, \mathbf{r}\right)$.

The electronic Hamiltonian is expressed in terms of the electronic density $n\left(\mathbf{r}\right)$, so that each contribution becomes a functional of $n\left(\mathbf{r}\right)$. We can approximate the electronic $\psi_n\left(\mathbf{r}\right)$ by the Slater determinant of single-particle wavefunctions $\phi_\nu\left(\mathbf{r}_\nu\right)$:

$$\psi\left(\mathbf{r}_1, \mathbf{r}_2, \ldots, \mathbf{r}_{n_e}\right) = \frac{1}{\sqrt{n_e!}} \begin{vmatrix} \phi_1\left(\mathbf{r}_1\right) & \cdots & \phi_1\left(\mathbf{r}_{n_e}\right) \\ \vdots & \ddots & \vdots \\ \phi_{n_e}\left(\mathbf{r}_1\right) & \cdots & \phi_{n_e}\left(\mathbf{r}_{n_e}\right) \end{vmatrix}. \tag{2.16}$$

This wavefunction $\psi(\mathbf{r}_1, \mathbf{r}_2, \ldots, \mathbf{r}_{n_e})$ shows the fundamental properties of a fermionic system. Therefore, the exchange of two rows or columns is equivalent to the interchange of two particles, which makes the wavefunction antisymmetric to the exchange of particles. Consequently, if two rows or columns are equal, there are two electrons in the same state, and the wavefunction is zero. Thus ensures these wavefunctions satisfy the Pauli exclusion principle.

Adapting the definition of the electronic density given in eq. (2.15) to the single-electron wavefunctions $\phi_\nu(\mathbf{r}_\nu)$ used in eq. (2.16), we get the expression

$$n(\mathbf{r}) = \sum_{\nu}^{n_e} |\phi_\nu(\mathbf{r})|^2 . \tag{2.17}$$

This definition of the electronic density permits us to write the Hamiltonian as a functional of the electronic density. Firstly, the electron-ion interaction energy is

$$E_{ei}[n] = \langle \phi | V_{ei} | \phi \rangle = -\sum_{\alpha}^{N_i} Z_\alpha \int d\mathbf{r} \frac{n(\mathbf{r})}{|\mathbf{r} - \mathbf{R}_\alpha|} \equiv \int d\mathbf{r} n(\mathbf{r}) v_{ext}(\mathbf{r}) , \tag{2.18}$$

where $v_{ext}(\mathbf{r})$ is the external potential created by the ions. Secondly, the electron-electron interaction energy is

$$E_{ee}[n] = \langle \phi | V_{ee} | \phi \rangle = \frac{1}{2} \iint d\mathbf{r} d\mathbf{r'} \frac{n(\mathbf{r}) n(\mathbf{r'})}{|\mathbf{r} - \mathbf{r'}|} + E_{xc}[n] \equiv E_h[n] + E_{xc}[n] , \tag{2.19}$$

where $E_h[n]$ is the Hartree energy. The $E_{xc}[n]$ term is the exchange and correlation energy that takes into account the missing electron-electron interaction contributions in the Hartree term. The exact form of the exchange and correlation term is unknown, but we consider it as a functional of the electron density. Finally, the kinetic energy term can be written in terms of single-electron wavefunctions,

$$E_{kin}[n] = \langle \phi | T_e | \phi \rangle = -\frac{1}{2} \sum_{\nu}^{n_e} \int d\mathbf{r} \phi_\nu^*(\mathbf{r}) \nabla^2 \phi_\nu(\mathbf{r}) . \tag{2.20}$$

We maintain the dependence of the kinetic energy term on the electron density using the single-electron wavefunctions notation. Therefore, the total electron energy can be written as functional of the electron density as follows:

$$E_e[n] = E_{kin}[n] + E_h[n] + E_{xc}[n] + E_{ei}[n] . \tag{2.21}$$

The first three term form which is called the universal functional, because they depend on the specific electron-ion system implicitly through the electron density. So, the only term that depends on electron-ion system explicitly is $E_{ei}[n]$, where the external potential $v_{ext}(\mathbf{r})$ created by the nuclei appears.

Regarding the external potential mentioned before, Hohenberg and Kohn proved two basic theorems[49]:

Theorem 2.1.1 *The external potential $v_{ext}(\boldsymbol{r})$ is a conversely unique functional of the electron density $n(\boldsymbol{r})$, apart from a trivial additive constant.*

Theorem 2.1.2 *The exact electron density $n(\boldsymbol{r})$ minimizes the electron energy functional $E_e[n]$.*

The theorems show that the ground state of the system can be uniquely determined by the minimization of the electron energy functional $E_e[n]$ with respect to the electron density $n(\mathbf{r})$ by a variational method. However, it is not possible to minimize this energy functional due to the unknown exact dependence of the universal functional on $n(\mathbf{r})$.

Kohn and Sham [50] proposed to construct the exact electron density $n(\mathbf{r})$ using a set of non-interacting electrons moving in the effective field created by the electron-ion system in order to minimize $E_e[n]$. Doing that, we can write the electron density in the following form:

$$n(\mathbf{r}) = \int d\mathbf{r}_2 \ldots d\mathbf{r}_{n_e} \left|\psi(\mathbf{r}, \mathbf{r}_2, \ldots, \mathbf{r}_{n_e})\right|^2 = \sum_{\nu}^{n_e} \left|\phi_\nu^{KS}(\mathbf{r})\right|^2, \tag{2.22}$$

where $\phi_\nu^{KS}(\mathbf{r})$ are the Kohn-Sham non-interacting orbitals. These single-electron wavefunctions can replace the actual wavefunction in a large amount of cases.

The Schrödinger like equations for non-interacting electrons in an effective potential $v_{eff}(\mathbf{r})$ can be written as follows

$$\left[-\frac{1}{2}\nabla^2 + v_{eff}(\mathbf{r})\right] \phi_\nu^{KS}(\mathbf{r}) = \epsilon_\nu \phi_\nu^{KS}(\mathbf{r}), \tag{2.23}$$

where the effective potential $v_{eff}(\mathbf{r})$ has the following terms:

$$v_{eff}(\mathbf{r}) = v_{ext}(\mathbf{r}) + \int d\mathbf{r'} \frac{n(\mathbf{r'})}{|\mathbf{r} - \mathbf{r'}|} + \frac{\partial E_{xc}[n]}{\partial n(\mathbf{r})}. \tag{2.24}$$

The first term $v_{ext}(\mathbf{r})$ is the external potential created by ions, the second term corresponds to the Hartree potential $v_h(\mathbf{r})$ and the last term is the exchange and correlation potential $v_{xc}(\mathbf{r})$.

The eigenvalue problems defined by the Kohn-Sham equations, eq. (2.23) are solved self-consistently. Firstly, an electron density $n(\mathbf{r})$ is proposed and introduced into eq. (2.24) to get an effective potential $v_{eff}(\mathbf{r})$. Then, this

potential is introduced in eq. (2.23) and the eigenvalue problem is solved, obtaining the corresponding Kohn-Sham non-interacting orbitals $\phi_\nu^{KS}(\mathbf{r})$. Finally, with $\phi_\nu^{KS}(\mathbf{r})$, a new electron density $n'(\mathbf{r})$ is calculated from eq. (2.22) and compared with the electron density $n(\mathbf{r})$ proposed at the beginning. This process is repeated until the desired convergence threshold is achieved.

2.1.3 Approximations of the exchange and correlation functional

The exact exchange and correlation functional is known for the case of the uniform electron gas (UEG), in which the approximations are based. The simplest approximation, which was also proposed by Kohn and Sham[49], is the Local Density Approximation(LDA), where it is assumed that exchange and correlation energies are local functions of the electron density in the limit of UEG. We also assume that the electrons are independent, as in the UEG, and move in an external potential created by a positive charge background, as it happens for electrons in the Kohn-Sham equations, eq. (2.23). So the first step to find an expression for $E_{xc}[n]$ will be to suppose the same functional dependence for the system as for the UEG:

$$E_{xc}^{LDA} = \int d\mathbf{r} n(\mathbf{r}) v_{xc}^{UEG}[n(\mathbf{r})]. \tag{2.25}$$

It is assumed that the exchange and correlation potential in each point of the space $\mathbf{r}$ have the same form as in the UEG, so we can decompose $v_{xc}^{UEG}(\mathbf{r})$ linearly into exchange and correlation terms:

$$v_{xc}^{UEG}(\mathbf{r}) = v_x^{UEG}(\mathbf{r}) + v_c^{UEG}(\mathbf{r}). \tag{2.26}$$

The correlation term, $v_c^{UEG}(\mathbf{r})$, has been parametrized with quantum Monte-Carlo simulations for different electron densities [51]. The most often used parametrization is that of Perdew and Zunger[52].

The LDA approximation is very useful to get geometries and other physical properties of simple molecules and solids, particularly when s and p bands dominate the electronic structure of the valence band. On the other side, the LDA can fail when there are localized electrons dominating the electronic structure, such as in transition metals, highly inhomogeneous or strongly correlated systems.

The next approximation is called the Generalized Gradient Approximation (GGA), which introduces first-order density gradient contributions in the $E_{xc}[n]$ functional,

$$E_{xc}^{GGA} = \int d\mathbf{r} n(\mathbf{r}) v_{xc}[n(\mathbf{r}), \nabla n(\mathbf{r})]. \tag{2.27}$$

In this case, $v_{xc}\left[n\left(\mathbf{r}\right),\nabla n\left(\mathbf{r}\right)\right]$ must be parametrized. In this way, the description of some molecules and their adsorption on surfaces is improved. Different parametrizations of GGA need to be considered and compared for a system. One of the most popular GGA parametrization is the one introduced by Perdew, Burke and Ernzerhof (PBE)[53]. This type of parametrizations correct the LDA exchange term by a multiplicative factor $F_x\left(s\right)$ that depends on density gradients(s is the generalized gradient defined as $s=\left|\nabla n\right|/2k_F n$, where k_F is the Fermi wave-vector), while the correlation part is corrected by a density-dependent additive term. $F_x\left(s\right)$ is chosen to preserve the good LDA description of the exchange and correlation energy in the small s region and to satisfy the Lieb-Oxford[54] bound in the large s region. The PBE approximation has been reviewed improving atomization and chemisorption energies of some small molecules[55].

GGA-PBE approximations are enough for most of the electronic structure properties of adsorbed atoms and small molecules on metal surfaces. However, they can fail when non-local interactions, as Van deer Waals interactions, need to be included[56]. Specifically, the correlation term has to be corrected including non-local contributions

$$E_{xc}\left[n\right]=E_x^{GGA}\left[n\right]+E_c^{LDA}\left[n\right]+E_c^{nl}\left[n\right], \tag{2.28}$$

where the non-local energy $E_c^{nl}\left[n\right]$ can be expressed in the exact form[56]:

$$E_c^{nl}=\int_0^\infty\frac{du}{2\pi}Tr\left[ln\left(1-V_\chi\right)-ln\left(\epsilon\left(u,\mathbf{r},\mathbf{r}'\right)\right)\right]. \tag{2.29}$$

Here u is the imaginary frequency $-i\omega$, $\epsilon\left(\mathbf{r},\mathbf{r}',u\right)$ is the dielectric function and V_χ corresponds to the next expression:

$$V_\chi=\int d\mathbf{r}''V\left(\mathbf{r}-\mathbf{r}''\right)\chi\left(\mathbf{r}'',\mathbf{r}',u\right). \tag{2.30}$$

$\chi\left(\mathbf{r}'',\mathbf{r}',u\right)$ is the charge response function and $V\left(\mathbf{r}-\mathbf{r}''\right)$ the Coulomb potential. The trace in eq. (2.29) integrates over diagonal elements. For UEG, if we write functions that appear in eq. (2.29) in spatial coordinates, they are diagonal, and thus, $\epsilon=1-V_\chi$, and non-local corrections vanish. In this way, we ensure that there is no double counting and that we have only the LDA correlation for truly homogeneous systems.

There are other approximations to the exchange and correlation functional[57, 58, 59], but these are the most used ones, and the ones that we will use in this work.

2.1.4 Electrons in a periodic potential and pseudopotential approximation

With the Hamiltonian defined, the time-independent electronic Schrödinger equation, has to be solved to obtain $\epsilon_n(\mathbf{R})$ and its gradient. This is called an *electronic structure calculation* of a system. Its exact solution gives access to all physical and chemical properties of the system. Even though an external field may be added to the Hamiltonian, the basic ideas can be illustrated in the case of electrons interacting with nuclei and themselves via Coulomb forces.

Due to the electron-electron interactions, the electronic wavefunctions cannot be written as the product of individual electronic wavefunctions. Here, we suppose that the system is a perfect solid. Although, real solids aren't absolutely pure, and defects are all of great importance, the effects of imperfections can be treated as small perturbations on the properties of a perfect solid. Therefore, the electrostatic potential affecting an electron in the perfect crystalline solid will be periodic, with a periodicity of lattice vector $\mathbf{R}$,

$$v_{eff}\left(\mathbf{r}+\mathbf{R}\right)=v_{eff}\left(\mathbf{r}\right). \tag{2.31}$$

Considering that our system is composed by independent electrons, including the effect of core electrons in the periodic electrostatic potential $v_{eff}(\mathbf{r})$, each electron follows the single electron Schrödinger equation:

$$\hat{h}_{se}\psi=\left(-\frac{\mathbf{p}^2}{2}+v_{eff}\left(\mathbf{r}\right)\right)\psi=\epsilon_{se}\psi. \tag{2.32}$$

As Bloch's theorem[60] states, the eigenstates of this Hamiltonian with periodic potential can be chosen to have the form of a plane wave times a function with the periodicity of the lattice,

$$\psi_{n\mathbf{k}}\left(\mathbf{r}\right)=e^{i\mathbf{k}\cdot\mathbf{r}}u_{n\mathbf{k}}\left(\mathbf{r}\right), \tag{2.33}$$

where

$$u_{n\mathbf{k}}\left(\mathbf{r}+\mathbf{R}\right)=u_{n\mathbf{k}}\left(\mathbf{r}\right), \tag{2.34}$$

and $\mathbf{k}$ is the real wave vector, that follows the Born-Von Karman boundary condition.

Generally speaking, the solution introduced by Bloch's theorem is not a eigenstate of the momentum operator, $\mathbf{p}=\frac{1}{i}\nabla$. So the wave vector $\mathbf{k}$, which can be always confined to the first Brillouin zone, is not proportional to the electronic momentum. This can be shown applying $\mathbf{p}$ to $\psi_{n\mathbf{k}}$:

$$\mathbf{p}\psi_{n\mathbf{k}}=\frac{1}{i}\nabla\left(e^{i\mathbf{k}\cdot\mathbf{r}}u_{n\mathbf{k}}\left(\mathbf{r}\right)\right)=\mathbf{k}\psi_{n\mathbf{k}}+\frac{e^{i\mathbf{k}\cdot\mathbf{r}}}{i}\nabla u_{n\mathbf{k}}\left(\mathbf{r}\right), \tag{2.35}$$

which is not a constant times $\psi_{n\mathbf{k}}$.

Bloch's theorem also introduces an additional n index because for each wave vector there are many solutions to the Scrhödinger equation. Each solution for a given wave vector has, in principle, different eigenvalue and eigenstate, which are labelled by the index n. Since $u_{n\mathbf{k}}(\mathbf{r})$ has the same periodicity of $v_{eff}(\mathbf{r})$, the wavefunctions can be expanded using the plane-wave basis set:

$$\psi_{n\mathbf{k}}(\mathbf{r}) = \frac{1}{\sqrt{V}} \sum_{\mathbf{G}} C_{n\mathbf{k}}(\mathbf{G})\, e^{i(\mathbf{k}+\mathbf{G})\cdot\mathbf{r}}, \tag{2.36}$$

where $C_{n\mathbf{k}}(\mathbf{G})$ are the plane-wave expansion coefficients, V is the total volume and $\mathbf{G}$ denotes the reciprocal lattice vectors. Introducing this expansion into the Kohn-Sham equations eq. (2.23), a set of matrix equations for the $C_{n\mathbf{k}}(\mathbf{G})$ is obtained:

$$\sum_{\mathbf{G}'} \left[-\frac{1}{2} |\mathbf{k}+\mathbf{G}|^2 \delta_{\mathbf{G}\mathbf{G}'} + \langle \mathbf{k}+\mathbf{G} | v_{eff}(\mathbf{r}) | \mathbf{k}+\mathbf{G}' \rangle \right] C_{n\mathbf{k}}(\mathbf{G}') = \epsilon_{n\mathbf{k}} C_{n\mathbf{k}}(\mathbf{G}). \tag{2.37}$$

Here, the matrix elements of the effective potential are:

$$\langle \mathbf{k}+\mathbf{G} | v_{eff}(\mathbf{r}) | \mathbf{k}+\mathbf{G}' \rangle = \int d\mathbf{r} e^{-i(\mathbf{k}+\mathbf{G})\cdot\mathbf{r}} v_{eff}(\mathbf{r})\, e^{i(\mathbf{k}+\mathbf{G}')\cdot\mathbf{r}}. \tag{2.38}$$

Usually, the effective potential is a functional of the valence electron density $n_v(\mathbf{r})$ only, instead of the total electron density. In this way, core and valence electrons are separated. Core electrons are treated as static and localized. On the other hand, valence electrons are much more delocalized and free to interact with the environment, making them responsible of most of the physical properties of solids. Furthermore, oscillations of the potential around atomic nuclei make necessary to include a large number of plane waves. The pseudopotential approximation assumes that only valence electrons enters in the Kohn-Sham equation, decreasing the cost of solving the problem significantly.

The construction of the pseudopotential for an isolated atom of a given element also contains some approximation[61, 62, 63, 64, 65], as it is a many body problem. It starts solving the atomic Schrödinger equation for all electrons, obtaining the corresponding exact eigenfunctions and eigenvalues. Then, the pseudowavefunction $\psi^{ps}(\mathbf{r})$ is constructed for each valence electron, which must be equal the exact wavefunction beyond a cutoff radius R_c. For $r < R_c$ the pseudowavefunction $\psi^{ps}(\mathbf{r})$ should smoothly vanish as r goes to 0. The pseudopotential $V^{ps}(\mathbf{r})$ is numerically calculated at every point in

real space from the Schrödinger equation of $\psi^{ps}(\mathbf{r})$:

$$\left(-\frac{1}{2}\nabla^2 + V^{ps}(\mathbf{r})\right)\psi^{ps}(\mathbf{r}) = \epsilon\psi^{ps}(\mathbf{r}). \tag{2.39}$$

In order to avoid numerical problems, $\psi^{ps}(\mathbf{r})$ should be nodeless. Now we have all the elements to solve Kohn-Sham equation, eq. (2.23).

2.1.5 Solving Kohn-Sham equations

After knowing the pseudopotetial of atoms of the studied system, Kohn-Sham equations can be solved self-consistently for valence electrons. At first, an initial guess is made for the electron density $n_i(\mathbf{r})$ and the corresponding effective potential $v_{eff}(\mathbf{r})$ is calculated. With this $v_{eff}(\mathbf{r})$ the Kohn-Sham equation is solved in a set of k-points diagonalizing in the plane wave basis,

$$\left[-\frac{1}{2}\nabla^2 + v_{eff}(\mathbf{r})\right]\psi_i(\mathbf{r}) = \epsilon_i\psi_i(\mathbf{r}). \tag{2.40}$$

The diagonalization of the Kohn-Sham equation yields a set of eigenvalues ϵ_i and eigenfunctions $\psi_i(\mathbf{r})$. From the solution of eq. (2.40) the final electron density $n_f(\mathbf{r})$ is obtained and compared with the initial electron density $n_i(\mathbf{r})$. If the electron density is not selfconsistent, a new initial electron density is guessed, which is based on the previous step, until the converge is achieved. Once this happens, output quantities, as energy or charge, are calculated.

2.2 Maximally localized Wannier functions

In the previous section we constructed the solution of the many-body problem in a set of functions known as Bloch orbitals $|\phi_{n\mathbf{k}}\rangle$, which were expanded in a plane wave basis set in eq. (2.36). One can change to a different set of functions through linear combinations of $|\phi_{n\mathbf{k}}\rangle$, in particular, to a local and orthonormal bases. This method was introduced in 1937 by G. H. Wannier[66] and has been developed since then. The basis set introduced in this method are a set of Wannier Functions (WF), which are orthonormal functions, defined as:

$$|\mathbf{R}n\rangle = \frac{1}{\sqrt{N}}\sum_{\mathbf{k}} e^{-i\mathbf{k}\cdot\mathbf{R}}|\phi_{n\mathbf{k}}\rangle, \tag{2.41}$$

with $\langle \mathbf{r}|\mathbf{R}n\rangle = w_{n\mathbf{R}}(\mathbf{r})$ and N is the number of mesh points in the Brillouin Zone. Note that this is the Fourier transform of Bloch orbitals from k-space to real space. The inverse relation is

$$|\phi_{n\mathbf{k}}\rangle = \frac{1}{\sqrt{N}} \sum_{\mathbf{R}} e^{i\mathbf{k}\cdot\mathbf{R}} |\mathbf{R}n\rangle . \tag{2.42}$$

Equations (2.41) and (2.42) define a linear transformation between Bloch functions and WFs. Even though WFs are not eigenstates of the Hamiltonian, both sets are, in principle, an equally acceptable basis for the description of electronic properties.

2.2.1 Gauge freedom

Bloch orbitals have an indeterminate phase in **k**-space. Therefore, we can define the equally valid orbital $\left|\tilde{\phi_{n\mathbf{k}}}\right\rangle$ as

$$\left|\tilde{\phi_{n\mathbf{k}}}\right\rangle = e^{i\varphi(\mathbf{k})} |\phi_{n\mathbf{k}}\rangle , \tag{2.43}$$

where $\varphi(\mathbf{k})$ is real and periodic in reciprocal space. This property of Bloch orbitals is called "gauge freedom" and it can be used to get WFs that are localized in real space. So, the smoother the Bloch orbital we chose, the more localized the WFs.

One can also generalize the gauge freedom of Bloch orbitals to

$$\left|\tilde{\phi_{n\mathbf{k}}}\right\rangle = \sum_{m=1}^{M} U_{mn}^{(\mathbf{k})} |\phi_{m\mathbf{k}}\rangle , \tag{2.44}$$

with $U_{mn}^{(\mathbf{k})}$ a M x M unitary matrix. Notice that eq. (2.43) is the special case where $U_{mn}^{(\mathbf{k})}$ is diagonal. Generally speaking, off-diagonal elements of $U_{mn}^{(\mathbf{k})}$ mix the contribution of several Bloch orbitals, which results in a transformed function $\left|\tilde{\phi_{n\mathbf{k}}}\right\rangle$ that is not an eigenstate of the Hamiltonian. Therefore, n cannot be identified as a real band index, it corresponds to a mixture of bands.

In order to get well-localized WFs, one has to construct smooth transformed functions $\left|\tilde{\phi_{n\mathbf{k}}}\right\rangle$. So, WFs are defined as:

$$|\mathbf{R}n\rangle = \frac{1}{\sqrt{N}} \sum_{\mathbf{k}} e^{-i\mathbf{k}\cdot\mathbf{R}} \left|\tilde{\phi_{n\mathbf{k}}}\right\rangle = \frac{1}{\sqrt{N}} \sum_{\mathbf{k}} e^{-i\mathbf{k}\cdot\mathbf{R}} \sum_{m=1}^{M} U_{mn}^{(\mathbf{k})} |\phi_{m\mathbf{k}}\rangle . \tag{2.45}$$

In this case, $U_{mn}^{(\mathbf{k})}$ should be rotated to cancel inherent discontinuities of Bloch orbitals and get well-localized WFs. In the general case, doing this is more complex than it seems. Firstly, degeneracies of different bands can occur for some $\mathbf{k}$. Bloch orbitals corresponding to degenerate bands at those points are not analytic, so the Fourier transform may be problematic. Secondly, and more important, it is not clear how should one chose the $U_{mn}^{(\mathbf{k})}$ matrix to have every transformed function $\left|\tilde{\phi_{n\mathbf{k}}}\right\rangle$ smooth in $\mathbf{k}$-space. Remind that one mixes contributions of several bands with $U_{nm}^{(\mathbf{k})}$, so trying to improve the smoothness of one band may worsen the smoothness of another one.

2.2.2 Marzari-Vanderbilt localization functional

Marzari and Vanderbilt developed in 1997[67] a method for determining the optimally localized set of WFs, and later it was generalized to the case of entangled bands by Souza, Marzari and Vanderbilt[68]. This method uses the next localization functional:

$$\Omega = \sum_n \left[\left\langle \mathbf{0}n \left| r^2 \right| \mathbf{0}n \right\rangle - \left\langle \mathbf{0}n \left| \mathbf{r} \right| \mathbf{0}n \right\rangle^2\right] = \sum_n \left[\left\langle r^2 \right\rangle_n - \bar{\mathbf{r}}_n^2\right]. \tag{2.46}$$

This functional measures the sum of quadratic spreads of desired WFs in the home unit cell around their centers. The functional can be decomposed into gauge invariant (Ω_I) and gauge dependent ($\tilde{\Omega}$) parts,

$$\Omega = \Omega_I + \tilde{\Omega}, \tag{2.47}$$

where

$$\Omega_I = \sum_n \left[\left\langle \mathbf{0}n \left| r^2 \right| \mathbf{0}n \right\rangle - \sum_{\mathbf{R}m} \left|\left\langle \mathbf{R}m \left| \mathbf{r} \right| \mathbf{0}n \right\rangle\right|^2\right] \tag{2.48}$$

and

$$\tilde{\Omega} = \sum_n \sum_{\mathbf{R}m \neq \mathbf{0}n} \left|\left\langle \mathbf{R}m \left| \mathbf{r} \right| \mathbf{0}n \right\rangle\right|^2. \tag{2.49}$$

$\tilde{\Omega}$ and Ω_I are both positive. Moreover, Ω_I is also invariant under any arbitrary transformation of the Bloch orbitals.

At this point, in order to minimize Ω, one only has to minimize the gauge dependent part, $\tilde{\Omega}$. At the minimum point, the off-diagonal elements $\left|\left\langle \mathbf{R}m \left| \mathbf{r} \right| \mathbf{0}n \right\rangle\right|^2$ are the smallest, and so one reaches the best compromise in the simultaneous diagonalization in the desired subspace of Bloch orbitals. Blount[69] showed in 1962 that the matrix elements of the position operator between WFs take the form:

$$\left\langle \mathbf{R}n \left| \mathbf{r} \right| \mathbf{0}m \right\rangle = i\frac{V}{(2\pi)^3} \int d\mathbf{k} e^{i\mathbf{k}\cdot\mathbf{R}} \left\langle u_{n\mathbf{k}} \left| \nabla_{\mathbf{k}} \right| u_{m\mathbf{k}} \right\rangle \tag{2.50}$$

and

$$\left\langle \mathbf{R}n \left| r^2 \right| \mathbf{0}m \right\rangle = -\frac{V}{(2\pi)^3} \int d\mathbf{k} e^{i\mathbf{k}\cdot\mathbf{R}} \left\langle u_{n\mathbf{k}} \left| \nabla_{\mathbf{k}}^2 \right| u_{m\mathbf{k}} \right\rangle , \tag{2.51}$$

where V is the real-space primitive cell volume. Using these expressions we can express the localization functional Ω in terms of $\nabla_{\mathbf{k}}$ and $\nabla_{\mathbf{k}}^2$, connecting WFs to the Bloch formalism. They also allow us to calculate the effects of localization of any unitary transformation of $|u_{n\mathbf{k}}\rangle$ without having to recalculate scalar products, which are computationally expensive. So, we determine the Bloch orbitals $|u_{n\mathbf{k}}\rangle$ on a regular k-point grid and use finite differences to evaluate the derivatives

$$\nabla_{\mathbf{k}} |u_{n\mathbf{k}}\rangle = \sum_{\mathbf{b}} c_{\mathbf{b}} \mathbf{b} \left(|u_{n\mathbf{k}+\mathbf{b}}\rangle - |u_{n\mathbf{k}}\rangle \right) + \mathcal{O}\left(b^2\right) , \tag{2.52}$$

where $\mathbf{b}$ are reciprocal vectors connecting nearest neighbour k-points and $c_{\mathbf{b}}$ the associated weights[67, 70]. In a similar way,

$$\left[\nabla f(\mathbf{k})\right]^2 |u_{n\mathbf{k}}\rangle = \sum_{\mathbf{b}} c_{\mathbf{b}} \left(|u_{n\mathbf{k}+\mathbf{b}}\rangle - |u_{n\mathbf{k}}\rangle \right)^2 + \mathcal{O}\left(b^3\right) . \tag{2.53}$$

Now we can calculate the matrix elements in eq. (2.50) and eq. (2.51). The overlaps $M_{mn}(\mathbf{k}, \mathbf{b})$ between Bloch orbitals at neighbouring $\mathbf{k}$ points now have all the information needed for the reciprocal space derivatives:

$$M_{mn}(\mathbf{k}, \mathbf{b}) \equiv \langle u_{m\mathbf{k}} | u_{n\mathbf{k}+\mathbf{b}} \rangle . \tag{2.54}$$

The overlap matrices are obtained iteratively updating the rotation matrix $M_{mn}(\mathbf{k}, \mathbf{b})$ in each iteration to minimize the global spread Ω.

This method results on a special type of WFs called Maximally Localized Wannier Functions (MLWFs) with the desired properties. First, they form the set of WFs with the highest level of localization[71]. Second, the localization of MLWFs is exponential. If spin-orbit coupling is not taken into account, the MLWFs are real. Last, this procedure permits to fix the arbitrary phase of Bloch orbitals in a large variety of systems.

2.2.3 Disentanglement procedure

The MLWFs obtained by the method introduced above describe correctly an isolated set of bands, such as valence states in an insulator. However, we need to introduce the disentanglement procedure[68] to obtain MLWFs for entangled bands that appear in metallic systems or the conduction bands of an insulator. This procedure requires defining an energy window, which

is called the outer window. For a k-point $\mathbf{k}$, there are $N_{win}^{(\mathbf{k})}$ states within the energy window. At each k-point, we perform a unitary transformation amongst the Bloch states which fall inside the energy window to obtain a set of N Bloch states,

$$\left|u_{n\mathbf{k}}^{opt}\right\rangle = \sum_{m \in N_{win}^{(\mathbf{k})}} U_{mn}^{dis(\mathbf{k})} \left|u_{m\mathbf{k}}\right\rangle , \tag{2.55}$$

where $\mathbf{U}^{dis(\mathbf{k})}$ is a rectangular N x $N_{win}^{(\mathbf{k})}$ matrix, and so $\left(\mathbf{U}^{dis(\mathbf{k})}\right)^{\dagger} \mathbf{U}^{dis(\mathbf{k})} = \mathbb{1}$. The set of $\mathbf{U}^{dis(\mathbf{k})}$ are obtained by minimising Ω_I within the outer energy window. Later on, the Marzari-Vandervilt localization functional can be used to minimise $\tilde{\Omega}$ and to obtain the MLWFs for this subspace.

The mixing between states in this subspace may lead to energy bands that do not correspond to any of the original energy bands. Also, a second energy window, the inner, or frozen, energy window, can be defined to preserve exactly the properties of a system in a given energy range. States that lies within this energy window are introduced unchanged in the optimal subspace.

2.2.4 Construction and reduction of the Wannier Hamiltonian for a 3d magnetic impurity

Once $\mathbf{U}^{dis(\mathbf{k})}$ and $\mathbf{U}^{(\mathbf{k})}$ are known, we can write the Hamiltonian in the basis of MLWFs[47]. For this, we start expressing the Hamiltonian in the basis of rotated Bloch states,

$$\mathbf{H}^{(W)}(\mathbf{k}) = \left(\mathbf{U}^{(\mathbf{k})}\right)^{\dagger} \left(\mathbf{U}^{dis(\mathbf{k})}\right)^{\dagger} H(\mathbf{k}) \mathbf{U}^{dis(\mathbf{k})} \mathbf{U}^{(\mathbf{k})}. \tag{2.56}$$

And then, we find its Fourier representation,

$$H_{nm}(\mathbf{R}) = \frac{1}{N_0} \sum_{\mathbf{k}} e^{-i\mathbf{k}\cdot\mathbf{R}} H_{nm}^{(W)}(\mathbf{k}) . \tag{2.57}$$

This is performed once and for each of the N_0 lattice vectors $\mathbf{R}$ that lie in a supercell conjugate to the k-mesh. $H_{nm}(\mathbf{R})$ decay quickly with R because the strong localisation of the MLWFs. For notation clarity, hereafter we should denote the Hamiltonian matrix at $\mathbf{R} = \mathbf{0}$ as $\mathbf{H}$.

This Wannier Hamiltonian can be diagonalized to obtain its eigenvalues ϵ_M and eigenvectors $|M\rangle$:

$$\mathbf{H}\left|M\right\rangle = \epsilon_M \left|M\right\rangle . \tag{2.58}$$

Introducing this Hamiltonian in a multiorbital Hubbard model, which is our goal, is computationally very expensive. So, we reduce the dimension of the Hamiltonian taking only the most relevant orbitals.

If we select the basis of the MLWFs in the correct order, we can write the Wannier $N_t \times N_t$ Hamiltonian as

$$\mathbf{H} = \begin{pmatrix} \mathbf{H}_{sd} & \mathbf{V}_{sd,j} & \mathbf{V}_{sd,\alpha} \\ \mathbf{V}_{j,sd} & \mathbf{H}_{j} & \mathbf{V}_{j,\alpha} \\ \mathbf{V}_{\alpha,sd} & \mathbf{V}_{\alpha,j} & \mathbf{H}_{\alpha} \end{pmatrix}, \tag{2.59}$$

where $\mathbf{H}_{sd}$ is the Hamiltonian corresponding to s and d orbitals of the magnetic atom, which is a 6×6 matrix or 5×5 matrix depending on whether it is necessary to include the s orbital or not. The block $\mathbf{H}_j$ contains the subspace of the Wannier Hamiltonian that are hybridized with the d-orbitals of the magnetic atom. Finally, the $\mathbf{H}_\alpha$ is the remaining subspace Hamiltonian, which contains the orbitals that are not hybridized with the d-orbitals of the magnetic atom. Notice that all these blocks, $\mathbf{H}_{sd}$, $\mathbf{H}_j$ and $\mathbf{H}_\alpha$, are square matrices which interact by the hopping matrices $\mathbf{V}_{i,k}$ (with $i \neq k$).

In order to decide which orbitals are hybridized with the d-orbitals of the magnetic atom, we diagonalize the Wannier Hamiltonian and obtain the weight of each eigenvector $|M\rangle$ on the subspace of d-orbitals:

$$W_d^M = \sum_{k \in d} |\langle M|k\rangle|^2 . \tag{2.60}$$

Notice that in so doing, we are labelling the MLWFs centred on magnetic impurity as s or d orbitals. Now we introduce a threshold weight Δ_d and the corresponding eigenvalues $\epsilon_{\mathcal{M}}$ and eigenvectors $|\mathcal{M}\rangle$ such that $W_d^{\mathcal{M}} \geq \Delta_d$. One can also introduce the weights on any MLWF, $W_k^{\mathcal{M}} = |\langle \mathcal{M}|k\rangle|^2$ and a second threshold Δ_k. The subspace of MLWFs hybridized with the d-orbitals of the magnetic impurity is then define by the N vectors $|k\rangle$ that satisfy the conditions:

$$W_d^{\mathcal{M}} \geq \Delta_d \tag{2.61}$$

$$W_k^{\mathcal{M}} \geq \Delta_k \tag{2.62}$$

Notice that the smaller Δ_d and Δ_k, the larger the dimension N of the reduced Hamiltonian. If we introduce the eigenvalues and eigenvectors of the reduced Hamiltonian $\mathbf{H}_{New}$ as $\mathbf{H}_{New}\left|M^P\right\rangle = \epsilon_M^P \left|M^P\right\rangle$, with $M \in [1, N]$, ideally we should have $\left|\epsilon_M - \epsilon_M^P\right| \to 0$ and $\sum_{k \in N} W_k^{\mathcal{M}} \to 1$. These conditions are trivially found when $\mathbf{V}_{sd,\alpha} = \mathbf{V}_{j,\alpha} = 0$ or when $N = N_t$.

The new reduced Hamiltonian will have the form

$$\mathbf{H}_{New} = \begin{pmatrix} \mathbf{H}'_{sd} & \mathbf{V}'_{sd,j} \\ \mathbf{V}'_{j,sd} & \mathbf{H}'_{j} \end{pmatrix}. \tag{2.63}$$

Since the MLWFs on the subspace belonging to $\mathbf{H}_\alpha$ are only weakly hybridized to the N subspace, the new Hamiltonian $\mathbf{H}_{New}$ can be derived

treating the effect of the hoppings $\mathbf{V}_{sd,\alpha}$ and $\mathbf{V}_{j,\alpha}$ perturbatively, following the Feshbach-Schur perturbative method[72]. Thus, it is given by

$$\mathbf{H}_{New}(\lambda) \approx H_P - PVR_\lambda VP, \tag{2.64}$$

where $P = \sum_{k\in N} |k\rangle \langle k|$ and $Q = \mathbb{1} - P$ are the projectors on the hybridized space and remaining space respectively, $H_P = P\mathbf{H}P$ and the resolvent R_λ is defined as

$$R_\lambda = Q\left(Q\mathbf{H}Q - \lambda\mathbb{1}\right)^{-1} Q. \tag{2.65}$$

The resulting effective Hamiltonian $\mathbf{H}_{New}(\lambda)$ is defined parametrically in terms of the energy λ. The closer λ to the actual eigenvalues $\epsilon_{\mathcal{M}}$, the more accurate is the representation given by $\mathbf{H}_{New}(\lambda)$. Notice that this method works well when the energy spectra of $\mathbf{H}_{sd}$ and $\mathbf{H}_j$ is far from the energy spectra of $\mathbf{H}_\alpha$, which means that there is a gap between eigenvalues of $\mathbf{H}_{sd} \oplus \mathbf{H}_j$ and $\mathbf{H}_\alpha$. However, this may not be the case of magnetic adatoms on top of metal surfaces. In systems where there is a strong coupling between orbitals of the magnetic atom and neighbouring atoms, the MLWFs may not provide a good description. In these cases, linear combinations of atomic orbitals (LCAO)[73], which are called ligand orbitals, provide a much better description of the system. The property that make ligand orbitals more convenient is that *d*-orbitals of the magnetic atom will coupled only to some linear combinations of orbitals of neighbouring atoms, depending on the symmetries of the environment. The idea in these cases is to change the basis set of the orbitals of neighbouring atoms to a more suitable one. First, we define the Hamiltonian

$$\mathbf{H}_{Neig} = \begin{pmatrix} \mathbf{H}_j & \mathbf{V}_{j,\alpha} \\ \mathbf{V}_{\alpha,j} & \mathbf{H}_\alpha \end{pmatrix}. \tag{2.66}$$

By diagonalizing this Hamiltonian, we get its eigenvalues ϵ_m^{Neig} and eigenvectors $|m_{Neig}\rangle$. Therefore, we can define the diagonal matrix,

$$\mathbf{H}_{Neig}^{(dia)} = \mathcal{V}^T \cdot \mathbf{H}_{Neig} \cdot \mathcal{V}, \tag{2.67}$$

where $\mathcal{V}$ is the matrix formed by all $|m_{Neig}\rangle$. With this matrix, we can define the rotation matrix U that acts on $\mathbf{H}$ as

$$U \equiv \mathbb{1}_{sd} \otimes \mathcal{V}. \tag{2.68}$$

Hence, the rotated Hamiltonian will take the form

$$\mathbf{H}^{ROT} = U^T \cdot \mathbf{H} \cdot U = \begin{pmatrix} \mathbf{H}_{sd} & \mathbf{V'}_{sd,j} & \mathbf{V'}_{sd,\alpha} \\ \mathbf{V'}_{j,sd} & \mathbf{H}_j^{(dia)} & \mathbf{0} \\ \mathbf{V'}_{\alpha,sd} & \mathbf{0} & \mathbf{H}_\alpha^{(dia)} \end{pmatrix}. \tag{2.69}$$

We can now apply the same procedure described above in this section to this rotated Hamiltonian $\mathbf{H}^{ROT}$. In the next section we will introduce the reduced Wannier Hamiltonian in the Multiorbital Hubbard model to describe the crystal and ligand field in the Hamiltonian.

2.3 Multiorbital Hubbard model

As mentioned in the previous chapter, the main goal of the work is to calculate electronic and magnetic properties of strongly correlated materials. With that purpose, we use a multiorbital Hubbard model[74, 75, 76, 77, 78, 79]. Therefore, our aim is to build a many-body Hamiltonian, derived from DFT calculations that accounts for the strong correlation of the system. This approach describes the spin excitations correctly in systems where charge redistribution and lattice deformation are negligible.

We model the magnetic atom on a substrate by a many-body Hamiltonian for N_e electrons,

$$H = \lambda_{Coul} H_{Coul} + \lambda_{CF} H_{CF} + \lambda_{SO} H_{SO} + H_{Zeem}. \tag{2.70}$$

We introduce the dimensionless λ_i parameters to switch off each interaction independently for analysis, where the physical situation would correspond to $\lambda_i = 1$. Here, H_{Coul} refers to the electron-electron Coulomb interaction, H_{CF} accounts for the crystal and ligand field, H_{SO} is the spin-orbit interaction and H_{Zeem} is the Zeeman interaction, which appears in the presence of a magnetic field.

2.3.1 Electron-electron Coulomb interaction

The first term in eq. (2.70) refers to the Coulomb interaction between electrons in the s and d-shells of the magnetic atom, and it can be expressed by:

$$H_{Coul} = \frac{1}{2} \sum_{\substack{m,m' \\ n,n'}} V \sum_{\sigma,\sigma'} d^{\dagger}_{m\sigma} d^{\dagger}_{n\sigma'} d_{n'\sigma'} d_{m'\sigma} - E_d \sum_{m} \hat{n}_m, \tag{2.71}$$

where $d^{\dagger}_{m\sigma}$ ($d_{m\sigma}$) denotes the creation (annihilation) operator of an electron with spin σ in orbital m of the magnetic atom. Coulomb integrals $V_{mnm'n'}$ are calculated numerically. The second term controls the occupation of orbitals of the magnetic atom. This occupation can fluctuate in one electron due to hoppings to orbitals of neighbouring atoms. The effective $U_{dd} = \langle V_{mmmm} \rangle$ repulsion characterizes the strength of Coulomb integrals,

while $\hat{n_m} = \sum_\sigma d^\dagger_{m\sigma} d_{m\sigma}$ is the occupation of the m-orbital. E_d controls the electron transfer between the d-shell of the magnetic atom and neighbouring atoms orbitals.

2.3.2 Crystal and ligand field

The second term in eq. (2.70) corresponds to the crystal and ligand fields Hamiltonian, that we write as

$$H_{CF} = H_{MA} + H_{neigh} + \lambda_{hopp} H_{hopp}, \tag{2.72}$$

where H_{MA} is the crystal field acting only on the electrons of the magnetic atom. We assume that it is given by

$$H_{MA} = \sum_{m,m'} \langle m \left| H_{CF} \right| m' \rangle \sum_\sigma d^\dagger_{m\sigma} d_{m'\sigma}, \tag{2.73}$$

with $\langle m \left| H_{CF} \right| m' \rangle = \left\langle m \left| H^{ROT} \right| m' \right\rangle$ derived from DFT, using the procedure described in the previous section, or extracted from a point charge model.

In eq. (2.72), we also consider contributions to the crystal field due to electrons on neighbouring atoms in the next form:

$$\begin{aligned} &H_{neigh} + \lambda_{hopp} H_{hopp} = \\ &\sum_{j,k,\sigma} \left\langle j \left| H^{ROT} \right| k \right\rangle p^\dagger_{j\sigma} p_{k\sigma} + \lambda_{hopp} \sum_{m,k,\sigma} \left(\left\langle m \left| H^{ROT} \right| k \right\rangle d^\dagger_{m\sigma} p_{k\sigma} + h.c. \right), \end{aligned} \tag{2.74}$$

where $p^\dagger_{j,\sigma}$ ($p_{j,\sigma}$) denotes the creation (annihilation) operator of a pseudoparticle with spin σ in the j orbital of a neighbouring atom. The parameter λ_{hopp} is used also for analysis reasons, as it permits us to decouple the contributions from the magnetic atoms and the hybridizations with other orbitals.

2.3.3 Spin-orbit and Zeeman interaction

The last two terms in eq. (2.70) are the spin-orbit interaction and the Zeeman interaction. The spin-orbit interaction is described by:

$$H_{SO} = \zeta \sum_{\substack{mm' \\ \sigma\sigma'}} \left\langle m\sigma \left| \vec{l} \cdot \vec{S} \right| m'\sigma' \right\rangle d^\dagger_{m\sigma} d_{m'\sigma'}, \tag{2.75}$$

where ζ is the single particle spin-orbit coupling parameter of d electrons. Notice that we have assumed that this term is non-zero only on the orbitals of the magnetic atom.

On the other hand, the Zeeman interaction, which appears when a magnetic field is applied to the system, can be written as:

$$\begin{aligned} H_{Zeem} &= H_{Zeem-MA} + H_{Zeem-neigh} \\ &= \mu_B \vec{B} \cdot \sum_{\substack{mm' \\ \sigma\sigma'}} \left\langle m\sigma \left| \left(\vec{l} + g\vec{S} \right) \right| m'\sigma' \right\rangle d^{\dagger}_{m\sigma} d_{m'\sigma'} \\ &+ g m_P \left(\vec{B} \right) \vec{B} \sum_{\substack{jk \\ \sigma\sigma'}} \left\langle j\sigma \left| \vec{S} \right| k\sigma' \right\rangle p^{\dagger}_{j\sigma} p_{k\sigma'}, \end{aligned} \tag{2.76}$$

where $g = 2$ is the gyromagnetic factor of the electron and $m_P\left(\vec{B}\right) \approx \rho\left(\epsilon_F\right)\mu_B^2 \vec{B}$ is the spin magnetic moment in the Pauli's diamagnetism.

Notice that the order of the terms in eq. (2.70) is descendent. The first term, Coulomb interaction, splits the energy levels in some eV. The second term, the crystal and ligand field interaction, produces a splitting around 1 eV. The magnitude of the third term, the spin-orbit interaction, is some tens of meV. And finally, the splitting produced by the last term, the Zeeman interaction, is about some meV.

The next section describes the Configuration Interaction method (CI method), which will be used for solving the multiorbital Hubbard Hamiltonian described in this section.

2.4 Configuration Interaction method

The aim of the Configuration Interaction (CI method) method is to solve the time-independent electronic Schrödinger equation, eq. (2.70), for a system with N_e electrons. The many body Hamiltonian is spanned in the basis of configurations projected onto N_{orb} single particle orbitals. We shall illustrate this method for the simplest non-trivial case: the H_2 molecule, where we have 2 electrons in 2 s states. The Hubbard Hamiltonian in this case can be written as:

$$H = \sum_{i=1}^{2} U \hat{n}_{i\downarrow} \hat{n}_{i\uparrow} + V \sum_{i<j} \hat{n}_i \hat{n}_j - V^{Exc} \sum_{\substack{i<j \\ \sigma}} \hat{n}_{i\sigma} \hat{n}_{j\sigma} + t \sum_{\substack{i \neq j \\ \sigma}} c^{\dagger}_{i\sigma} c_{j\sigma}, \tag{2.77}$$

where the first term is the on-site repulsion interaction, the second term is the repulsion interaction between electrons in different states, the third term is the exchange term and the last term is the hopping term. Here we have introduced the creation (annihilation) operators $c^{\dagger}_{i\sigma}$ ($c_{i\sigma}$) of an electron in the

single particle state labelled by i, with spin σ; and the occupation operators $\hat{n}_{i\sigma} = c^{\dagger}_{i\sigma} c_{i\sigma}$ and $\hat{n}_i = \sum_\sigma \hat{n}_{i\sigma}$.

Each many body configuration $\Psi_{m_1,...,m_N}(\vec{r}_1, ..., \vec{r}_N)$ is given by Slater determinant

$$\Psi_{m_1,...,m_N}(\vec{r}_1, ..., \vec{r}_N) = \frac{1}{\sqrt{N!}} \begin{vmatrix} \psi_{m_1}(\vec{r}_1) & \cdots & \psi_{m_n}(\vec{r}_1) \\ \vdots & \ddots & \vdots \\ \psi_{m_1}(\vec{r}_N) & \cdots & \psi_{m_n}(\vec{r}_N) \end{vmatrix}, \tag{2.78}$$

where $\psi_m(\vec{r})$ are the product of orbital states $\xi_m(\vec{r})$ and a spinor χ_{m_s}, i. e.,

$$\psi_m(\vec{r}) = \xi_m(\vec{r}) \otimes \chi_{m_s}, \tag{2.79}$$

$\xi_n(\vec{r})$ were obtained before from the MLWFs.

The energy of single particle states has no upper bound. In consequence, we have an infinite number of single particle eigenvectors $\psi_m(\vec{r})$, and an infinite number of possible configurations. Nevertheless, the low energy states of N interacting particles system can be well approximated by a finite number of configurations n_C. This constitutes the bases of the CI method. The problem of N interacting particles is then solved by calculating eigenvalues and eigenfunctions of the $n_C \times n_C$ Hamiltonian matrix. This n_c is linked to the number of single particle orbitals N_{orb} and electrons N_e by

$$n_C = \frac{(2N_{orb})!}{(2N_{orb} - N_e)! N_e!}, \tag{2.80}$$

where the 2 reflects the possible spin orientations of electrons for each orbital. In the case of H_2 molecule, with $N_{orb} = N_e = 2$, the number of possible configurations is $n_C = 6$. This number increases rapidly with N_e and N_{orb}. For instance, lets consider a Co adatom on 3×3 hexagonal boron nitride (h-BN) supercell, which will be consider afterwards for DFT calculations. The system is composed by 9 N atoms ($9 \times 5 = 45$ electrons), 9 B atoms ($9 \times 3 = 27$ electrons) and 1 Co atom (9 electrons), $N_e = 81$ electrons. For B atoms and N atoms we consider only 1 s and 3 p orbitals, and for Co atom 1 s and 5 d orbitals, thus the number of orbitals introduced in the CI method are $N_{orb} = 78$ orbitals. So, in the system there are $n_C = 5.19 \times 10^{45}$ possible configurations.

The diagonalization of the Hamiltonian H becomes simpler if there is an observable $\hat{A}$ that commutes with it. In this case, an orthonormal basis can be constructed with eigenvectors common to $\hat{A}$ and H. Then, the matrix H is block diagonal in the basis of eigenvectors of $\hat{A}$, which makes the problem

much simpler. In the case of H_2 molecule, reflecting the spin-orbit coupling, $\hat{S}_z$ commute with H,

$$[H, S_z] = 0. \tag{2.81}$$

Therefore, the quantum number that defines eigenvalues of S_z is a good quantum number. For this reason, we will group the configurations that have the same value of S_z. As we have 2 electrons to distribute in 2 orbitals, from quantum mechanics, we know that the possible values are obtained from the equation

$$S_z \left|m_{s_1}; m_{s_2}\right\rangle = M_s \left|m_{s_1}; m_{s_2}\right\rangle, \tag{2.82}$$

where $M_s = m_{s_1} + m_{s_2}$ and $m_{s_i} = \pm 1/2$. The number of configuration for each eigenvalue of S_z is given by

$$n_{C_{S_z}} = \frac{N_{orb}!}{(N_{orb} - N_\downarrow)! N_\downarrow!} \frac{N_{orb}!}{(N_{orb} - N_\uparrow)! N_\uparrow!}, \tag{2.83}$$

where $N_\downarrow$ ($N_\uparrow$) is the number of electrons with spin down (up) for each eigenvalue, $N_e = N_\uparrow + N_\downarrow$. So, for the H_2 molecule, we have that the eigenvalues and eigenvectors of S_z are

$$\begin{array}{rcl} S_z = -1 & \rightarrow & |1_\downarrow, 2_\downarrow\rangle \\ S_z = 0 & \rightarrow & |1_\downarrow, 2_\uparrow\rangle \quad |1_\uparrow, 2_\downarrow\rangle \quad |1_\uparrow, 1_\downarrow\rangle \quad |2_\uparrow, 2_\downarrow\rangle \\ S_z = 1 & \rightarrow & |1_\uparrow, 2_\uparrow\rangle, \end{array} \tag{2.84}$$

The spins of both electrons that build the configuration with $S_z = 1$ will be up. The configurations built with one electron with spin up and the other spin down have the eigenvalue $S_z = 0$. And, the configuration with eigenvalue $S_z = -1$ is built with the spin of both electrons is down.

According to eq. (2.83), in subspaces of $S_z = \pm 1$ only 1 configuration is possible, $n_{C_1} = n_{C_{-1}} = 1$. As there cannot be two electrons with equal spin in the same orbital, due to the Pauli exclusion principle, the only way to distribute the electrons is placing one electron in each orbital. Thus, the Hamiltonian corresponding to these subspaces will be 1×1 matrices. On the other hand, there are 4 possible configurations in the subspace $S_z = 0$, $n_{c_0} = 4$, i. e., there are 4 possible ways to distribute the electrons with one spin up and one spin down. Therefore, the diagonal block of the Hamiltonian with $S_z = 0$ will be a 4×4 matrix.

Now we have to build the configurations for each subgroup. These Slater determinants will form the many-particle basis wavefunctions in which we will solve the Hamiltonian, eq. (2.77). For the eigenvalue $S_z = -1$ we have only one configuration,

$$\Psi_{1_\downarrow, 2_\downarrow}(\vec{r}_1, \vec{r}_2) = \frac{1}{\sqrt{2!}} \begin{vmatrix} \psi_{1_\downarrow}(\vec{r}_1) & \psi_{2_\downarrow}(\vec{r}_1) \\ \psi_{1_\downarrow}(\vec{r}_2) & \psi_{2_\downarrow}(\vec{r}_2) \end{vmatrix}. \tag{2.85}$$

For the eigenvalue $S_z = 0$, we have 4 configurations:

$$\Psi_{1_\downarrow,2_\uparrow}(\vec{r}_1,\vec{r}_2) = \frac{1}{\sqrt{2!}} \begin{vmatrix} \psi_{1_\downarrow}(\vec{r}_1) & \psi_{2_\uparrow}(\vec{r}_1) \\ \psi_{1_\downarrow}(\vec{r}_2) & \psi_{2_\uparrow}(\vec{r}_2) \end{vmatrix}, \tag{2.86}$$

$$\Psi_{1_\uparrow,2_\downarrow}(\vec{r}_1,\vec{r}_2) = \frac{1}{\sqrt{2!}} \begin{vmatrix} \psi_{1_\uparrow}(\vec{r}_1) & \psi_{2_\downarrow}(\vec{r}_1) \\ \psi_{1_\uparrow}(\vec{r}_2) & \psi_{2_\downarrow}(\vec{r}_2) \end{vmatrix}, \tag{2.87}$$

$$\Psi_{1_\uparrow,1_\downarrow}(\vec{r}_1,\vec{r}_2) = \frac{1}{\sqrt{2!}} \begin{vmatrix} \psi_{1_\uparrow}(\vec{r}_1) & \psi_{1_\downarrow}(\vec{r}_1) \\ \psi_{1_\uparrow}(\vec{r}_2) & \psi_{1_\downarrow}(\vec{r}_2) \end{vmatrix} \tag{2.88}$$

and

$$\Psi_{2_\uparrow,2_\downarrow}(\vec{r}_1,\vec{r}_2) = \frac{1}{\sqrt{2!}} \begin{vmatrix} \psi_{2_\uparrow}(\vec{r}_1) & \psi_{2_\downarrow}(\vec{r}_1) \\ \psi_{2_\uparrow}(\vec{r}_2) & \psi_{2_\downarrow}(\vec{r}_2) \end{vmatrix}. \tag{2.89}$$

Finally, for the eigenvalue $S_z = 1$ we have also only one configuration,

$$\Psi_{1_\uparrow,2_\uparrow}(\vec{r}_1,\vec{r}_2) = \frac{1}{\sqrt{2!}} \begin{vmatrix} \psi_{1_\uparrow}(\vec{r}_1) & \psi_{2_\uparrow}(\vec{r}_1) \\ \psi_{1_\uparrow}(\vec{r}_2) & \psi_{2_\uparrow}(\vec{r}_2) \end{vmatrix}. \tag{2.90}$$

It is particularly convenient to write the Slater determinants in terms of the creation operators,

$$|\alpha,\beta\rangle = c_\alpha^\dagger c_\beta^\dagger |0\rangle, \tag{2.91}$$

where $|0\rangle$ is the ground state of the vacuum and α and β are composed index (m,σ). And the corresponding ket in terms of annihilation operators is

$$\langle\alpha,\beta| = \langle 0| c_\beta c_\alpha. \tag{2.92}$$

Therefore, the CI basis written in terms of creation and annihilation operators is

$$\{|u\rangle, |a\rangle, |b\rangle, |c\rangle, |d\rangle, |v\rangle\}, \tag{2.93}$$

where

$$\begin{aligned} |u\rangle &= c_{1_\downarrow}^\dagger c_{2_\downarrow}^\dagger |0\rangle \\ |a\rangle &= c_{1_\uparrow}^\dagger c_{1_\downarrow}^\dagger |0\rangle \\ |b\rangle &= c_{1_\downarrow}^\dagger c_{2_\uparrow}^\dagger |0\rangle \\ |c\rangle &= c_{1_\uparrow}^\dagger c_{2_\downarrow}^\dagger |0\rangle \\ |d\rangle &= c_{2_\uparrow}^\dagger c_{2_\downarrow}^\dagger |0\rangle \\ |v\rangle &= c_{1_\uparrow}^\dagger c_{2_\uparrow}^\dagger |0\rangle \quad . \end{aligned} \tag{2.94}$$

We will write the configurations in terms of creation and annihilation operators to calculate Hamiltonian matrix elements in an easier way.

Once we have constructed each of the possible configurations, we can obtain the matrix elements of the Hamiltonian in this basis by,

$$H_{ij} = \langle \Psi_i | H | \Psi_j \rangle, \tag{2.95}$$

where we replace $\Psi_{a,b}(\vec{r}_1, \vec{r}_2)$ by $|\Psi_i\rangle$. For instance, lets calculate the first term:

$$\langle u|H|u\rangle = \langle 0| c_{1_\downarrow} c_{2_\downarrow} \left(\sum_{i=1}^{2} U n_{i_\downarrow} n_{i_\uparrow} + V \sum_{i<j} n_i n_j - V^{Exc} \sum_{\substack{i<j \\ \sigma}} n_{i_\sigma} n_{j_\sigma} + t \sum_{\substack{i\neq j \\ \sigma}} c^\dagger_{i_\sigma} c_{j_\sigma} \right) c^\dagger_{1_\downarrow} c^\dagger_{2_\downarrow} |0\rangle . \tag{2.96}$$

The first term in eq. (2.96) is 0 as there is no spin $\uparrow$ electron in $|u\rangle$ configuration and so $n_{i_\uparrow}|u\rangle = 0$. In the second term, there is only one element,

$$V \left\langle u \left| \sum_{i<j} n_i n_j \right| u \right\rangle = V \left\langle 0 \left| c_{2_\downarrow} c_{1_\downarrow} n_1 n_2 c^\dagger_{1_\downarrow} c^\dagger_{2_\downarrow} \right| 0 \right\rangle = V. \tag{2.97}$$

Similarly, the third term is

$$-V^{Exc} \left\langle u \left| \sum_{\substack{i<j \\ \sigma}} n_{i_\sigma} n_{j_\sigma} \right| u \right\rangle = -V^{Exc}. \tag{2.98}$$

The last term creates an electron in one orbital and annihilates in the other. All the terms that have the $\uparrow$ spin are 0 as there is no electron in $|u\rangle$ with $\uparrow$ spin. So, we will only consider terms with all operators for $\downarrow$ spin,

$$\langle 0| c_{2_\downarrow} c_{1_\downarrow} \left(t c^\dagger_{1_\downarrow} c_{2_\downarrow} + t c^\dagger_{2_\downarrow} c_{1_\downarrow} \right) c^\dagger_{1_\downarrow} c^\dagger_{2_\downarrow} |0\rangle = t\left(\langle 2_\downarrow | 1_\downarrow \rangle + \langle 1_\downarrow | 2_\downarrow \rangle \right) = 0 \tag{2.99}$$

Doing all the computation with all the elements, one can derive the next Hamiltonian matrix:

$$H = \begin{pmatrix} V - V^{Exc} & 0 & 0 & 0 & 0 & 0 \\ 0 & U & t & -t & 0 & 0 \\ 0 & -t & V & 0 & t & 0 \\ 0 & t & 0 & V & -t & 0 \\ 0 & 0 & -t & t & U & 0 \\ 0 & 0 & 0 & 0 & 0 & V - V^{Exc} \end{pmatrix}. \tag{2.100}$$

The eigenvalues obtained from the diagonalisation are

$$\begin{cases} E_1 &= \frac{1}{2}\left(U + V - \sqrt{16t^2 + (U-V)^2} \right) \\ E_2 = E_3 &= V - V^{Exc} \\ E_4 &= V \\ E_5 &= U \\ E_6 &= \frac{1}{2}\left(U + V + \sqrt{16t^2 + (U-V)^2} \right) \end{cases}. \tag{2.101}$$

Our multiplet calculations will be more complex, as we will work a larger number of orbitals and electrons. In spite of that, we will follow the procedure described above.

In the next chapter, we will use all these methods to extract magnetic properties of Co on h-BN, and associate them with different adsorption sites.

Chapter 3

Co ADATOM ON h-BN

The main goal of this chapter is to study the magnetic anisotropy energy (MAE), which has a critical role on the stability of a magnetic moment, of Co adatom on hexagonal boron nitride (h-BN), which we will use after as a decoupling layer from different metallic substrates. A large MAE avoids spin transitions due to, for example, thermal fluctuations, and it appears as a combination of the spin-orbit coupling and the appropriate crystal field symmetry. Even though the spin-orbit coupling strength of late $3d$ transition metal atoms is relatively low, around 50 meV; they can show large MAE values in special conditions. This is the case of single atoms and nanostructures of Co on Pt single crystals[9, 10].

In this chapter, we will study the interaction of Co with the h-BN from DFT+SOC calculations. In addition, we will also follow the procedure described by Ferron *et al.*[29, 30] to calculate magnetic properties of the system. This procedure is based on extracting the crystal field from first principle DFT calculations to build a many-body multiorbital Hubbard model that includes also spin-orbit and electron correlation effects, described in the previous chapter.

3.1 Properties of h-BN

The structure of h-BN is the same as that of graphene, sp^2-bonded honeycomb lattice. In h-BN, instead of having two C sublattices, one of the sublattices is composed of N atoms and the other one of B atoms. Therefore, h-BN is isostructural and isoelectronic to graphene, and it has 8 valence electrons per BN unit that are distributed in the in-plane σ and the out-of-plane π bonds[80]. The B-N bond-length of h-BN is also similar to the C-C bond-length of graphene, 1.44 Å and 1.42 Å respectively, which ends up in a

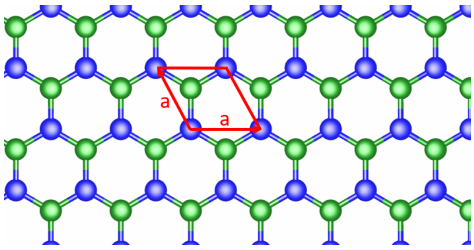

Figure 3.1: Top view of the h-BN where green spheres represent B atom and blue ones N atoms. The unit cell is represented by red lines, where a is the length of unit cell vectors.

small lattice mismatch between h-BN and graphene ($\approx 1.4\%$)[81].

However, h-BN has quite different electronic properties compared to graphene. The electronegativity of B and N atoms is different, which produces a considerable charge transfer from B to N. The N atom is negatively charged and the B atom positively, giving a ionic character to the bond and making the h-BN an insulator with a large band gap of about 6 eV[82, 83, 84]. Additionally, h-BN shows low defect density and high chemical and thermal stability, which makes it an excellent candidate as a decoupling layer from a metallic substrate. Other properties and applications of h-BN and its derivates can be found in the report by Willi Auwärter[80].

The first thing to do here is to model the h-BN, see fig. 3.1. For that, we need to calculate the lattice parameter of h-BN. We perform first-principles DFT calculations using VASP code with PAW potential. The total energy calculations have been carried out using the PBE parametrization of the GGA exchange and correlation functional. We set the energy cutoff of plane-waves in 500 eV and an energy convergence threshold of 10^{-5} eV. We select a $9 \times 9 \times 1$ Monkhorst-Pack Γ centered method for generating the k-mesh in these calculations.

The h-BN has a sp^2-bonded honeycomb structure. For convenience, the perpendicular vector to the h-BN plane will correspond to the Z axis. The remaining two vectors will form an angle of $2\pi/3$ in the XY plane, but they will be of the same length. We will call the length of this two vectors, a, the lattice parameter, and we will vary it to get its optimal value. We will keep constant the length of the perpendicular vector at 15 Å to avoid interaction due to periodic boundary conditions. Finally, a N atom is placed at the origin and a B atom at (1/3,2/3,0) fractional coordinates to form the structure of the h-BN showed in fig. 3.1.

Figure 3.2 shows the total energy of the system with respect to the lattice parameter, and it shows that the optimal lattice parameter is 2.51 Å. This

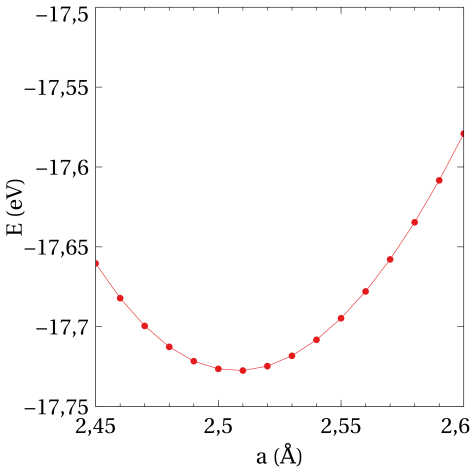

Figure 3.2: Calculation of the optimal lattice parameter.

lattice parameter is consistent with other DFT calculations, as the 2.50 Å obtained for LDA approximation[85]; but also by the experimental measurement of 2.48 ± 0.05 Å by Corso *et. al.*[86].

Then, we calculate the bandstructure of the system taking the k-points along high symmetry lines in the first Brillouin zone.

From the bandstructure in fig. 3.3, we can extract the band gap energy, E_{GAP}, which is 4.66 eV, in good agreement with other GGA calculation by Wang *et. al.*[87], who reported a band gap of 4.77 eV for a lattice parameter of 2.46 Å.

3.2 Adsorption of Co on h-BN

Once we have characterized the isolated h-BN, and taking into account that the main goal is to use the h-BN as a decoupling layer from metallic substrate, we build a 4×4 supercell, see fig. 3.4. That supercell is formed by two vectors of 9.80 Å length in the XY plane, with $2\pi/3$ angle, and one vector of 21.47 Å length in the perpendicular direction. We will use this unit cell after when the metallic substrate is included in the calculation. This supercell corresponds to a primitive unit cell with a lattice parameter slightly smaller, 2.45 Å, than the optimal one, but it will match with a rotation of metallic substrates analysed later in the thesis. In the 4×4 h-BN supercell, we will study the adsorption of Co in different sites. Taking that into account, the unit cell will be composed by 16 N atoms and 16 B atoms in the same XY plane, and 1 Co atom at higher Z coordinate.

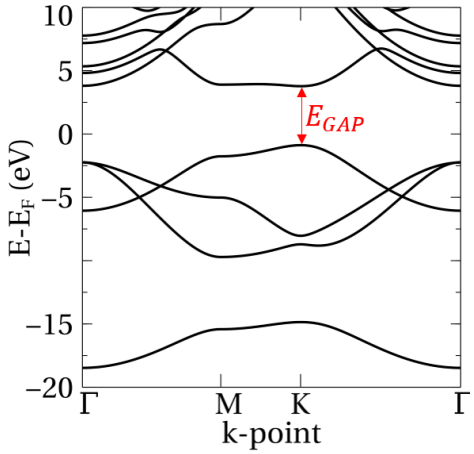

Figure 3.3: Calculated bandstructure of the isolated h-BN.

3.2.1 Non-spin-polarized DFT calculations

These DFT calculations were performed within the PAW method as it is implemented in VASP code. We used PBE for the exchange-correlation functional. Non-spin-polarized DFT calculations were performed using an energy cutoff of 400 eV and a gaussian smearing of 0.2 eV width. DFT-D2 method of Grimme[58] was used to include Van der Waals correction. For the study of the Co adsorption site we used a Γ only k-mesh. The relaxation of the system was performed until the forces were below 0.01 eV/Å.

Forces in planar 4×4 h-BN, without the Co adatom, are below 0.01 eV/Å so it does not need a relaxation. We take the energy of the planar 4×4 h-BN as the reference energy.

Then, we deposit a Co adatom atop N site, see fig. 3.4, and relax all the atoms in the unit cell in Z direction. This relaxation result on a small corrugation, around 0.4 Å of the 4×4 h-BN monolayer, with the Co atom placed 1.89 Å above one of the N atoms. The energy of this system is 2.41 eV lower than the reference. The interaction energy of the Co in this site is 1.66 eV, which is obtained by subtracting from the total energy of the system the energy of each component isolated.

For the hollow adsorption site in fig. 3.4, we repeat the same relaxation as for the atop site. This also results on a small corrugation of around 0.4 Å for the 4×4 h-BN, with the Co atom placed at 1.66 Å above the N underneath. In this case, the energy of the system is 2.15 eV smaller than the reference, and the interaction energy is 1.33 eV.

According to these results the Co adsorbs on atop N site, but it is close in energy, 261.1 meV, to the hollow site. Thus, we decide to perform more

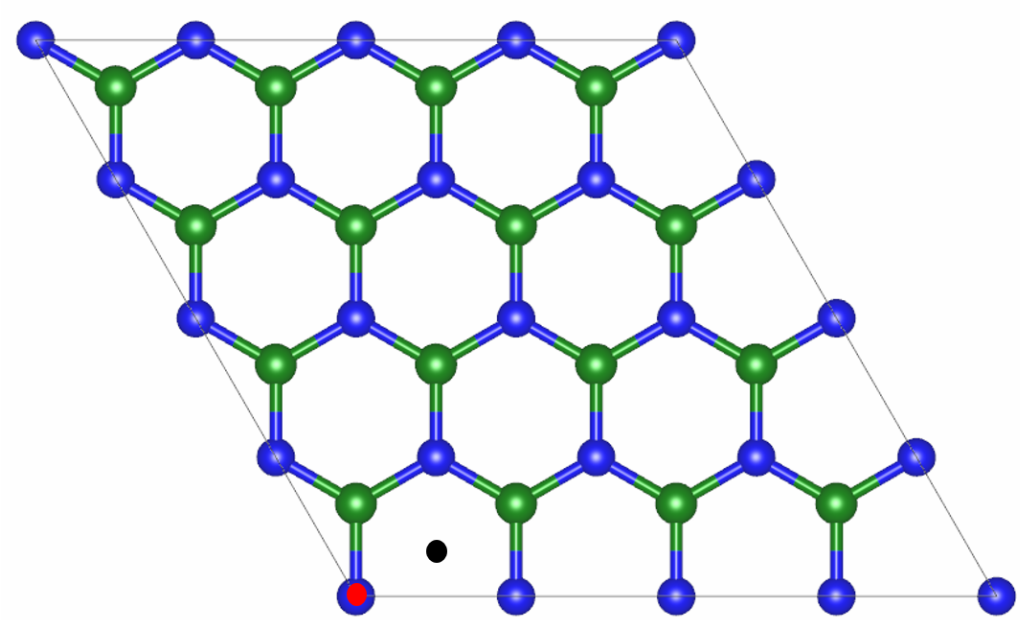

Figure 3.4: Top view of the unit cell, marked with grey lines, of the 4×4 h-BN where green spheres represent B atom and blue spheres N atoms. Red dot is the atop N adsorption site and black dot the hollow site.

realistic calculations, as spin-polarized calculations or DFT+U calculations.

3.2.2 Spin-polarized DFT and DFT+U calculations

We perform spin-polarized relaxation for both adsorption sites with parameters described previously. The energy difference between different adsorption sites is now reduced to 84.6 meV, but, contrary to the previous calculation, favourable to the hollow site.

As we expect, the bond distance increases when spin-polarized DFT calculations performed, in comparison with non-spin-polarized calculations. In the case of the atop N site the distance between Co adatom and the N atom below is 1.94 Å, increasing the Co-N bond length by 3% in comparison with non-spin-polarized calculations. For the hollow adsorption site, the height of the Co adatom from its first neighbour N atoms is 1.89 Å which represent an increase in the N-Co bond length of 9%.

From spin-polarized calculations we obtain the PDOS, shown in fig. 3.5, for both adsorption sites. The energy integration of these PDOS curves onto $3d$-states up to the Fermi level gives around 7.8 electrons in the d-shell of Co adatom in both cases, see table 3.1. The occupation of d-shell for the Co

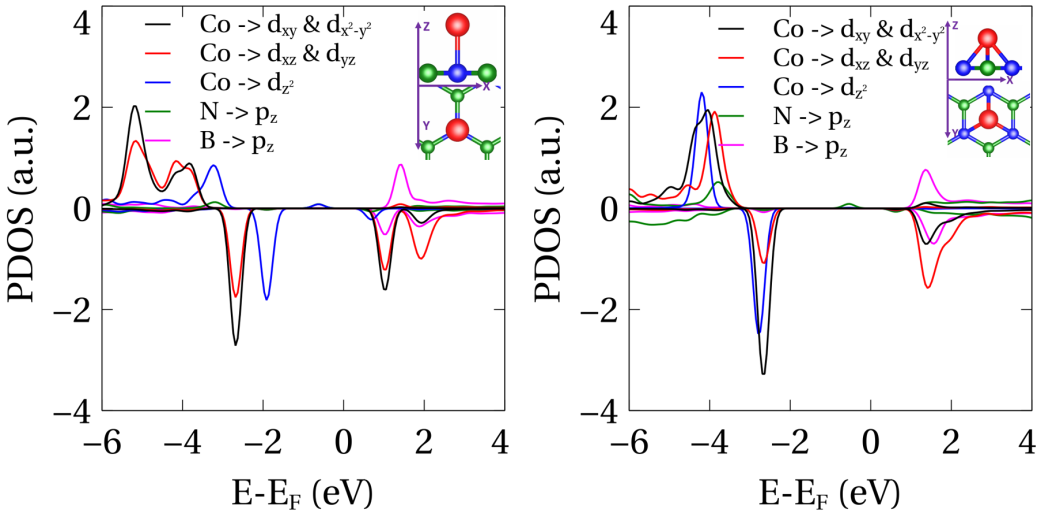

Figure 3.5: Projected density of states (PDOS) onto $3d$ orbitals of Co and p_z orbitals of first neighbour N and B atoms for atop N (left) and for hollw (right) adsorption sites, as obtained from the spin-polarized calculations. Positive values correspond to majority-spin and negative values to minority-spin. The insets shows the adsorption site, where the red spheres represents the Co adatom, while blue and green spheres represent N and B atoms, respectively.

adatom corresponds to a spin $S = 1$ localized in the $3d$ shell of Co.

The PDOS of both cases also reveals a weak hybridization between Co $3d$-states and h-BN $2p$-states, due to the presence of relatively sharp peaks, where practically the majority spin $3d$-states of the Co are occupied, but only three of the minority spin states. In the case of the atop adsorption, the weak hybridization corresponds to d_{z^2} state of Co with p_z state of N. The hollow case is more complicated, as it involves more states than in the atop N case, where the d_{yz} orbitals and d_{xz} of Co are hybridized with p_z of first neighbour N and B atoms.

Table 3.1: Populations and spin polarization of Co orbitals from spin-polarized DFT+U calculations.

	Total	$4s$	$3d$
Total charge	8.77	0.98	7.79
Spin up	5.80	0.87	4.93
Spin down	2.97	0.11	2.86
Polarization	2.83	0.76	2.07

In order to have more realistic results, we performed DFT+U calculations including vdW interaction for the spin-polarized system, which result in an energy difference of 367.9 meV favourable to the hollow site, in agreement with the work by Yazyev and Pasquarello [88]. In this energy range, which corresponds to the weak chemisoption regime, Van der Waals forces are playing an important role, and is difficult to determine accurately the adsorption site.

3.2.3 DFT+SOC calculations

DFT calculations including spin-orbit interaction are more expensive than DFT+U calculations and permit us to estimate, not only the absorption site, but also the MAE from the total energy difference of two self-consistent calculations corresponding to two different magnetization directions, in-plane and out-of-plane. This type of calculations requires extremely high precision (energy convergence threshold smaller than 10^{-6} eV) to get well converged MAE values. We achieve this convergence using Γ centered $5\times5\times1$, $7\times7\times1$ and $9\times9\times1$ k-point samplings.

DFT+SOC calculations confirm that Co adatoms prefer the hollow adsorption site rather than the atop N site. The energy difference between them is a slightly smaller than for spin-polarized DFT+U calculation, 316 meV, but it is still in the energy range of weak chemisorption.

The results of such accurate calculations are summarized in table 3.2, where we can see that the Co on both adsorption site has similar spin-moment. The quenching of orbital moments is overestimated by DFT calculations and results on an underestimation of the calculated MAE. This problem of DFT calculations is well-known, and therefore we can only reproduce observed trends.

The MAE for Co adatom on atop N site is significantly higher (1.5 meV) with an easy axis (EA) anisotropy (MAE > 0) in comparison with the hard axis (HA) anisotropy (MAE < 0) of Co adatom on hollow site (-0.43 meV).

Table 3.2: Summary of calculated spin-moment (m_S), orbital-moment (m_L) and zero-field splitting (ZFS) of Co atoms on a h-BN layer obtained from DFT calculations including the spin-orbit interaction. Here HA and EA stand for hard axis and easy axis, respectively.

Adsorption-site	m_S (μ_B)	m_L (μ_B)	ZFS (meV)
atop N	2.31	0.29	1.5 (EA)
hollow	2.20	0.184	0.43 (HA)

However, these values are not in quantitative agreement with XMCD data, see section 4.1.3, as a consequence of the overestimation of the quenching of the orbital-moment of this type of calculations. This inherent limitation of DFT makes us to follow a different procedure, which was proposed by Ferron *et al.*[30, 29], in order to get a more realistic MAE.

3.2.4 MLWFs and multiplet calculations

In order to calculate the low energy excitation spectrum of Co adatoms on h-BN we use a multiorbital Hubbard model, which was explained in section 2.3. Consequently, our aim is to build a many-body Hamiltonian derived from DFT calculations that accounts for the strong correlations in the system.

All the terms that are included in the model are analytical, except the crystal field term, which depends on the system. Therefore, the first thing to do is to derive an effective crystal field term from DFT.

The starting point are the non-spin-polarized DFT calculations on the 3×3 supercell for both adsorption sites using the VASP code. We change the basis from the plane wave basis, which was obtained from the VASP calculations, to Maximally Localized Wannier Functions (MLWF) using Wannier90 code[47]. We select an atomic orbital basis containing sp_2 and p_z orbitals for N atoms and s and d orbitals for Co atom to perform the basis change. In order to perform the change, we disentangle the bands in the energy range between -21.5 eV and 1 eV, referred to the Fermi energy, while energy bands between -12 eV and 0.8 eV are frozen.

Due to the gauge freedom inherent to MLWFs, it is necessary to check that we are describing the system correctly in the new basis. The first check is to compare the eigenvalues obtained from the previous DFT calculation and the MLWFs calculation, which can be done comparing the bandstructure obtained from DFT and MLWFs calculation, see fig. 3.6. The bandstructures showed in the figure present a very good agreement between DFT and MLWFs eigenvalues for both adsorption sites.

Apart from the eigenvalues, it must be checked the spread of the orbitals, as they might spread to another atoms in the unit cell. We have to check specially d orbitals from Co, as we shall assume later that they correspond to atomic orbitals.

Looking at the shape of the orbitals from Co, see fig. 3.7, one can notice that the s orbital has a mushroom shape, which indicates that the s orbital is hybridized with the p_z orbital of the N atom below. Furthermore, the d_{z^2} orbital is also distorted due to the hybridization with p_z orbitals of B and N atoms below. The rest of the orbitals are also slightly tilted, but their shape is close to the atomic ones. Additionally, the spread of the orbitals is not

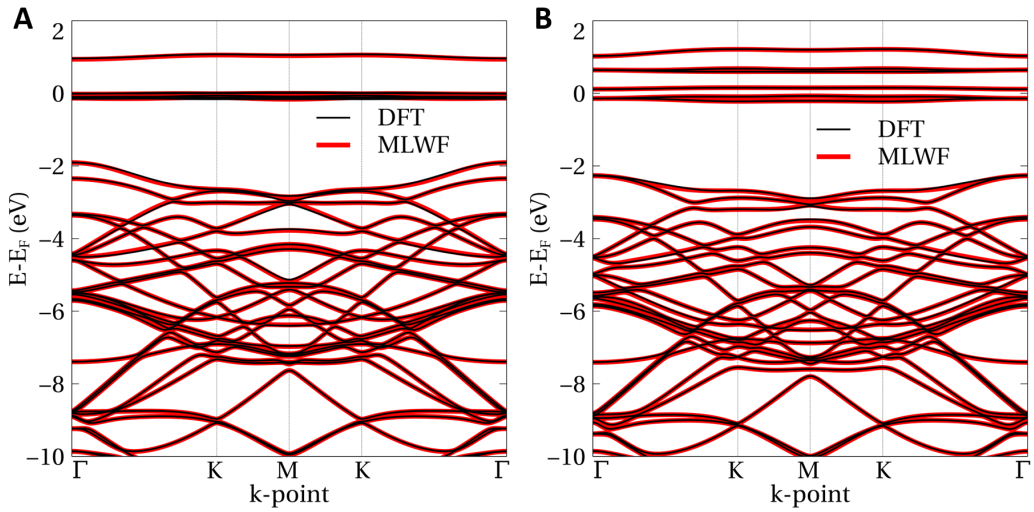

Figure 3.6: Bandstructures of Co on a 3×3 monolayer of h-BN obtained from DFT and MLWF calculations. Black lines represent DFT bandstructure and red ones MLWF. Left panel (A) shows the bandstructures for atop N adsorption site and right panel (B) for hollow site.

high, so we can use this orbitals to construct the crystal field term.

After all these checks, we can follow the procedure described in section 2.2.4 to reduce the dimension from a 42×42 matrix obtained in the MLWFs calcualtion to a matrix easier to handle within the multiorbital Hubbard model. In the case of atop N site, we used $\Delta_d = 0.05$, $\Delta_k = 0.01$ and $\lambda = -1.5$ eV to reduce the dimension of the matrix to 10×10. For the hollow site, the parameters that we used were $\Delta_d = 0.05$, $\Delta_k = 0.008$ and $\lambda = -1.5$ eV, and we obtain a 9×9 matrix.

According to spin-polarized DFT calculations, the d-shell of Co is partially filled with almost 8 electrons, see table 3.1. Therefore, we describe the interacting $N_e = 8$ electrons at the Co d-shell by the Hamiltonian in eq. (2.70). The single particle spin-orbit coupling constant is taken as the atomic value $\xi_{Co} = 65.5$ meV[89].

Following Hund rules, the expected total angular momentum and spin quantum numbers for the ground state of a d^8 configuration are $L = 3$ and $S = 1$, respectively. The crystal field splits the ground state multiplet, with degeneracy $(2L + 1)(2S + 1) = 21$, in a similar way on the two sites: the ground state multiplet is a spin triplet. However, as it is shown in fig. 3.8, the effect of the spin-orbit coupling is different. For the atop N site, the triplet ground state is split into a ground state doublet, with $|L_z|$ and $|S_z|$ degeneracy, and a singlet, with $|L_z| = |S_z| = 0$ and higher in energy. For

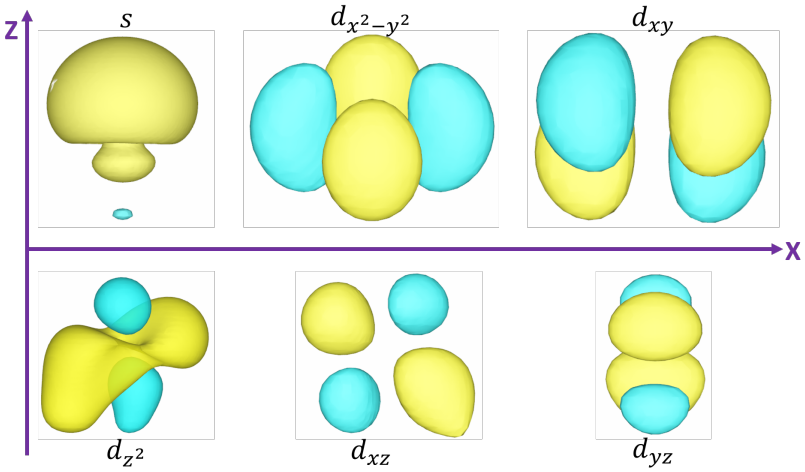

Figure 3.7: Visualization of MLWFs from Co adatom on atop N site with s and d character. Yellow lobes refers to positive values of the isosurface and blue to negative ones.

the hollow site, the splitting is much smaller than for the atop site due to the mixing of different components of $\langle L_z \rangle$ and $\langle S_z \rangle$. This mixing of states is reflected in the fact that, even for large magnetic fields, the values of $\langle L_z \rangle$ and $\langle S_z \rangle$ are not saturated.

3.2.5 Point charge model

As a consequence of the limitations induced by the use of MLWFs, see **??**, we disregard the procedure using MLWFs to construct the crystal field term and use a point charge model, which is derived from spin-polarized DFT calculations. Although it is well known that these point charge models do not provide a good quantitative description, especially when covalent bonds are present, they yield the right qualitative behaviour and they correctly reproduce the symmetry of the environment.

We include only first neighbouring N and B atoms in the point-charge model. The positions and charges that we use for each site are summarized in table 3.3. The atomic-cloud dependent expectation values $\langle r^2 \rangle$ and $\langle r^4 \rangle$ are taken from the atomic values[89].

The results of the multiplet calculation with the point charge model for Co on pristine h-BN on atop N (left panels) and hollow (right panels) adsorption sites are shown in fig. 3.9. As expected for an atomic d^8 configuration on the basis of Hund rules, the total angular momentum and spin quantum numbers are $L = 3$ and $S = 1$ in both cases. The crystal field splits the ground state

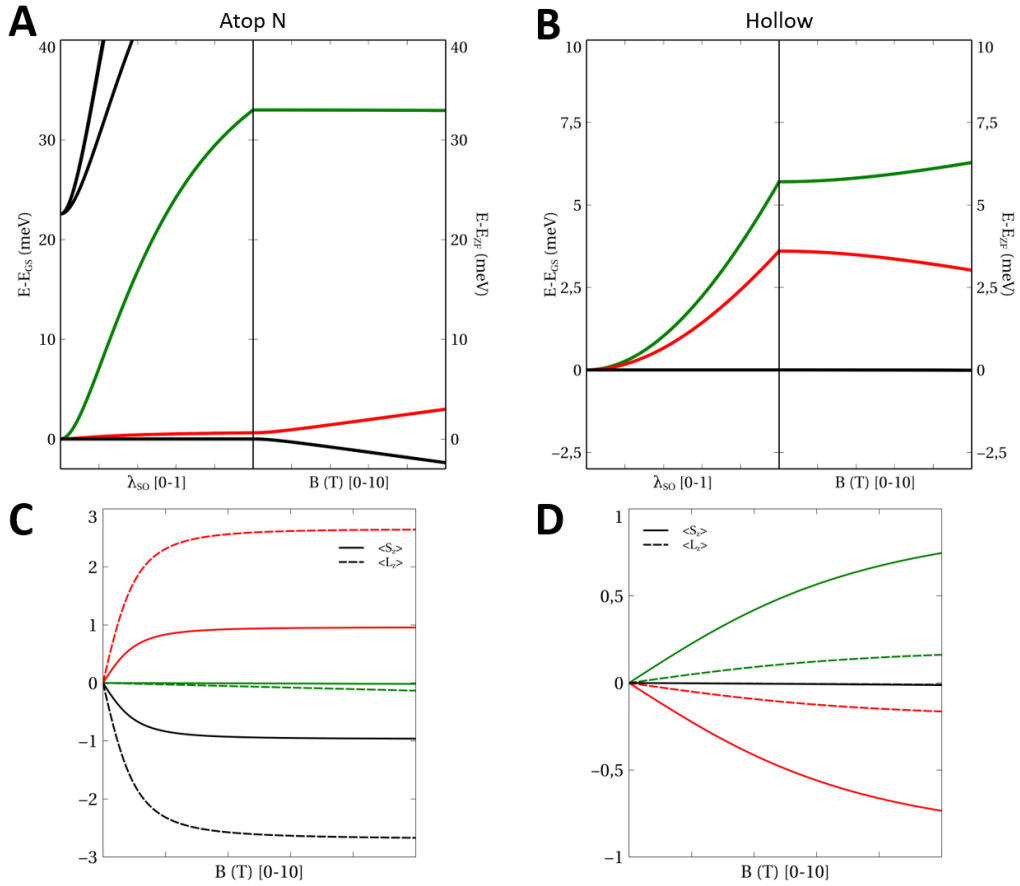

Figure 3.8: Results obtained from multiplet calculations when the crystal field is derived from MLWFs. Top panels, (A) and (B), show multiplet low energy excitation spectra of Co on a 3×3 h-BN monolayer in d^8-electronic configuration versus spin-orbit coupling strength (λ_{SO}) and magnetic field applied perpendicular to the h-BN plane. Bottom panels, (C) and (D), show the expectation values $\langle S_z \rangle$ (solid lines) and $\langle L_z \rangle$ (dashed lines) for the three lower energy states corresponding to the effective $S = 1$ anisotropic spin. Black color is used for the ground state, red for first excited state and green for second excited state.

multiplet, with degeneracy $(2L + 1)(2S + 1) = 21$, in a different way on the two sites due to lower symmetry of the hollow site; for atop N site, the ground state multiplet is an orbital doublet 6 times degenerate as it corresponds to $S = 1$, while for the hollow site the crystal field leads to a 3 times degenerate orbital singlet. As a result, the spin-orbit coupling induces a qualitatively different behaviour in both systems. More specifically, the effect of spin-

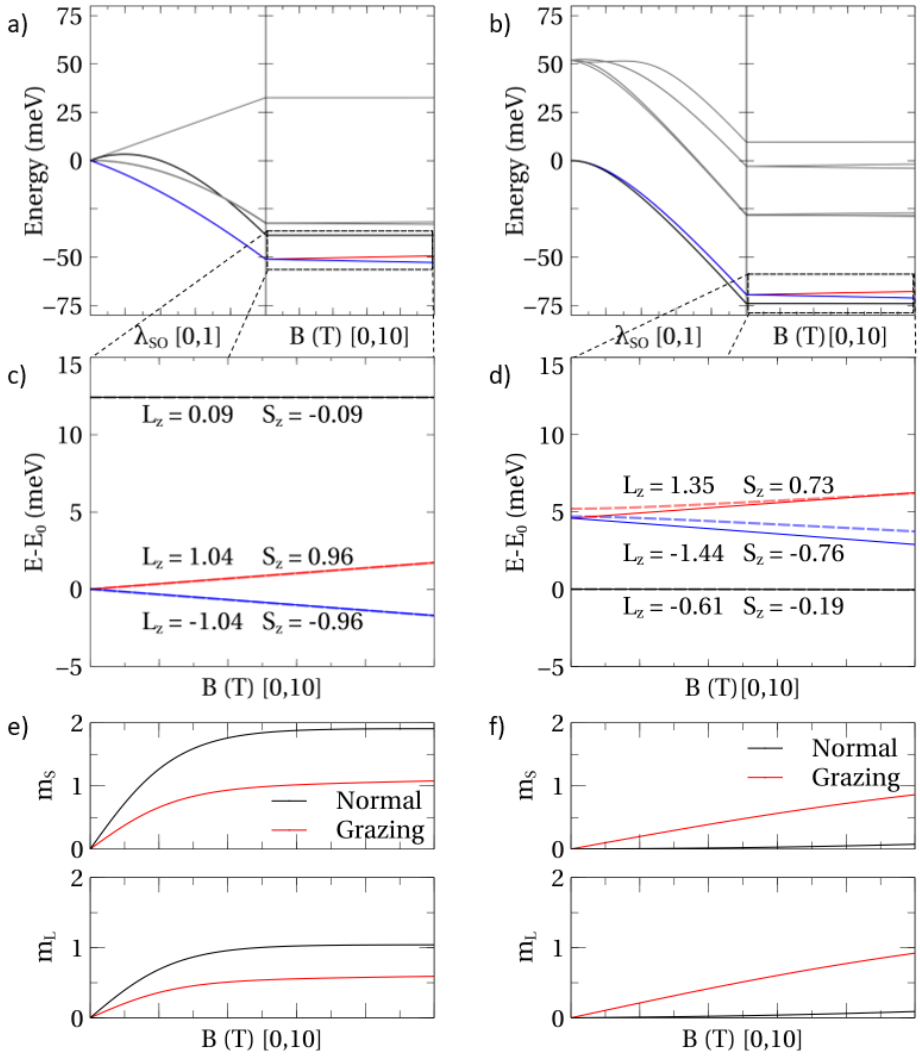

Figure 3.9: (a) and (b) Multiplet energy spectra versus spin-orbit coupling strength λ_{SO} and magnetic field along the out-of-plane direction for Co adsorbed on atop N and hollow sites of h-BN, respectively. The solid blue, red and black curves correspond to the lowest three energy states, while the light grey lines correspond to the higher energy states (not considered in the discussion). (c) and (d) Zooms of the low energy sector for the three lower energy states corresponding to the effective $S = 1$ anisotropic spin, where the labels correspond to the spin S_z and orbital L_z moments at $B = 6.8$ T. The superposed dashed lines correspond to the solutions of the spin Hamiltonian, eq. (3.1). (e) and (f) Average spin m_S (top) and orbital m_L (bottom) angular momenta in the direction of the applied B field for out-of-plane and grazing directions at $T = 2.5$ K.

Table 3.3: Position and charges of the point charges used to calculate the crystal field contribution in the multiorbital Hubbard model.

Hollow site				Atom	Atop N site			
x (Å)	y (Å)	z (Å)	q (e)		x (Å)	y (Å)	z (Å)	q (e)
1.23	0.71	−1.66	−0.50	N	0.00	0.00	−1.90	−1.50
0.00	−1.42	−1.66	−0.50	N	–	–	–	–
−1.23	0.71	−1.66	−0.50	N	–	–	–	–
0.00	1.42	−1.68	0.50	B	1.51	0.00	−1.90	0.50
1.23	−0.71	−1.68	0.50	B	−0.75	1.30	−1.90	0.50
−1.23	−0.71	−1.68	0.50	B	−0.75	−1.30	−1.90	0.50

orbit coupling on these two lowest laying multiplet states is to split the orbital doublet and singlet states into four and two states, respectively, see fig. 3.9(a) and (b). These states are further split by the external magnetic field.

As observed from the magnetic field dependence for the atop N position, the lowest doublet is formed by the $S_z = \pm 1$ states, while the excited state corresponds to $S_z \approx 0$, indicating an out-of-plane easy axis system. This situation is reversed for the hollow adsorption site, where an out-of-plane hard axis is found. The change in the preferential magnetization axis between the two adsorption sites is also corroborated by the average magnetization along the applied magnetic field, see fig. 3.9(c) and (d). Interestingly, the orbital moment is drastically affected by the adsorption site: the atop N site leads to a significantly larger orbital moment, a situation reported before in similar systems with very high symmetry[7, 90]. The origin of this unquenched orbital moment is the large and almost perfectly axial crystal field crated by the underlying N atom. On the contrary, the hollow site corresponds to a much lower point symmetry, in which both the spin and orbital components along the field direction are quenched compared to the atop N site.

Spin Hamiltonian Extracted from the multiorbital model

Excitation spectra of diluted magnetic centres in a paramagnet are often described in terms of spin Hamiltonians[89], which depend only on the spin degrees of freedom. In the case of $S = 1$ system, the spin Hamiltonian can be written as

$$H_S = D\hat{S}^2_{z'} + E\left(\hat{S}^2_{x'} - \hat{S}^2_{y'}\right) + g\mu_B\vec{B}\cdot\vec{S}, \tag{3.1}$$

where $\hat{S}_a$ is the a-component of the spin operator and D and E are the axial and transverse magnetic anisotropy parameters ($|D|$ = ZFS for a spin

Table 3.4: Parameters of the spin Hamiltonian H_S in eq. (3.1) as extracted from the multiorbital Hubbard model. Remember that for $S = 1$, ZFS $= |D|$.

Site	D (meV)	E (meV)	g_{xx}	g_{yy}	g_{zz}
Atop N	-12.41	0.008	1.72	1.67	2.96
Hollow	$+3.34$	0.50	3.15	3.01	2.15

$S = 1$). At finite external field $\vec{B}$, the spectrum changes due to the induced Zeeman splitting, with a response characterized by the Landé g-factor tensor. It should be pointed out that, although we may not expect the transverse term in eq. (3.1) from the C_{3v}-symmetry of the two adsorption sites, this term can appear due to any small symmetry breaking, which can be found for Co/h-BN/Rh(111)[19].

The parameters are usually estimated from fitting to experiments. Here, however we construct such a Hamiltonian from the many-body Hubbard Hamiltonian. If we denote by $|E_n\rangle$ and E_n the eigenvectors and eigenvalues of the many-body Hamiltonian, eq. (2.70), and taking advantage that $\left\langle E_n \left| \hat{S}^2 \right| E'_n \right\rangle \approx S(S+1)\delta_{nn'}$, we can construct H_S by projecting the $(2S+1)$ low energy states into the bases of eigenstate of $\hat{S}^2$, $\hat{S_{z'}}$, i.e., $H_S = \sum_{n=1,\dots,2S+1} E_n \hat{\mathcal{P}}_S |E_n\rangle \langle E_n| \hat{\mathcal{P}}_S$, where $\hat{\mathcal{P}}_S = \sum_{m_{z'}} |S, m_{z'}\rangle \langle S, m_{z'}|$. We notice that the quantization axis z' may be different from the z-axis taken in the DFT calculations, see inset fig. 3.5, in which case some rotations may be needed to recover the simple form eq. (3.1). The parameters found in the analysis are summarized in table 3.4. In agreement with previous results, the Co on atop N site can be described as an easy axis system with the z' direction out-of-plane. By contrast, the Co on hollow site corresponds to a hard axis. The energy spectra of H_S are also depicted in fig. 3.9 (a) and (b) with dashed lines. The accordance between these results and those of the multiorbital Hubbard model indicates the robustness of our assumptions in deriving H_S.

3.3 Conclusion

Summarizing, in this chapter we studied electronic properties of the free standing h-BN and magnetic properties of Co. We started determining the lattice constant of a free standing monolayer of h-BN, 2.51Å, which is in good agreement with previous experimental and theoretical works [85, 86]. This

lattice constant matches very well, less than 3 % , with a rotation of 13.9° of some fcc (111) or hcp (0001) surfaces, as the Ir(111) or Ru(0001) surfaces, that we will study in the next chapter.

Then, and using this lattice constant, we obtained the band-structure of free standing h-BN monolayer. As expected, and in agreement with other works [87], we obtain a band gap energy of 4.66 eV. This energy gap will prevent hybridizations near the Fermi energy of the adsorbate with the surface below, which is a very interesting property to use as a decoupling layer and stabilize a single atom magnetic moment on a surface[6, 7, 8, 13, 14, 15, 16, 17, 18, 19, 91].

We analysed the adsorption of Co. We performed different type of calculations to determine the adsorption site, but they do not provide conclusive results. The main reason for these is that both adsorption sites are close in energy, in chemisorption regime, that Van der Waals are playing an important role. So we decided to study magnetic properties of Co on both adsorption sites with different methods. However, it was convenient to know how electrons are divided in different shell of Co on both sites. Thus we obtained the PDOS from the spin polarized calculation and integrating this curves onto different states up to the Fermi level we saw that the occupation of both sites is the same. The main result of these calculations is that the Co has 7.8 d-electrons, which corresponds to a spin $S = 1$.

The first method consist in performing DFT calculations including spin-orbit interaction. These calculation yield a significantly higher out-of-plane easy axis magnetic anisotropy for the atop N site, while the hollow site has smaller MAE with an in-plane anisotropy. Both adsorption sites have similar spin moments, but orbital moments are too small, which is caused by the well known overestimation of the quenching of the orbital moment by DFT calculations. This overestimation of the orbital quenching produces an underestimation of the calculated MAE values by this method.

The second method consisted in constructing a many-body Hamiltonian using MLWFs to obtain the crystal field, which were obtained from a non-spin-polarized DFT calculation. In this way, we performed non-spin-polarized DFT calculations on the 3×3. Then, we changed the basis to MLWFs to construct the crystal fields and introduce these crystal fields in the many-body Hamiltonian. We also did the same for the 4×4 supercell, see appendix A. The results obtained by this method were not reliable as for both supercells we obtained completely different magnetic anisotropy. For the 3×3, we get an out-of-plane easy axis anisotropy with a ZFS of more than 30 meV for the atop N site and an in-plane anisotropy of 3 meV. This results agree quite well with DFT+SOC calculations as the obtained directions of the anisotropy are the same, but the MAE is one order of magnitude

higher.

The third method consisted in using a point charge model derived from DFT calculations to construct the crystal field, instead of using the MLWFs. For this, we extracted the position and charges of Co and first neighbouring N and B atoms and constructed the crystal field with them. Then, we introduced this crystal field in our many-body Hamiltonian. This approach yielded the results in fig. 3.9, where it is showed that the atop N site has a higher out-of-plane anisotropy, while the hollow site has a smaller in-plane one due to the smaller point symmetry, which quenches the spin and orbital components along the field direction. We confirmed these results by extracting a spin Hamiltonian and fitting the parameters.

Generally speaking, we found a qualitatively good agreement between the three methods. The MAE value is an order of magnitude larger for the atop N site than for the hollow site with all methods. Additionally, we obtain an out-of-plane easy axis anisotropy for the atop N site, while the hollow site corresponds to a hard axis.

In the next chapter, we will study the effect that Ir(111) and Ru(0001) surfaces have on the h-BN and when we deposit Co on it and we will compare our results with XAS, XMCD and XMLD experiments.

Chapter 4

Co ADATOM ON h-BN/Ir(111) AND h-BN/Ru(0001) SUBSTRATES

In the previous chapter we studied the electronic and magnetic properties of Co on free standing h-BN monolayer. However, in experiments, these systems are grown on different substrates. There are many substrates where h-BN monolayer can grow forming different structures[80]: from noble metal surfaces, as Au(111)[92] or Ag(111)[93], to transition metal ones, like Mo(110)[94] or Re(0001)[95]. We will focus the attention on Ir(111) and Ru(0001) substrates for which we have available experimental results for Co on h-BN/Ir(111) and on h-BN/Ru(0001). The growth by chemical vapor deposition of h-BN using borazine on these two substrates leads to two different properties. The Ir(111) substrate results in a structure with a much lower corrugation[96] than Ru(0001)[97].

On one hand, the X-ray absorption spectroscopy (XAS), combined with multiplet calculations using CTM4XAS6[98] and the multiX[99] codes, provides a clue about the electronic structure of adatoms. On the other hand, the magnetic ground state and magnetic anisotropy are obtained by measuring X-ray magnetic circular dichroism (XMCD) and X-ray magnetic linear dichroism (XMLD) spectra at normal and grazing incidences, and combined with multiplet calculations with multiX[99] code.

Therefore, the first part of the chapter will be devoted to the analysis of these experimental data. Later, we will study the absorption of Co adatoms on the 4×4 h-BN monolayer on a 4 layer slab of Ir(111) and Ru(0001) by DFT calculations. Notice that including the metallic slabs add a large amount of atoms to the unit cell, which makes calculations computationally more expensive. Our main goal with these DFT calculations is to give

additional support to the fundamental difference between Co adsorption on h-BN/Ru(0001) and h-BN/Ir(111), i. e., the adsorption site, which is atop N and hollow site, respectively. Actually, this basic assumption has been used in the previous chapter to study the MAE at three different levels of approximation. As it is shown in the chapter, the multiorbital Hubbard model results for the spin (S), S_z, L_z and MAE values previously obtained are in very reasonable agreement with the values extracted from fittings to XMCD data, as long as the different adsorption sites are considered.

4.1 XAS, XMCD and XMLD experiments

In this section, we will describe the experiments and multiplet calculations using CTM4XAS6 and multiX codes performed in the group of Prof. Harald Brune[100].

4.1.1 Sample Preparation

The Ir(111) and Ru(0001) single crystals were prepared *in-situ* by repeated cycles of Ar^+ sputtering and annealing. Subsequently, h-BN was grown by chemical vapor deposition (CVD) using borazine (125 Langmuir at 1030 K). The reaction is self-limited to one monolayer since the catalytic dissociation of the precursor molecule requires bare metal areas. Co was deposited from a high purity rod (99.998 %) using an e-beam evaporator in a background pressure of $\leq 3 \times 10^{-11} mbar$. The Co coverage is expressed in monolayers (ML), where 1 ML is defined as one Co atom per h-BN unit cell. During Co deposition the temperature of the sample surface remains below 5 K. At this temperature surface diffusion is inhibited, corresponding to a random adatom adsorption.

4.1.2 XAS data

The XAS experiment consists in exciting a core electron to an empty state by the absorption of an X-ray photon, which is obtained usually by synchroton radiation. During the X-ray absorption process, a core-hole is created in the excited electron state. XAS experiments can determine accurately the local geometry or obtain element-specific information[101]. In our case, we use XAS experiment to determine the electronic structure of Co, as the position of the peak depends on the number of $3d$ electrons.

The X-ray absorption measurements were performed at the EPFL/PSI X-Treme beamline at the Swiss Light Source, Paul Scherrer Institut, Villi-

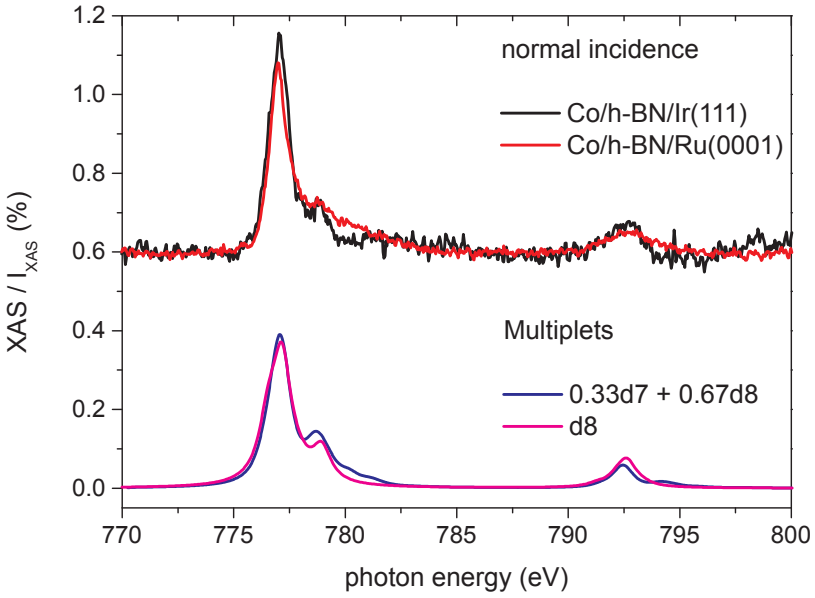

Figure 4.1: (top) XAS spectra measured for Co on h-BN/Ir(111) and on h-BN/Ru(0001) ($\theta = 0°$, $T = 2.5\ K$, $B = 6.8$ T, Co coverage $\Theta_{Co} = 0.005$ ML and $\Theta_{Co} = 0.008$ ML on h-BN/Ir(111) and on h-BN/Ru(0001), respectively). Similar spectral features are observed on the two substrates. (bottom) Multiplet calculations with two different codes, namely CTM4XAS6 and multiX for mixed and pure d-shell configuration, respectively. The electronic configuration of the Co atom is prevalently $3d^8$ corresponding to a spin quantum number of $S = 1$.

gen, Switzerland[102]. The experiments were carried out in the total electron yield (TEY) mode at 2.5 K, for circularly (σ^+, σ^-) and linearly (σ^h, σ^v) polarized X-rays, with the magnetic field applied parallel to the incident X-ray beam. The XAS corresponds to ($\sigma^+ + \sigma^-$). The TEY mode enables the high sensitivity required by the extremly low concentration ($\sim 1\%$) of magnetic elements at the surface. The XAS spectra were acquired with the magnetic field collinear with the photon beam at normal ($\theta = 0°$) and grazing incidence ($\theta = 60°$). To take into account the different surface areas illuminated by the X-ray beam at both sample orientations, the XAS spectra were normalized to the intensity at the pre-edge (772 eV). Prior to deposition of Co, background spectra on the given substrate have been recorded and then subtracted from the Co XAS spectra to eliminate the substrate contribution.

The comparison between the XAS spectra of isolated Co atoms deposited on the two surfaces and the spectra obtained from multiplet calculations with two different approaches is shown in fig. 4.1. The experimental data

show a fine multipeak structure, fingerprint of the Co electronic state. In particular we note that the L_3 edge splits in a main peak at 777.0 eV and in a small shoulder at 778.8 eV. This multipeak structure compared to the broad L_3 shape observed for Co atoms in bulk is signature of an electronic state partially preserving an atomic like-character. In order to disentangle the Co electronic state, multiplet calculations were performed using the CTM4XAS6[98] and the multiX[99] codes. In both cases, a crystal field (CF) with C_{3v} symmetry was assumed, corresponding to Co adsorption on top of the N atom or in the hollow site. The CTM4SAX6 code describes the CF via Dq, Ds and Dt terms and allows for mixed configurations; while the multiX code describes the CF via a point charge approach and it does not include partial charge transfer to the ligand, i.e., only pure $3d^n$ configurations are considered. Both calculations represent the data well and reveal a ground state configuration with mainly $3d^8$ character on both surfaces. This predisposition to acquire an extra electron in the $3d$ shell is frequently observed for Co atoms adsorbed on surfaces with low electron density at the Fermi level such as alkali metals[103], graphene[15, 16, 104] or MgO[7].

4.1.3 XMCD and XMLD data

The use of circularly or linearly polarized X-rays (XMCD and XMLD respectively) opened the door to study magnetic properties of transition metals or rare earth elements. These experiments compare the absorption spectra of two XAS measurements with two different polarizations.

More specifically, in XMCD experiments, as the angular momentum must be conserved, X-ray photons transfer their angular momentum to excited electrons, $\hbar$ for photons polarized to the right or $-\hbar$ to the left. The transferred angular momentum from right polarized photons is opposite to left polarized photons and, thus, the excited electrons have different spin, depending on the original photon polarization. Since the $p_{3/2}$ (L_3 edge) and $p_{1/2}$ (L_2 edge) states have opposites spin-orbit coupling, l+s and l-s, respectively, the spin polarization will be different at the two edges. After absorbing the X-ray, the electrons are excited to empty d-bands, which are also polarized, i.e., the number of unoccupied spin up states is different from the number of unoccupied spin down states. The transferred angular momentum is reflected as a change of ± 1 in the total angular momentum quantum number m_J and thus the excited electrons will behave differently for two different photon polarizations. The XMCD signal corresponds to $(\sigma^+ - \sigma^-)$. As antiferromagnetic materials have no net magnetization, the absorption of right polarized or left polarized X-rays is the same, and, thus the XMCD signal is null.

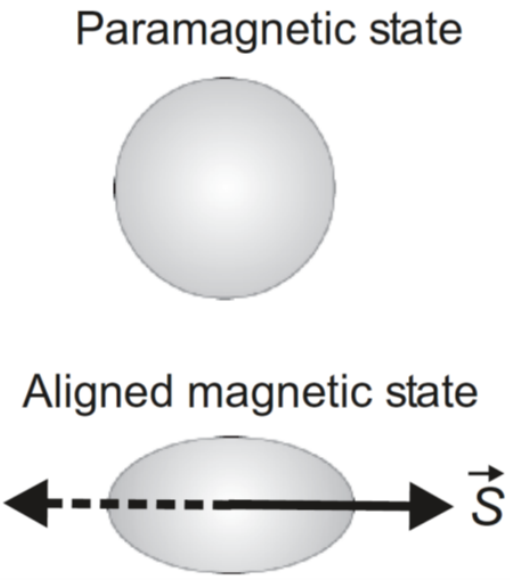

Figure 4.2: Illustration of how a spherical charge density may be modified in the presence of a magnetic alignment of the spins in the sample. The charge distortion arises from the spin-orbit coupling and an asymmetry is induced relative to the spin axis (not direction!). The effect exists in both collinear ferromagnets and antiferromagnets. Picture taken from the book of Stöhr and Siegmann[105].

In contrast, XMLD experiments provide information about the magnetism of both ferromagnetic or antiferromagnetic materials. Each magnetic atom has a spin moment, which induces a deformation of the charge due to spin-orbit coupling. Even if there is no net magnetic moment, as in antiferromagnets, this effect still occurs. The charge distortion depends on the spin axis, see fig. 4.2, but not on the direction. Thus, the absorption of X-rays polarized parallel to the spin axis is different from the absorption of X-rays polarized perpendicular. And this is where XMLD experiment comes in. It measures the difference in absorption of X-rays polarized parallel and perpendicular to the spin axis. Therefore, XMLD experiments reveal local charge anisotropies.

Comparing both experiments, XMCD depends linearly on the sample magnetization ($\vec{M}$), while XMLD varies with $\vec{M}^2$. This means that XMCD depends on the magnitude and the direction of the magnetization, while XMLD depends only on the magnitude, and not on the direction of individual magnetic moments. This feature of XMLD makes it useful to study antiferromagnets and other materials with compensated magnetic structures.

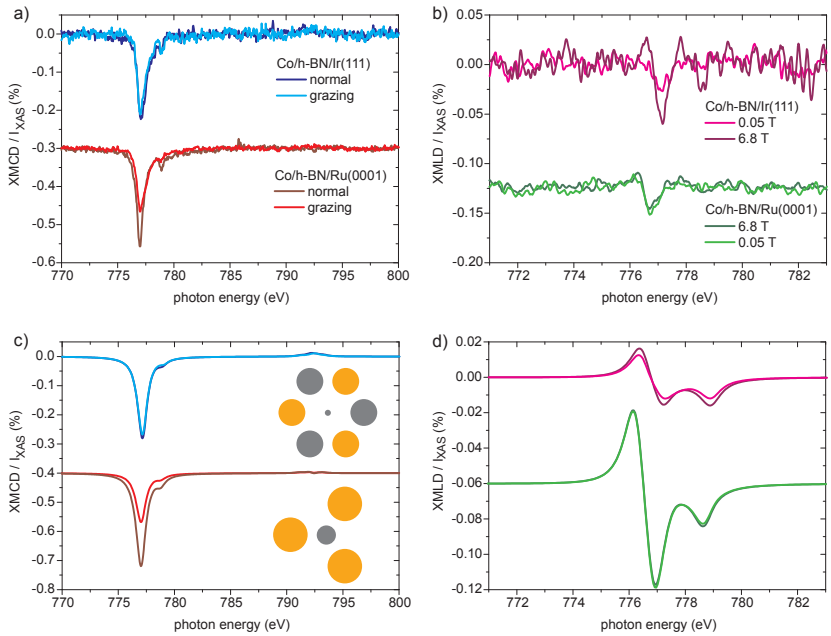

Figure 4.3: (a) XMCD spectra measured for Co on h-BN/Ir(111) and on h-BN/Ru(0001) at normal and grazing incidence in an external field $B = 6.8$ T. (b) XMLD spectra measured at grazing incidence for Co on h-BN/Ir(111) and on h-BN/Ru(0001) showing strong and weak field dependence, respectively. (c) XMCD and (d) XMLD spectra calculated with the multiX code by using the point charge distributions sketched in panel (c) for hollow and atop N Co adsorption sites. The area of the circles is proportional to the charge value, and the colour represents the sign of the charge (grey = positive, yellow = negative).

The microscopic origin of the magnetic anisotropy is the combined effect of the anisotropy in the atomic orbital moment dictated by the CF and the spin-orbit interaction[106, 107]. In solids, the orientation of the orbital moment is defined by the CF symmetry and strength. However, in an external magnetic field, $\vec{S}$ and $\vec{L}$ tend to align to the field itself; thus, the resulting configuration depends on the competition between CF and magnetic field. Linear dichroism is a measure of the charge density involved in perpendicular versus in-plane bonds formed between Co atom and supporting substrate. Its field dependence, i.e. the XMLD, thus provides a measure of this competition.

Coming back to our system, XMCD and XMLD spectra measured at normal ($\theta = 0°$) and grazing ($\theta = 60°$) incidence, see fig. 4.3, enlighten the magnetic properties of Co on h-BN/Ir(111) and on h-BN/Ru(0001). The quite

Table 4.1: Point charge CF scheme employed in multiplet calculations with the multiX code.

h-BN/Ir(111)					h-BN/Ru(0001)			
x (Å)	y (Å)	z (Å)	q (e)		x (Å)	y (Å)	z (Å)	q (e)
0	0	−1.70	0.10		0	0	−1.60	1.00
1.50	0	−1.70	−1.40		1.50	0	−1.60	−1.80
−0.75	1.30	−1.70	−1.40		−0.75	1.30	−1.60	−1.80
−0.75	−1.30	−1.70	−1.40		−0.75	−1.30	−1.60	−1.80
−1.50	0	−1.70	1.40		–	–	–	–
0.75	1.30	−1.70	1.40		–	–	–	–
0.75	−1.30	−1.70	1.40		–	–	–	–

Table 4.2: Orbital (m_L) and effective spin (m_{S+D}) moments (in μ_B), as well as their ratios, for normal (0°) and grazing (60°) incidence evaluated by applying the sum rules to the experimental (calculated) spectra assuming a hole number $n_h = 2$.

		m_{S+D}	m_L	m_L/m_{S+D}
Normal	h-BN/Ir(111)	1.4(2.01)	0.8(1.13)	0.57(0.56)
	h-BN/Ru(0001)	1.4(2.22)	1.0(1.42)	0.71(0.64)
Grazing	h-BN/Ir(111)	1.2(1.9)	0.7(1.10)	0.58(0.58)
	h-BN/Ru(0001)	1.0(1.25)	0.6(0.77)	0.6(0.62)

similar XMCD shape and intensity observed at normal and grazing incidence for Co on h-BN/Ir(111) indicate negligible magnetic anisotropy. On the contrary, in the case of Co on h-BN/Ru(0001) it is observed a strong angular dependence of the XMCD signal, larger at normal than at grazing incidence, indicating a strong out-of-plane magnetic anisotropy. These conclusions are also supported by the magnetic field dependent (independent) XMLD signal observed in Co/h-BN/Ir(111) (Co/h-BN/Ru(0001)). In systems with strong CF and magnetic anisotropy, the application of an external field can only marginally change the orientation of $\vec{L}$ and $\vec{S}$, resulting in a field independent XMLD as observed in Co/h-BN/Ru(0001); the opposite behaviour is observed in low magnetic anisotropy systems. The angular dependence of the magnetization curves shown in fig. 4.4 fully confirm the low and high magnetic anisotropy scenario for Co/h-BN/Ir(111) and Co/h-BN/Ru(0001), respectively.

Comparison of the experimental data with multiplet calculations, which

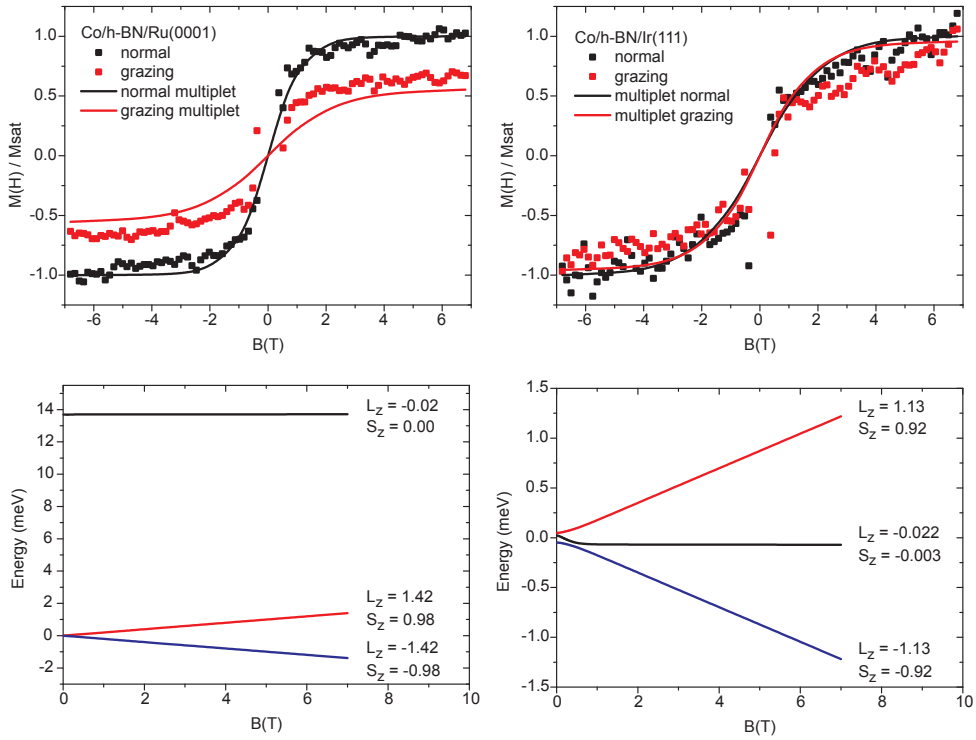

Figure 4.4: Upper panels: magnetization curves, (dot) experimentally acquired and (line) obtained from multiplet calculations, for Co on h-BN/Ru(0001) and h-BN/Ir(111) at both normal and grazing incidence. Lower panels: Corresponding field splitting of the Co lower states obtained from multiX multiplet calculations. The labels in lower panels L_z and S_z are the orbital and spin moments in the normal direction, respectively, measured in $\hbar$.

were performed with the multiX code, allows us to provide a more quantitative analysis. Given the mainly $3d^8$ character of the Co atoms on both substrates, we focused on calculations with the multiX code in which a pure $3d^8$ electronic state has been assumed. These calculations include the effect of the external magnetic field, finite temperature, incidence of X-rays and crystal field environment of the magnetic atom. The CF is defined by effective point charges whose positions and intensities were chosen in order to simultaneously fit the shape and intensity of XAS, XMCD and XMLD spectra as well as the shape of the magnetization curves at the two X-ray incidence angles. The point charge distributions that best reproduce the two systems are sketched in fig. 4.3, and the exact position and charge values are summarized in table 4.1. They correspond to a hollow and atop N adsorp-

tion site for Co/h-BN/Ir(111) and Co/h-BN/Ru(0001), respectively. This is very similar to the behaviour of Co on graphene on both substrates[16]. Orbital (m_L) and effective spin magnetic moment (m_{S+D}), given by the sum of the spin and dipolar term, projected onto the X-ray incidence direction are evaluated by applying the sum rules to the experimental and calculated spectra, see table 4.2. The orbital moment is relatively large on both samples with values close to free atom values observed for Co deposited on other decoupling layers such MgO[7] or graphene on Ru(0001)[16]. In addition, m_L shows a strong angular dependence for Co/h-BN/Ru(0001), with the largest value observed at normal incidence, while there is only a fractional reduction by moving from normal to grazing incidence for Co/h-BN/Ir(111). The different angular dependence of the orbital momentum observed in the two systems explains the high (negligible) magnetic anisotropy observed in Co/h-BN/Ru(0001) (Co/h-BN/Ir(111)), as also highlighted by the angular dependence of the magnetization curves in the two systems, see fig. 4.4. We can quantify the strength of the MAE by the zero field splitting (ZFS), which is the energy difference between the ground and first excited state. The ZFS values, as deduced from the multiX calculations, are shown in table 4.3. For Co/h-BN/Ru(0001) we find that the ground state consists of a doublet ($S_z = 0.98$, $L_z = 1.42$) separated by 13.7 meV from the singlet ($S_z = 0$, $L_z = 0.02$). These values of S_z and L_z for different states are in very good agreement for the ground state doublet ($S_z = 0.96$, $L_z = 1.04$) and singlet excited state ($S_z = 0.09$, $L_z = 0.09$) obtained from the multiorbital Hubbard model for atop N site within the point charge approach, see fig. 3.9. The ZFS of 13.7 meV obtained for Co/h-BN/Ru(0001) is quite large, similar to the values observed for Co on graphene supported by different metallic substrates[15, 16], and only lower than the ZFS of about 58 meV reported for Co/MgO/Ag(100)[7]. Furthermore, the $D = -12.41$ meV value resulting from the spin Hamiltonian analysis for atop N site agrees very well with experimental observations of Co on h-BN/Ru(0001). On the contrary, for Co/h-BN/Ir(111) we find a singlet ground state ($S_z = 0.003$, $L_z = 0.022$) and a excited doublet ($|S_z| = 0.92$, $|L_z| = 1.13$) only 70 μ eV higher in energy. The agreement with the hollow site on free standing h-BN is more limited, as the experiment does not detect a measurable MAE. The multiorbital Hubbard model results for the hollow site are a ground state singlet ($S_z = 0.19$, $L_z = 0.61$) and a doublet excited state ($S_z = 0.76$, $L_z = 1.44$). Additionally, the $D = 3.34$ meV value obtained from the comparison with the spin Hamiltonian is in clear contrast with the almost null XMCD signal. We note that on both surfaces the lowest energy states are not pure $S_z = 0$, ± 1 and L_z states, since they contain admixtures of different spins and orbital moments from electronic levels belonging to multiplets higher in energy.

Table 4.3: Values of the spin and ZFS as deduced from multiplet calculations as obtained with the multiX code assuming a $3d^8$ configuration.

	S	ZFS(meV)
h-BN/Ir(111)	0.92	0.07
h-BN/Ru(0001)	0.98	13.7

In order to compare experimental results with the multiorbital Hubbard model, there are two important points that have to be taken into account. The underlying metallic substrate, Ir(111) or Ru(0001), partially reduces the symmetry of Co environment. In addition, the crystal field felt by Co atoms can be affected by the region of the Moiré pattern where it is adsorbed. In the case of the atop N site, the crystal field is created mainly by the underlying N atom, so a corrugation of the h-BN monolayer does not produce qualitative changes. Assuming that, in the experiment, the N-Ru registry is the same, there are small changes of the MAE between different Co atoms on h-BN/Ru(0001). Contrarily, on the hollow site, the electrostatic potential on the Co position tends to cancel, due to the symmetric positions of opposite charges with similar magnitudes of the first neighbours atoms. Thus, a small corrugation, charge transfer or lattice strain can introduce important changes for atoms adsorbed on hollow sites. This, partially explains the limited agreement for Co atoms on the hollow sites on h-BN/Ir(111).

4.2 Modelling h-BN on Ir(111) and Ru(0001) surfaces

In order to model the experimental systems, Co/h-BN/Ir(111) and Co/h-BN/Ru(0001), we will start studying how the h-BN behaves when it is physisorbed on these surfaces. The calculations have been done using a 4×4 h-BN supercell, which matches reasonably well, with a rotation of 13.9°, on the Ir(111) and Ru(0001) surfaces. This strategy is similar to the one used to study the adsorption energy variations in different Moiré domains for h-BN/Ni(111) with a lattice matched model[88]. Previous works showed that the corrugation of h-BN is much smaller in the case of Ir(111)[96] than the case of Ru(0001)[97]. For this reason we will study first the case of the Ir(111) surface.

4.2.1 Absorption of h-BN on Ir(111) surface

We performed non-spin-polarized DFT self consistent calculations varying the adsorption distance of flat h-BN from 2.7 Å to 3.9 Å in steps of 0.05 Å. We used a gaussian smearing with a width of 0.05 eV and a $9 \times 9 \times 1\Gamma$-centered k-point mesh. We set an energy cutoff of 600 eV. As the h-BN is in the physisorption regime, where Van der Waals forces play an essential role, we include Van der Waals corrections by the D2 method of Grimme[58].

Comparing the energies obtained from different calculations performed with the same parameters gives a very good clue about the adsorption distance. In this way, we can conclude that the optimal distance from the flat h-BN monolayer to Ir(111) is around 3.10 Å. A relaxation was performed, from this point, until vertical forces acting on B and N atoms were smaller than 0.05 eV/Å. For the relaxation, we used the same set of parameters as before. The h-BN structure obtained from the relaxation shows a small corrugation of 0.44 Å, see fig. 4.5. This corrugation is slightly higher than in the work of Schulz *et. al.*[96]. The reason for this difference is that they use a supercell consisting on a 13×13 superstructure of h-BN on a 12×12 Ir(111) slab. This different approach introduce, in our case, a bigger lattice mismatch, 2.4 % for our supercell, against the 0.8 % of the case of Schulz *et. al.*, and explains our higher corrugation.

It is worth to mention that the closest region to the surface is 2.79 Å above it, which is still in the physisorption regime. Therefore, we expect that the adatoms behave similarly to the case of free standing h-BN studied in the previous chapter.

4.2.2 Absorption of h-BN on Ru(0001) surface

As both surfaces have the same lattice parameter, we used the same rotated supercell as for the Ir(111). In this case, we place it 3 Å above the Ru(0001) surface and perform a non-spin-polarized relaxation including the the Van der Waals correction by the DFT-D2 method of Grimme. We use 0.2 eV width gaussian smearing, an energy cutoff of 400 eV and Γ only k-point sampling. We allow atoms from the h-BN to move in the perpendicular direction until forces were smaller than 0.01eV/Å.

The relaxation results in a much more corrugated structure for Ru(0001) surface, see fig. 4.6, than for Ir(111). This corrugation is in good agreement with the measurements of Goriachko *et. al.*[97], who measures a corrugation of about 0.7 Å. As in the case of h-BN on Ir(111), the used 4×4 h-BN superstructure on rotated Ru(0001) surface is smaller than the 13×13 h-BN superstructure on the 12×12 Ru(0001) slab, due to some compressive strain

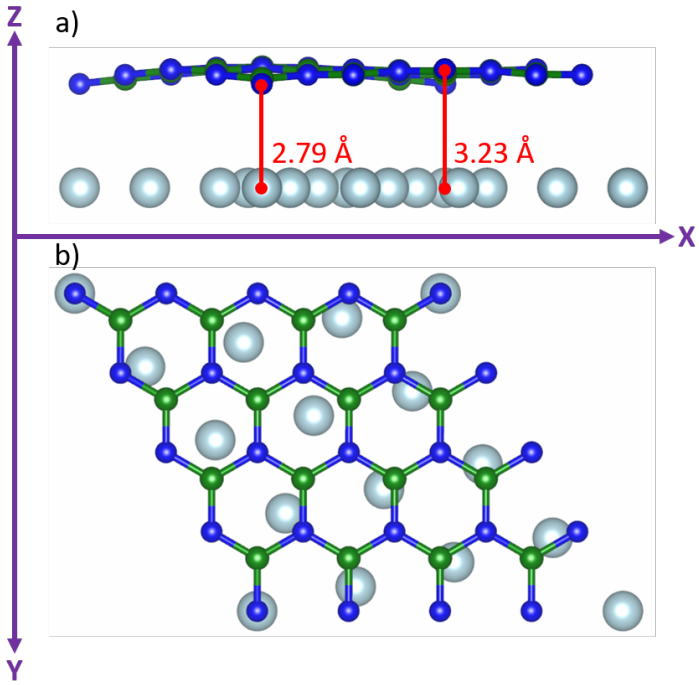

Figure 4.5: a) Side and b) top views of the 4 × 4 supercell for h-BN on Ir(111) surface, after relaxation of the h-BN monolayer in the Z direction. Green and blue spheres represent B and N atoms, respectively, while light blue are the top most layer Ir(111) surface atoms. The side view, a), show a small corrugation of the h-BN on Ir(111) of 0.44 Å.

that increases the corrugation.

There are two qualitatively different regions of h-BN on Ru(0001): the first region is the one that is far from the surface, and the second one close to the surface. We expect the behaviour of adatoms on these different regions to be different. On one side, in the far region, the adatoms will behave similarly to the free standing h-BN, as the interaction of the h-BN with surface atoms is weak. On the other side, in the close region, and despite the insulating character of the h-BN, the Ru surface electrons will interact with the adatoms, affecting the adsorption.

4.3 Co adatom on h-BN/Ru(0001)

In this section we will study the effect of Ru(0001) surface on the adsorption of Co adatom. The highly corrugated h-BN/Ru(0001) may change the

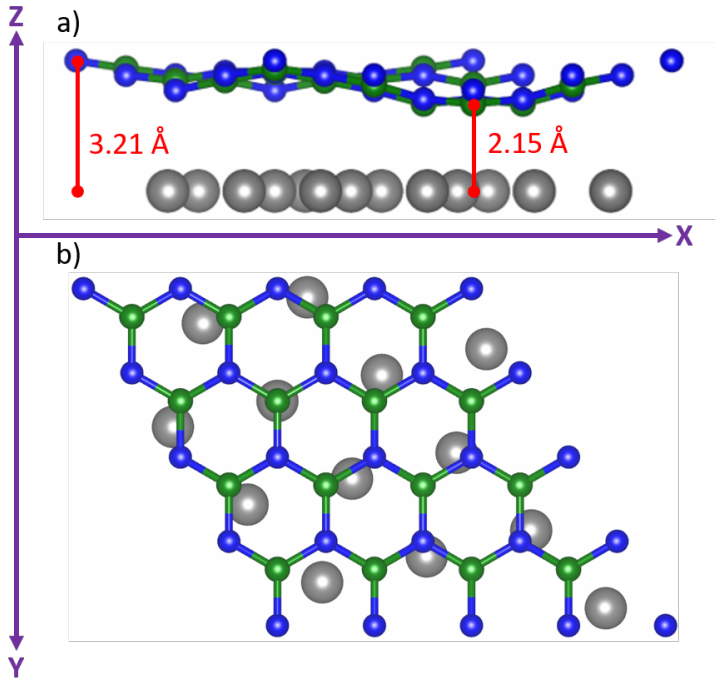

Figure 4.6: a) Side and b) top views of the 4×4 supercell for h-BN on the Ru(0001) surface after relaxation of the h-BN monolayer in the Z direction. Green spheres represent B atoms, blue ones N atoms and grey ones the top most layer Ru(0001) surface atoms. The side view show a) shows the high corrugation of the h-BN on Ru(0001) of 1.06 Å.

adsorption site of Co, specially in the region where the h-BN is closer to Ru(0001). We used the relaxed h-BN/Ru(0001) obtained in the previous section and we placed the Co atoms at three different regions, depending on the distance between the h-BN monolayer and the Ru(0001) surface: 3.2 Å, 2.5 Å and 2.1 Å, which we will call far, medium and close regions, respectively. With this strategy, we simulate the absorption of Co on different Moiré domains.

We performed spin-polarized DFT+U relaxations using an energy cutoff of 400 eV, a gaussian smearing of 0.2 eV width and Γ only k-point sampling. We included Van der Waals correction by using the DFT-D2 method of Grimme. We set the Coloumb (U) and exchange (J) parameters at 4 and 0 eV, respectively.

In the case of atop N adsorption site, we relaxed the perpendicular coordinates of Co adatom and the N atom below and all the coordinates of first neighbour B atoms until the forces were smaller than 0.01 eV/Å. For

Table 4.4: Relative energies of Co on h-BN/Ru(0001) for both adsorption sites obtained from spin-polarized DFT+U calculations. The lowest energy was taken as the reference, the one that corresponds to 0 meV.

Region	Site	Energy (meV)
Far	Hollow	0
	Atop N	821
Medium	Hollow	48
	Atop N	83
Close	Hollow	18
	Atop N	0.3

the hollow case, we performed the same relaxation as the atop N, relaxing all coordinates of first neighbour N and B atoms.

The relative energies of these calculations are summarized on table 4.4. When the Co is adsorbed on the far region of h-BN/Ru(0001), it has a similar behaviour that the free standing h-BN. DFT+U calculations show that the hollow site is favourable in this region. As it was expected, these results show that at 3.2 Å the interaction between the h-BN monolayer and the Ru(0001) surface is too weak to affect the adsorption of Co. However, when we look to what happens in the close region, the Co atom prefers to be on the atop N site.

Notice that atop N site on the close region is only 0.3 meV above the hollow site on the far region. This energy difference is too small to argue in favour of one adsorption site or the other only with these total energy calculations. Furthermore, our 4×4 supercell is too small to contain all possible Ru registries for the atop N site on the close region, nor for the hollow site for far region. A similar situation was found for molecular adsorption on metal weak chemisorption regime, like Co on Cu(111), where the correct adsorption site is only obtained when hybrid functionals, like, BLYP, are used[108]. However, combining XMLD and XMCD data in section 4.1.3 with the multiorbital Hubbard model, see section 3.2, we deduce the atop N site for Co on h-BN/Ru(0001).

4.4 Conclusions

In this chapter we studied the adsorption of Co adatoms on two different surfaces: the almost flat h-BN/Ir(111) surface and the highly corrugated h-BN/Ru(0001). We started analysing experimental data, where XAS, XMLD

and XMCD reveal a large out-of-plane magnetic anisotropy for Co individual atoms adsorbed on h-BN/Ru(0001), but basically without any anisotropy on h-BN/Ir(111). The XAS data also reveal the spin quantum number $S = 1$ for Co on both surfaces, which is in good agreement with spin-polarized DFT calculations obtained for free standing h-BN in the previous chapter. In addition, the adsorption sites for Co on h-BN/Ru(0001) and on h-BN/Ir(111) are identified as atop N and hollow sites, respectively, by fitting XMCD data with CTM4XAS6 and multiX codes for multiplets calculations.

The agreement is rather good between the experimental S, S_z, L_z and ZFS values for the Co on h-BN/Ru(0001) and the multiorbital Hubbard model values for atop N adsorption site for Co on the free standing h-BN. The obtained average spin and orbital moments saturate for fields around 3 T in both, experiments and model. Additionally, the obtained ratios (m_L/m_S) of 0.71 and 0.6 in the experiments at normal and grazing incidence are close to the value of 0.54 obtained in the model. In contrast, the XMCD data for Co on h-BN/Ir(111) give a magnetic anisotropy much smaller than the one obtained with the model for the Co on the h-BN hollow site. The difference in the agreement is partially explained by the absence of a strong crystal field in the case of the hollow site, making this site more sensitive to small changes, like corrugation, charge transfer or lattice strain. In the case of atop N site, the strong crystal field affecting the Co is mainly produced by the underlying N atom. This strong crystal field is not affected by changes in the surrounding atoms and, thus, gives better agreement between the experiments and the model.

For the adsorption site calculations on different substrates, we needed an accurate description of the surfaces. For that we used a rotated lattice matched model. This model consist in a 4×4 h-BN surface unit cell on a rotated Ir(111) or Ru(0001) 4 layer slab. This model slightly magnifies the corrugation of h-BN on both surfaces, but gives the appropriate behaviour at much lower computational cost. The main reason for this is that the calculated Moiré pattern of h-BN on both metallic substrate requires supercells of 13×13 h-BN surface unit cell to represent it. Despite the magnification of the corrugation of the h-BN, on Ir(111) surface it is still small, due to the low reactivity of this surface. For this reason, the Co on h-BN/Ir(111) substrate is assume to adsorb on a hollow site, as it did in the free standing h-BN, validating our previous considerations.

In contrast to the Ir(111) surface, the Ru(0001) induces a high corrugation on the h-BN. This high corrugation of the h-BN affects the adsorption of the Co. So, the situation is more complex in this case. The h-BN on Ru(0001) has some regions that are much closer than other regions from the surface. According to XAS data the Co retains the spin $S = 1$. Looking at DFT+U

calculations, table 4.4 shows that the total energy difference between the Co adsorbed on atop N close to the h-BN and on hollow site far to the h-BN is less than 1 meV. Therefore, although our DFT calculations for Co adsorption on h-BN/Ru(0001) do not permit to establish unambiguously the Co adsorption site based on this tiny energy differences, the information obtained from XMCD and XMLD, as well as the results of the multiorbital Hubbard model permit to do so.

Chapter 5

CONTROLLING THE SURFACE STATE OF Au(111) AND Cu(111) BY ADSORBATES

In the previous chapters we have studied magnetic properties of Co adatoms on h-BN, with or without substrate. In this chapter, we will focus the study on electronic properties of Au(111) and Cu(111) with different adsorbates. Specially, we will put the attention on the surface state of these substrates and the changes that the adsorbates, Co among others, may induce.

5.1 Tuning the surface state

The surface of a crystal breaks the symmetry of the solid. This is the origin of some special two dimensional (2D) states that are located on the surface, the so called surface states. They spread, only, near the topmost atomic layer and cannot exist in the bulk. In reciprocal space, due to periodic potential, an energy gap opens, where real wave vector solutions to the one-particle Schrödinger equation, eq. (2.24), are forbidden. However, imaginary wave vectors solutions can exist. They are the surface states. These imaginary wave vector solutions explode in the solid, but not in the semi-infinite crystal, and they can only exist within the energy gap at the surface.

There are two types of surface states depending on the valence band states of the metal. On one hand, Shockley surface states[31] emerge from two band model formalism, which is applied to the description of *sp*- bands. This is the case of the studied surfaces, Au(111) and Cu(111). On the other hand,

Tamm surface states[32] are split-off states of d- and f- bands.

Electronic and magnetic properties of surfaces are influenced by their surface state. This makes necessary the study and to understand the different physical mechanisms that control surface states. Charge transfer between the surface and an adsorbate is one of these mechanisms. Depending on the electron affinity of the adsorbate and the surface an electron may be transferred from the adsorbate to the surface shifting down in energy the surface state. This is the case of alkali metals, such as Na[33, 35] or Cs[34] on Cu(111). The opposite situation may also occur, as in TTF-TCNQ layer on Au(111)[36]. As TTF-TCNQ molecule is more electron affine than the Au(111), electrons are transferred from the surface to the adsorbate, shifting up in energy the surface state.

Another mechanism for tuning the surface state is confinement. This mechanism is similar to a single particle in a box. In this case, if the size of the box is L, the energy of the ground state is given by

$$E_L = \frac{\pi^2\hbar^2}{2mL^2}, \tag{5.1}$$

where m is the mass of the particle. Notice that E_L is always positive. But if we reduce the size of the box by half, making the size $L/2$, the energy of the ground state is:

$$E_{L/2} = \frac{\pi^2\hbar^2}{2m\left(L/2\right)^2} = 4E_L. \tag{5.2}$$

So if we confine the surface state, we will see that it will be shifted up in energy.

The surface state can be confined by nanoporous networks[37, 38, 39, 40], also called quantum dot (QD) arrays, which form a huge family of new and exotic 2D materials to study and engineer their electronic properties. These QD arrays can be synthesize by selecting the proper components, the building blocks of QD arrays, and depositing them on selected substrates. In this way, one can obtain long-range ordered, regular and robust nanoporous networks, ranging from hydrogen-[37] or halogen-bonded[38] to metal-organic structures[39, 40]. Surface electrons are scattered by organic molecules and are confined into pores of the network. This confinement produces an upward shift of the surface state, as well as of states from the metal atoms.

Confinement is not the only mechanism present when nanoporous networks are grown on different surfaces. Metal-organic nanoporous networks (MONN) show a downshift of the surface state, as it was reported by I. Piquero-Zulaica *et al*[109]. The confinement mechanism can only shift the surface state to a higher energy, and never to a lower energy.

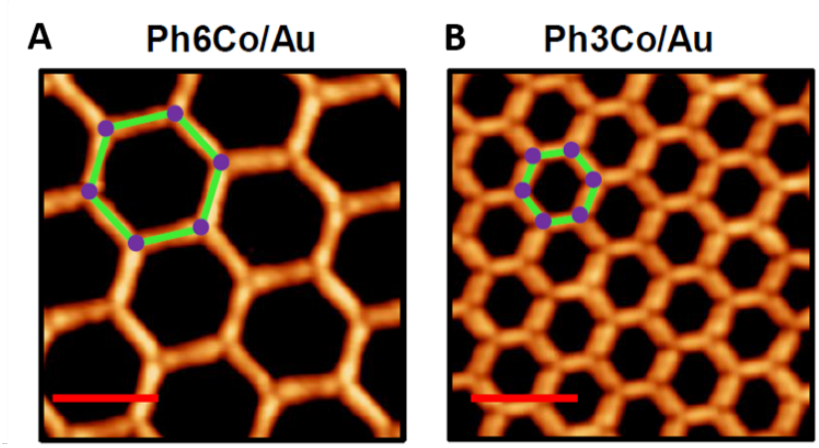

Figure 5.1: STM topographies of single domain Co-coordinated hexagonal QD arrays using (A) Ph6 and (B) Ph3. Red scale bar corresponds to 5 nm. Green lines represent organic molecules and purple dots Co atoms forming the hexagonal QD arrays. Image from [109].

This chapter aims at studying this downshift and explain it. In their work, I. Piquero-Zulaica *et al*, grew two homothetic (scalable) metal-organic nanoporous networks on Au(111), see fig. 5.1, by evaporating sequentially dicarbonitrile-terphenyl (Ph3) or dicarbonitrile-sexyphenyl (Ph6) molecules and Co atoms in a 3:2 stoichiometry, followed by a mild annealing to 400 K. In agreement with previous work [110], both networks show sixfold symmetry and enclose pore areas of 8 nm^2 for Ph3Co network and 24 nm^2 for Ph6Co.

ARPES measurements[109] on these hexagonal structures showing the band structure of system are presented in fig. 5.2. The second derivative of the ARPES spectral density along the $\overline{\Gamma M}$ high symmetry direction from Ph6Co and Ph3Co are shown. A gradual downshift of the fundamental energy at $\overline{\Gamma}$ point is observed as the pore size is reduced. This can be quantified from the normal emission energy distribution curves (EDC), fig. 5.2c and table 5.1. The measured downshift of the surface state is 40 meV for Ph6Co network and 100 meV for Ph3Co. Note that this behaviour goes in opposite direction to the energy shift expected from conventional lateral confinement. Therefore, another mechanism must be involved as well.

First, we focus on the confinement effect. Using Scanning Tunnelling Spectroscopy (STS), it is possible to verify that these MONN confine the surface state of Au(111), similar to what happens in Ag(111)[110]. Figure 5.3a shows the STS data obtained at two different positions of the Ph6Co network. In order to compare Au(111) and Ag(111) data, a shifted onset has been used. The agreement between these two datasets is quite reasonable,

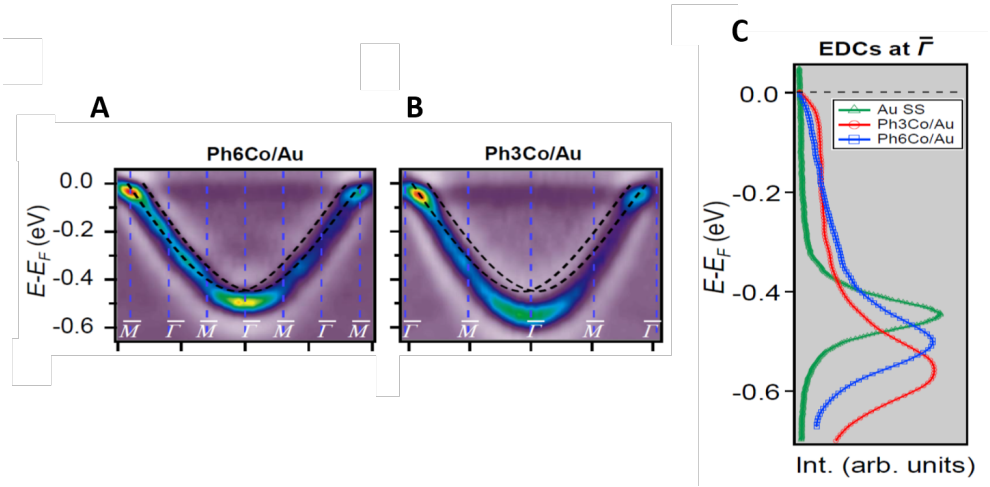

Figure 5.2: Second derivative of the spectral density obatined by ARPES at 150 K along $\overline{\Gamma M}$ high-symmetry direction (A) for Ph6Co and (B) for Ph3Co MONN. The band structure exhibits downward shifts of the band bottom and gap openings at the superstructure symmetry points compared to the pristine Au(111) surface state (black dotted lines). (C) Energy distribution curves at normal emission ($\overline{\Gamma}$ point) for pristine Au(111) (green), Ph6Co (blue) and Ph3Co (red). Image from [109].

demonstrating that the confinement properties of Ph6Co are similar for both substrates. Therefore, the conductance spectra together with the dI/dV maps taken at different voltages, fig. 5.3b to e, exhibit confinement resonances within the pores.

Different factors might be responsible for these downshift of the confined surface states with respect to the pristine Au(111) surface. One possibility is some network-substrate interaction in the form of charge transfer, similar to the shift induced by alkali metals [111]. However, the fact that m^* decreases and the Fermi wave-vector k_F is practically pinned suggests the

Table 5.1: ARPES experimental binding energies at $\overline{\Gamma}$ and effective masses (columns $E_B^{\overline{\Gamma}}$ and m^*/m_0) for the substrate and the two networks).

System	$E_B^{\overline{\Gamma}}$ (eV)	m^*/m_0
Au(111)	0.45	0.255
Ph6Co	0.49	0.24
Ph3Co	0.55	0.22

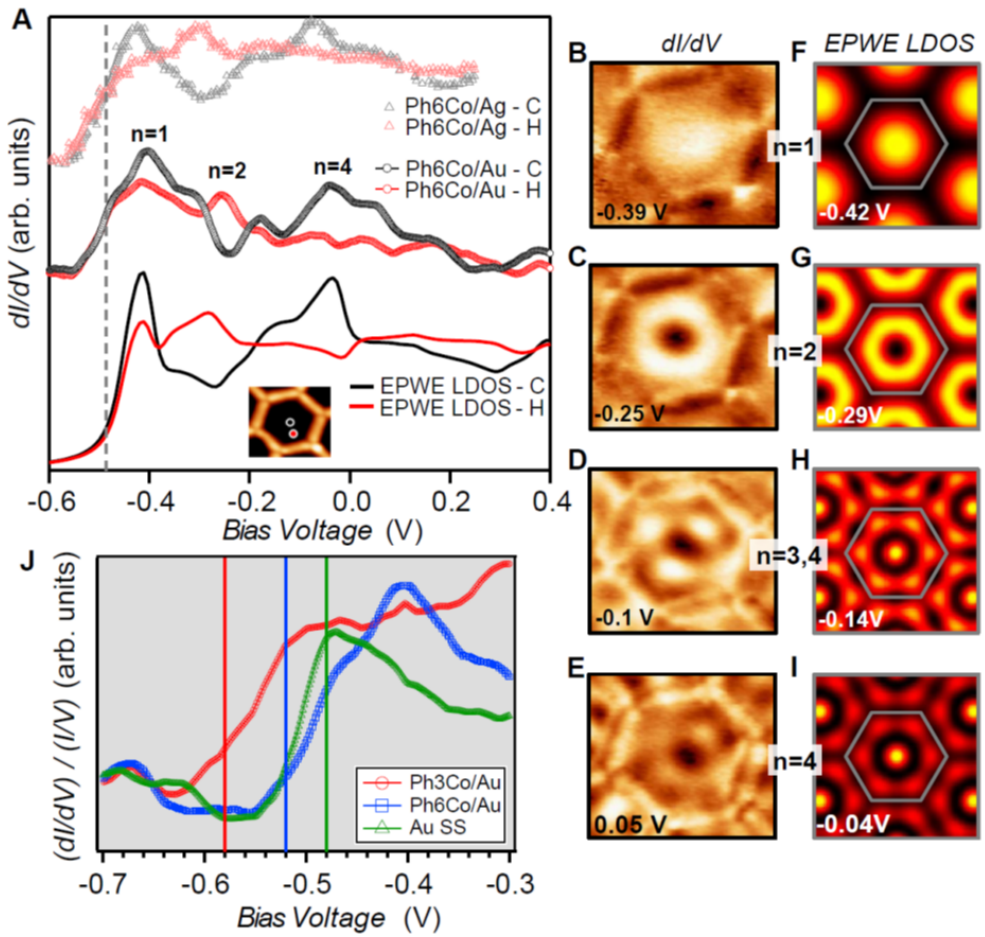

Figure 5.3: Local confinement and renormalization effects observed by STM/STS. (A) dI/dV spectra at the pore center (black) and halfway (red) for three Ph6Co datasets: Experimental curves of Ph6Co on Au(111) (middle), corresponding electron plane wave expansion (EPWE) conductance simulation using the ARPES parameters (bottom), and experimental spectra of Ph6Co on Ag(111) adapted from reference [110] and normalized to the Au(111) 2D electron gas (top). (B to E) Experimental dI/dV maps reproducing standing wave patterns of different energy levels n showing excellent agreement with the EPWE simulated ones at similar energies (F to I). (J) Zoom-in onto the experimental dI/dV onset for the pristine Au(111) surface state (green) and Ph6Co (blue) and Ph3Co (red) networks probed at the center of the pores.

conservation of the electron occupancy of the 2D electron gas (electron density $n = \frac{k_F^2}{2\pi}$)[112]. Therefore, the Au(111) surface state shift is not driven by

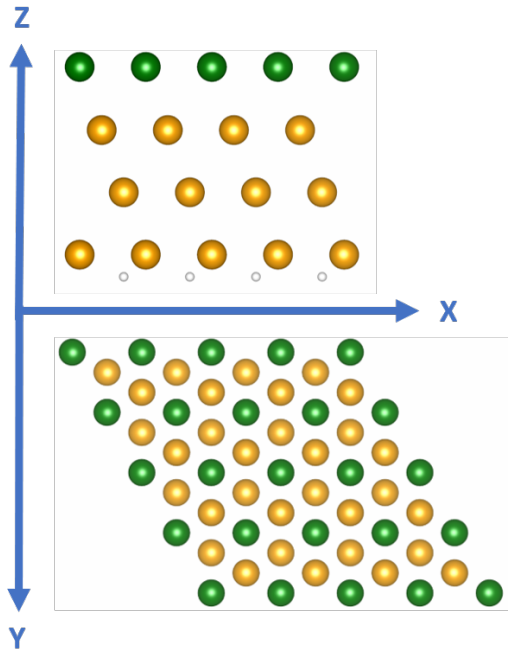

Figure 5.4: Side (top) and top (bottom) view of the Au(111) passivated slab. Yellow spheres represent bulk Au atoms, while green spheres surface ones and white H atoms.

electron charge transfer from Co atom to the Au surface and, indeed, does not appear in our DFT calculations.

As it will be shown in the next sections, the downward shift of the surface state reflects the weak hybridization between the Co atom and the Au surface.

5.2 Modelization of the surface state

The first thing to do is to model the surface state of the Au(111) substrate. In doing so, we use the characterization of the Au(111) surface state proposed in the thesis of Nora González-Lakunza[36, 43]. Our aim is to study the downshift of the Au(111) surface state due to the hybridization with the Co atom and to reproduce the trends observed in experiments.

Our simulations use a slab of atomic layers to model the desired surface. Increasing the number of atomic planes improves the description of the continuous band structure of the metal. If the Au slab is symmetric, there are two (111) surfaces. Therefore, we have two surface states. Both surface states have similar energy and dispersion. In this case, we obtain two non-

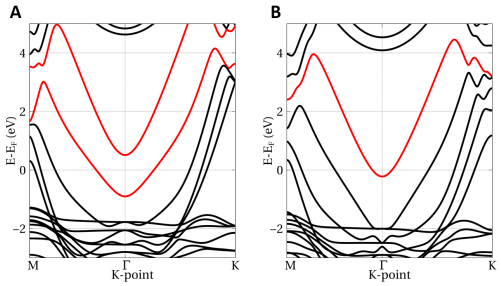

Figure 5.5: Calculated band structure of Au(111) 4 layer slab using the 1×1 unit cell.(A) Symmetric slab and (B) slab passivated with H atoms on the bottom. Red bands correspond to the surface state.

degenerate surface states. The "true" surface state energy will be in between these two state energies.

In order to quench one of the surface states, and obtain a more realistic description of the surface state, we passivate with H atoms the bottom face of the slab, see fig. 5.4. The resulting band structure, see fig. 5.5b, shows only one surface state, which is localised on the surface that has no H atoms, at 222 meV below E_F. Although the obtained binding energy of the Au(111) surface state does not agree with the experimental one, see table 5.1, this description of the surface state is enough to reproduce the experimental trend.

To test the model, we will put a molecular layer, pyrazine layer, on the non-passivated face of the Au(111) slab at 3.5 Å height, see fig. 5.6. We use a 2×2 supercell and, as the pyrazine does not enter in this supercell, we tilt the molecule by 15º for the calculations.

The pyrazine molecular layer scatters surface electrons and does not permit them to penetrate so much in vacuum. Therefore, the molecular layer confines the surface state in the perpendicular direction of the surface. This causes an upward shift of the Au(111) surface state, as it is showed in fig. 5.6b. The calculated upward shift of the Au(111) surface state is 390 meV, becoming empty. This upward shift follows expected trends, also previously observed for naphthalene tetracarboxylic diimide (NTCDI, $C_{14}H_8N_2O_4$) and 1,4-bis(4,6-diamino-1,3,5-triazin-2-yl)benzene (BDG, $C_{12}H_{12}N_{10}$) molecular layers adsorbed onto Au(111)[113].

These results confirm that our model describes correctly the Au(111) surface state, at least to study locally the interaction with an adsorbate. Therefore, we will use it to study the interaction of Co atoms with the Au(111) surface.

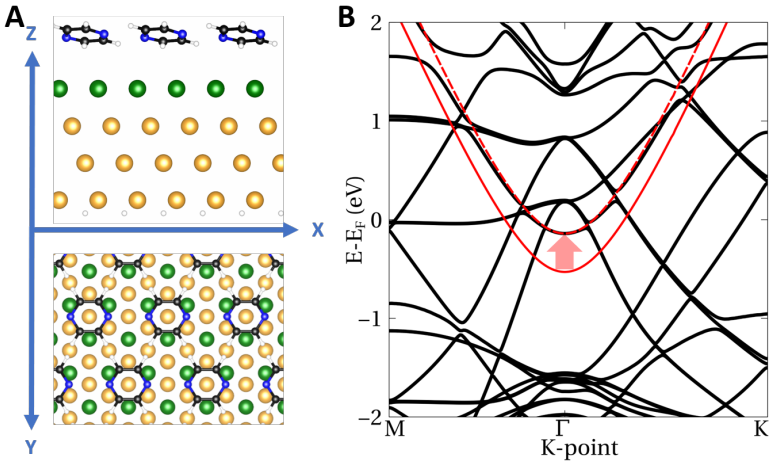

Figure 5.6: (A) Side (top) and top (bottom) view of the passivated Au(111) slab with a pyrazine molecular layer. Same colour code of fig. 5.4 for yellow, green and white spheres, while black spheres represent C atoms and blue spheres N atoms. (B) Band structure of 2×2 supercell of a passivated 4 layer Au(111) slab with a pyrazine molecular layer. Solid red line is the surface state of the pristine Au(111) surface as it is obtained in the 2×2 supercell. Dashed red line are a guide to follow the Au(111) surface state shifted by the molecular layer.

5.3 Weakly interacting adsorbates on Au(111) surface

In this section we will study the effect that Co or Au arrays have on the Au(111) surface state. In addition, we shall also consider Cu arrays on the Cu(111) surface.

5.3.1 Co adatoms

As it was previously mentioned, the downward shift of the surface state reflects the local Co hybridization with the Au substrate. We explore the weak Co-Au hybridization by putting Co atom arrays on a non-reconstructed Au(111) surface, but at larger adsorption distance than the optimal one to simulate the situation of the metal-organic network.

First of all, notice that the downward shift measured in experiments is smaller for Ph6Co network than for Ph3Co network. Consequently, when Co concentration is smaller, the downward shift is smaller, as the pore formed by Ph6Co is bigger than the pore formed by the Ph3Co network. In the

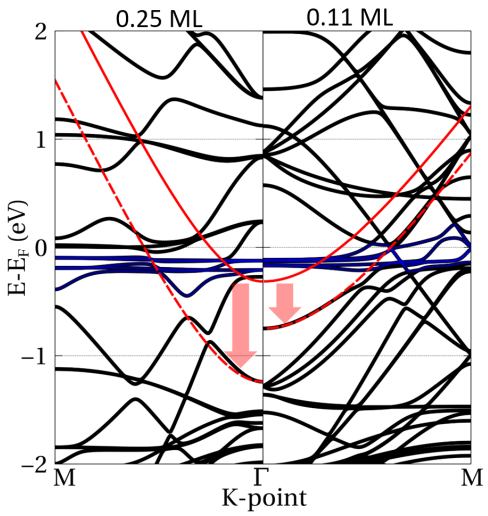

Figure 5.7: Visualization of the Au(111) surface state (continuous red curve for the pristine case) downward energy shift at two different Co coverages. The vertical arrows show the calculated shift close to Γ and the red dashed lines are a guide to the eye to follow the shifted surface state. The left panel corresponds to 0.25 ML of Co and the right panel to 0.11 ML, as obtained by using a 2×2 and a 3×3 supercell, respectively. The different supercells introduce an evident difference in the folding of Au bands (black lines). The blue curves close to the Fermi level correspond to Co adatom *d*-bands. The coupling between the Co *d*-bands and folded bulk-bands with the Au(111) surface state pushes it downwards in energy, the shift being larger at higher Co coverages.

experimental networks, the concentration of Co is 0.015 monolayers (ML) for Ph3Co network and 0.005 ML for the Ph6Co network. These are very small concentrations, 1 Co atom per 67 and 200 Au surface atoms for Ph3Co and Ph6Co networks, respectively. Therefore, we need 8×8 and 14×14 supercells to have similar Co concentrations, which is computationally too expensive. So we will work with smaller supercells, between 2×2 and 3×3, where the concentration of Co is higher than in the experiment (0.25 ML and 0.11 ML, respectively) to see the trends and extrapolate to explain the observations.

Another important point to take into account in these calculations is the height of the Co atoms from the Au(111) surface. Ph3 and Ph6 molecules are coupled to Co atoms and henceforth the coupling between Co and the Au surface is weaker than if only Co is adsorbed. So the distance from the Au(111) surface to Co atom must be larger than the optimal Co adsorption

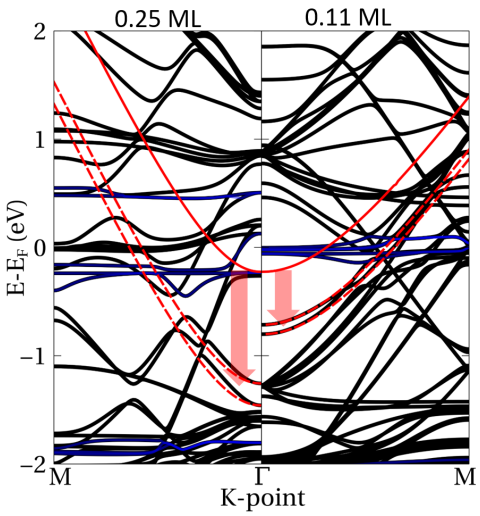

Figure 5.8: Same as fig. 5.7 with spin polarization. Visualization of the Au(111) surface state (continuous red curve for the pristine case) downward shift at two different Co coverages. The vertical arrows show the calculated shift close to Γ and the red dashed lines are a guide to the eye to follow the shifted surface states with different spin polarizations. The left panel corresponds to 0.25 ML of Co and right panel to 0.11 ML, as obtained by using a 2×2 and a 3×3 supercell, respectively. Different supercells introduce different Au band foldings (black lines). The blue lines correspond to Co adatom *d*-bands.

distance on Au(111) surface. For these calculations we put the Co atom at 2.5 Å from the surface.

In fig. 5.7, we can see the calculated band structures from two selected supercells: 2×2 (0.25 ML) on the left and 3×3 (0.11 ML) on the right. These superstructures introduce an evident difference in the folding of Au bands, but more importantly, a clear downshift of the pristine Au(111) surface state. We find that the magnitude of the downshift is directly related to the amount of isolated Co adatoms on the surface.

Notice that Co atom *d*-states (in blue) are close to the Fermi energy. More accurately, they appear between the surface state and the Fermi level. So, *d*-states from Co push down the surface state by hybridization. This hybridization creates the bonding and antibonding states but, as we are in the weak coupling regime, they still maintain their original characters, surface state and *d*-states characters.

Although geometrical variations of the overlayer, in the form of vertical displacements, could affect the surface state reference[39, 114, 115], the

hybridization of Co *d*-bands with Au(111) surface state explains the experimentally observed surface state renormalization, see fig. 5.13.

We include spin-polarization to our calculations, while we maintain the Co at 2.5 Å from the surface. Typically, adsorption distances obtained from spin-polarized calculations are larger than for non-spin-polarized calculations. However, 2.5 Å is still larger than the optimal adsorption distance for spin-polarized calculations, so we continue in the weak hybridization regime.

In fig. 5.8, we can see the calculated spin-polarized bands-structure from the 2×2 supercell (0.25 ML) on the left and the 3×3 (0.11 ML) on the right. The downward shift measured before is confirmed with spin-polarized calculations. Although the spin polarization makes difficult to obtain a value for the shift, since surface state is split into majority and minority spin states, the calculated shift is of the same order of magnitude than the obtained for non-spin-polarized calculations.

5.3.2 Au adatoms

In order to check if the downward shift of the surface state due to hybridization appears with other arrays of metallic atoms, we change the Co atom for another atom that has occupied *d*-states. In this case, we choose Au atom.

The optimal bonding distance of Au is larger than for Co. This means that we have to put the Au adatom further from the surface. However, the distance cannot be so large that there is no interaction. So, the absorption distance that we use is 3 Å in the weak hybridization regime.

The band structure for Au adatom on Au(111) is showed in fig. 5.9. The downward shift of the Au(111) surface state with Au adatom is similar to the shift with Co adatom. However, *d*-bands of Au adatom are close to the valence band of the substrate and below the surface state. Consequently, we can discard that the downward shift is an effect of the electrostatic interaction. Hybridization between the Au adatoms, and the folded substrate bands, with the Au(111) surface state appear as the cause of this effect.

Next, we will consider the more reactive Cu(111) surface under two different coupling regimes, weak and strong.

5.4 Cu adatoms on Cu(111)

In order to study the Cu(111) surface, we will use the same model as for the Au(111), a 4 layer slab with one of the faces passivated with H atoms. This description of the Cu(111) surface state gives us that the Cu(111) is 530 meV below Fermi level.

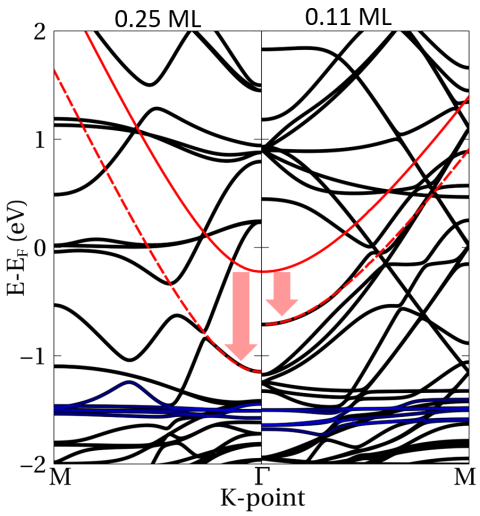

Figure 5.9: Au(111) 4 layer slab band structure for two different Au coverages. The color code is the same as in fig. 5.7, except for blue lines that correspond to Au *d*-bands. The left panel corresponds to a coverage of 0.25 ML of Au and the right panel to 0.11 ML. Au adatom *d*-bands, in blue, are below the surface state, far from the Fermi energy.

5.4.1 Weak interaction regime

For the Cu(111) surface, we select Cu atom as the adatom since it has been reported as linker in metal-organic networks on this surface[39, 116, 117]. In order to be in the weak hybridization regime, we put the Cu adatom at a distance of 3 Å from the Cu(111) surface.

The band structure of Cu adatom on the passivated 4 layer Cu(111) slab is showed on fig. 5.10. In this case, we have again the same trend than for Co and Au onto Au(111). The downward shift of the surface state is not only seen in Au(111) surface, it appears also in Cu(111) surface. The difference is that the downward shift is smaller for the low coverage in comparison with Co and Au adatoms on Au(111) surface. Notice that, in this case, the position of *d*-bands of Cu adatom is very close the pristine Cu(111) surface state.

Now, we can state that for Au(111) and Cu(111) surfaces the adsorption of homoatomic and heteroatomic arrays exhibit the downward shifting effect whenever the hybridizations are not strong (physisorption cases), such that the surface state character is maintained. This commonly applies to MONN since the molecules slightly pull the adatoms away from the surface[39, 114, 115], effectively reducing its coupling the the surface.

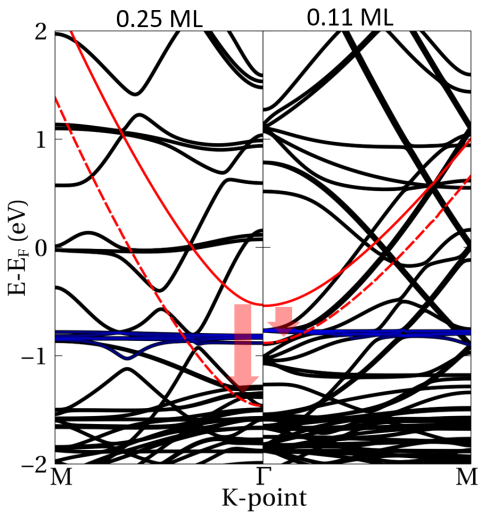

Figure 5.10: Passivated Cu(111) 4 layer slab band structure for two different Cu coverages. The Cu(111) surface state (continuous red line corresponding to the pristine case) downward shift can be seen at the two different Cu coverages. The vertical red arrows show the calculated shift close to Γ and the red dashed lines are a guide to follow the shifted surface state. The left panel corresponds to 0.25 ML of Cu and the right panel to 0.11 ML. As we use different supercells for each coverage the folding of Cu bands (black lines) is different on each panel. Blue lines correspond to Cu adatom *d*-bands.

5.5 Strong interaction regime

Previous studies of Cu-coordinated MONN on Cu(111)[39, 116, 117] did not report such a counter-intuitive downward shift of the surface state. The MONN of those works is shown in fig. 5.11. The growing technique of such a structure is different from the previous one. In this case, the organic molecule, 4,9-diaminoperylene-quinone-3,10-diimine (DPDI), is deposited on the surface below one ML coverage, which are mobile on the Cu surface. The molecules are frozen by decreasing the temperature to 5 K before annealing at 200 ºC to dehydrogenate N atoms, but also generate Cu adatoms from the surface. By this method, the MONN is formed for coverages below 0.73 ML, as each Cu adatom is coordinated to two N atoms from two adjacent molecules at the node.

In the previous MONNs, Ph6Co and Ph3Co from fig. 5.1, the metallic linker was only one Co atom, which was evaporated sequentially with the organic molecule. In contrast, the metallic linker of DPDICu MONN is a Cu trimer that has been taken from the surface, i.e., segregated Cu adatoms.

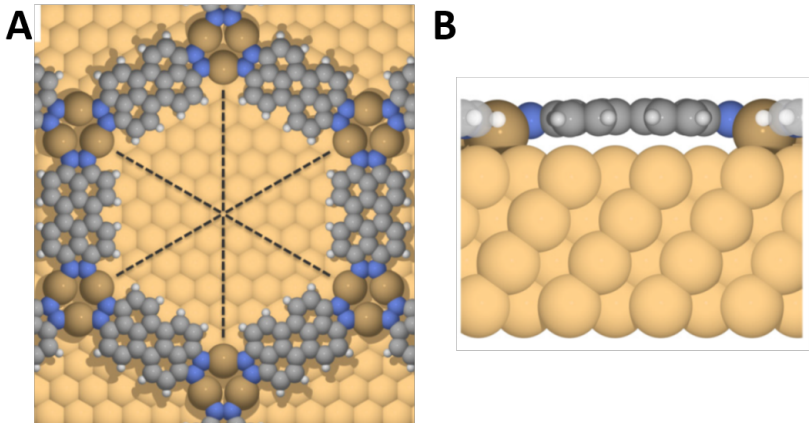

Figure 5.11: Visualization of the MONN studied in [39]. In this system, there are two different type of Cu atoms, Cu atoms from the substrate and from the MONN, represented by light and dark yellow spheres, respectively. Blue, grey and white spheres indicate N, C and H atoms, respectively. (A) Top and (B) side views of the system. Image taken from[39].

This makes a big difference as the Cu trimer is close to the surface, making the Cu-Cu(111) hybridization strong.

In order to simulate this strong hybridization, we bring the Cu adatom closer to the surface, to 2.5 Å and repeat the calculation in the 2×2 supercell.

In fig. 5.12, the band structure of close Cu adatom on the passivated 4-layer Cu(111) slab is showed. The surface state is now splitted into two bands, bonding and anti-bonding states, 1.5 eV below Fermi energy and 1 eV above Fermi energy, respectively. In this case, the bonding state is mixed with valence bands of the substrate. Thus, ARPES experiment should show the antibonding state, which is higher in energy than the original surface state and acquires surface state character.

The experiments were not able to see the downward shift of the surface state on Cu(111) with DPDICu MONN due to the strong hybridization of the *d*-states from the linkers with the surface state. Although there is no direct chemical interaction between the organic ligand and the surface, the network is chemically bonded to the surface by Cu trimers. This bonding is responsible also of the bending of the DPDI molecule that can be appreciated in fig. 5.11b.

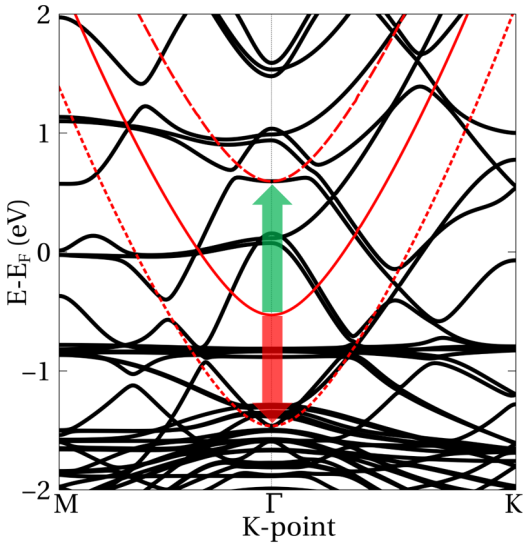

Figure 5.12: Band structure of Cu on passivated 4-layer Cu(111) slab at 2.5 Å with 0.25 ML coverage. The solid red line is where the original surface state appears in the clean Cu(111) slab, while the dashed and dotted red lines are a guide to follow the antibonding and bonding states, respectively.

5.6 Conclusion

In summary, we tested the model to describe the surface state proposed in the thesis of Nora González Lacunza[43] with a pyrazine molecular layer on Au(111). This testing system confines the surface state of Au(111) in the perpendicular direction of the surface. Due to this confinement the surface state is shifted upward, which confirms the expected trends from previous studies[113].

Apart from the upward shift, we have studied the unexpected downward shift of Au(111) and Cu(111) surface states, which was reported by Piquero-Zulaica *et al.*[109], due to weakly adsorbed metallic adatoms. Unlike other MONN, Ph3Co and Ph6Co networks show a counter-intuitive downward shift of the Au(111) surface state while the confinement effect is still confirmed by STM/STS experiments and EPWE simulations. Our DFT calculations, see table 5.2, reproduce the trends observed in the experiments, see fig. 5.13, where the linear extrapolation of DFT values is in good agreement with the experimental values. This trend was also confirmed by spin-polarized calculations for Co on Au(111) surface.

We find that the hybridization between *d*-states of the metallic adatoms and the surface state is essential to determine the direction of the shift of

Table 5.2: Energy shift of the pristine surface state obtained from DFT calculations. The calculations, from the left to right, correspond to the cases Co/Au(111), Au/Au(111) and Cu/Cu(111). To account for the decoupling effect of the molecules, Co adatom is located at 2.5 Å above the unreconstructed pristine surface, while Au and Cu adatoms are 3 Å above. The calculations show a general increasing downward shift of the surface state with adatom content. Note that the experimental amounts of Co used are significantly lower, corresponding to 0.015 ML for Ph3Co and 0.005 ML for Ph6Co.

Adatom concentration (ML)	Array size	Co/Au(111) Δ_{SS} (eV)	Au/Au(111) Δ_{SS} (eV)	Cu/Cu(111) Δ_{SS} (eV)
0.25	2×2	-0.94	-0.92	-0.93
0.17	3×2	-0.70	-0.65	-0.78
0.11	3×3	-0.49	-0.49	-0.35

the surface state. Whenever the hybridization is strong, the surface state character is lost and our DFT model cannot determine it. The reason for this is the high concentration of adatoms that we have in our calculations calculations. In contrast, in the experiment, the bonding state, resulting from the strong hybridization between the surface state and the Cu *d*-states, is mixed with valence band states of Cu(111) substrate, while the antibonding state is what ARPES measurements probes.

On the weak hybridization regime, the surface state character is retained, in spite of the high concentration of our calculations, and we were able to reproduce the experimentally observed downward shift of the surface state, see fig. 5.13. We assign this downward shift as an effect of the weak hybridization between the surface state and *d*-bands of the adsorbate. We notice also that the downward shift happens when the bonding state do not mix with valence bands, as it is the case of Cu on Cu(111) at 3.0 Å and Au and Co on Au(111) at 3 Å and 2.5 Å, respectively. The adsorption distance on all these cases is larger than their optimal adsorption distance in order to be in the weak hybridization regime, and simulate the effect of metal-organic networks[109, 110].

In conclusion, our single description of weakly adsorbed *d*-adatoms can explain the downward shift observed in the experiment with Ph3Co and Ph6Co networks, see fig. 5.2. Organic molecules, Ph3 and Ph6, are reducing the hybridization between the *d*-states from Co adatoms and Au(111) surface state. The shift of the surface state is very sensitive to the balance between

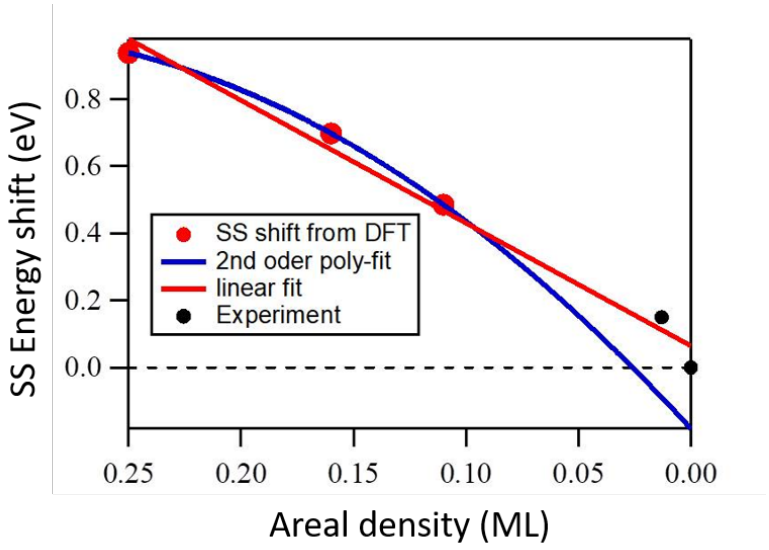

Figure 5.13: Energy shift of the Au(111) surface state due to the Co adatom concentration. Red dots correspond to values obtained from DFT calculation while black dots were experimentally measured. Red and blue lines are linear and second order fitting of DFT values, respectively. The linear fitting is giving quite good agreement between the experimental and theoretical values of the surface state energy shift.

charge transfer, confinement and the hybridization with d-states.

Chapter 6

CONCLUSIONS

Overall, in this thesis we have demonstrated that the Co has different magnetic properties on different chemical environments, in spite of having similar d shell occupation. The main part of the thesis is devoted to study the magnetic anisotropy of Co on h-BN. We developed a new method to construct a crystal field Hamiltonian and introduce it in the multiorbital Hubbard model[30]. We have compared the obtained results with other theoretical approaches and experimental data. In the case of 0-dimensional systems, as magnetic adatoms, one needs to go beyond Density Functional Theory (DFT) to get a quantitative agreement between measured and calculated Magnetic Anisotropy Energy (MAE). The use of Maximally Localized Wannier Functions (MLWFs) introduces a new set of parameters that need to be fixed and the MAE is very sensitive to them. If a nice description of the system in terms of MLWFs is obtained, the method provides qualitatively good results in quantitative agreement with experiments. This was done for Co on h-BN/Ir(111) and h-BN/Ru(0001), where it unveiled the different adsorption sites of Co depending on the metallic substrate, hollow site with almost no magnetic anisotropy for Co on h-BN/Ir(111) and atop N with a larger out-of-plane anisotropy for Co on h-BN/Ru(0001).

We started by considering the problem of Co adsorbed on a free standing h-BN monolayer. We saw that Co atoms adsorb in the weak chemisorption regime, where Van der Waals forces play an important role. Moreover, we demonstrated that there are two possible adsorption sites close in energy, with hollow site as the preferable adsorption site. We also extracted that the d-shell occupation of Co on both adsorption sites is 7.8 electrons, which corresponds to a spin $S \simeq 1$.

Regarding the magnetic anisotropy of both sites, we performed DFT+SOC calculations and obtained a significantly higher out-of-plane easy axis anisotropy for the atop N site and a smaller in-plane MAE for the hollow. Then, from the

multiorbital Hubbard model using MLWFs, we obtained results in qualitative agreement, but an order of magnitude higher MAE values. We confirmed this results by extracting a spin Hamiltonian and calculating its parameters. Comparing the three methods, we found a qualitatively good agreement between them.

Afterwards, we have studied the effects of Ir(111) and Ru(0001) substrates on the magnetic properties and compared them with the experimental data. First, we studied the effect that those substrates have on h-BN. We demonstrated that the corrugation is larger on Ru(0001) than on Ir(111). These results showed that the Ir(111) substrate has little effect on the h-BN and, thus, it acts as the free standing h-BN. Therefore, the hollow site is assumed for Co on h-BN/Ir(111), as it was found for the free standing h-BN. Then, we have confirmed that the hollow adsorption site of Co on a far region of the h-BN on Ru(0001), and the atop N site on a close region have similar adsorption energies. These DFT results suggest that the adsorption site of Co on h-BN/Ru(0001) could be either atop N or hollow. Thus, we use experimental data together with the multiplet fitting and the multiorbital Hubbard model results to stablish the adsorption site. X-ray Absorption Spectroscopy (XAS), X-ray Magnetic Circular Dichroism (XMCD) and X-ray Magnetic Linear Dichroism (XMLD) measurements reveal a large out-of-plane magnetic anisotropy for Co atoms on h-BN/Ru(0001), while on h-BN/Ir(111) have basically no anisotropy, consistent with atop N and hollow adsorption sites, respectively.

XAS data agrees on the spin $S = 1$ obtained for Co atoms on both substrates. In addition, multiplet calculations correctly reproduce the main trends in the magnetic anisotropy, thus, only confirming that Co on h-BN/Ru(0001) and on h-BN/Ir(111) are atop N and hollow sites, respectively.

Adsorption sites of Co for the two surfaces are also supported by the multiorbital Hubbard model. The agreement between the S, S_z, L_z and Zero Field Splitting (ZFS) values of the atop N site within the multiorbital Hubbard model and the experimental Co/h-BN/Ru(0001) XAS, XMCD and XMLD data is very good. The average spin and orbital moments saturate for fields around 3 T in both, experiments and model. Additionally, the obtained ratios (m_L/m_S) in the experiments for normal and grazing incidence are close the one obtained in the model.

Although the model for the hollow site predicts a magnetic anisotropy larger than the measured one for Co/h-BN/Ir(111), the qualitative agreement is good. This is due to the fact that the anisotropy of the hollow site is much more sensitive to small changes in the surrounding environment like corrugation, charge transfer or lattice strain.

Finally, we have also studied the effect of weakly adsorbed Co, Au and

Cu arrays on the Shockley surface state of Au(111) and Cu(111) surfaces. In particular, Angle Resolved Photo-Emission Spectroscopy (ARPES) and Scanning Tunnelling Spectroscopy (STS) measurements reveal a gradual energy downward shift of the Au(111) surface state upon the formation of two homothetic Co coordinates metal-organic networks. This counterintuitive downshift is gradual with decreasing pore size, despite the coffining attribute to the nanocavities, which upshift the surface state.

The downward shift of the surface state happens in the weak hybridization regime of *d*-atoms arrays on noble metal surfaces and it becomes stronger with the adatom concentration, as it happens for Co-dicarbonitrile-terphenyl (Ph3Co) and Co-dicarbonitrile-sexyphenyl (Ph6Co) Metal-Organic Nanoporous Networks (MONNs). We speculate that, in the experiment, the interaction of the Co atoms with the surface is not so strong due to the presence of Ph3 and Ph6 molecules. We assume that the molecules push the Co atoms from their optimal adsorption distance, and place them at the weak hybridization distance. Nevertheless, if the hybridization is strong, or for high concentrations, the downward shift of the surface state disappears because it mixes with valence bands and it looses its surface state character. In addition, other MONNs onto noble metal surfaces should show such subtle counterintuitive downward shift whenever the surface state character is preserved, i.e., for weak coupling cases.

Appendix A

Co on 4x4 h-BN: Limits of the MLWFs method

In order to obtain the crystal field from the MLWFs for our multiorbital Hubbard model, we used a 3×3 supercell. A priori, it would be more convenient to use the 4×4 supercell that better matches with the rotation of Ir(111) and Ru(0001). Even though Ir and Ru have different 3D Bravais lattices, the surface unit cell is very similar for both substrates: an hexagonal unit cell with a lattice constant of 2.72 Å. After a rotation of 13.9°, this surface matches very well with a 4×4 h-BN supercell, with a mismatch of 2.4%. Since the 4×4 h-BN monolayer that matches with the surfaces has a compressive stress, the lattice parameter of the supercell is slightly smaller than the optimal one, and the h-BN will have a small corrugation.

The MLWFs basis for the 4×4 h-BN monolayer contains the sp_2 and p_z orbitals for N atoms and s and d orbitals for the Co. In order to describe correctly the system, we select the disentanglement energy window from -22 eV to 2 eV referring to the Fermi energy, and the frozen energy window from -1.5 eV to 0.5 eV.

The bandstructure obtained of both adsorption sites for the 4×4 supercell do not show the same quantitative agreement than the 3×3 supercell, see fig. 3.6 and fig. A.1. However, the d-bands of Co seem in reasonably qualitative agreement. Therefore, we reduce the hamiltonian obtained with this basis and introduce it as the crystal field.

For 8 electrons in the d-shell of Co, the expected total angular momentum and spin quantum numbers for the ground state are again $L = 3$ and $S = 1$, respectively. After applying the crystal field term, the ground state, whose total initial degeneracy was 21, ends in a triplet ground state with total degeneracy 3, see fig. 3.8 and fig. A.2. The ground state for atop N site is now the one with $\langle L_z \rangle = \langle S_z \rangle = 0$, contrary to the 3×3 case. But also the

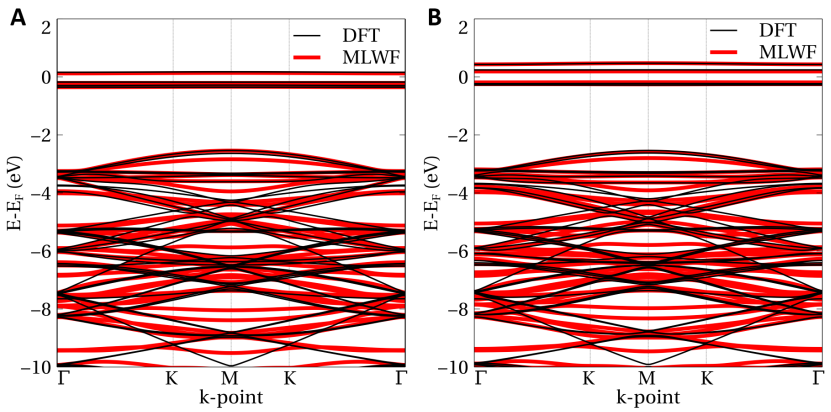

Figure A.1: Bandstructure of Co on h-BN monolayer for a 4×4 supercell from DFT (black lines) and MLWF (red lines) calculations. Left panel (A) corresponds to the atop N adsorption site, while the right panel corresponds to the hollow site.

quenching of $\langle L_z \rangle$ and $\langle S_z \rangle$ change in the 4×4 supercell. The quenching for the atop N site is higher than for the hollow site, which makes the ZFS bigger for the hollow site. On the opposite side is the hollow site, where it is expected to found a hard axis in the out-of-plane direction. However, the expectation values of $\langle S_z \rangle$ seem to indicate an easy axis.

Another source of error is the reduction of the dimension of the Hamiltonian obtained from the MLWFs calculation to perform the multiplet calculations. This step is necessary as the computational cost increases with the dimension of the matrix that we want diagonalize, but we are missing same contributions that may be important for the magnetic properties.

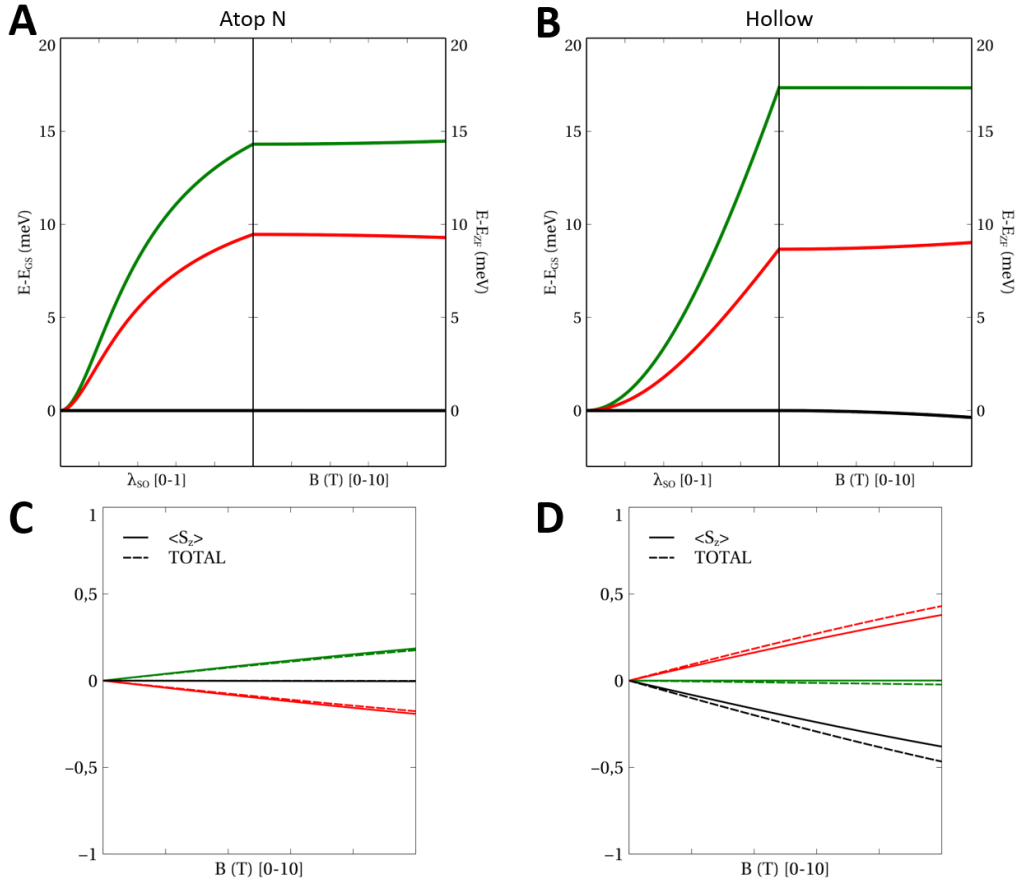

Figure A.2: Top panel, (A) and (B), show multiplet low energy excitation spectra of Co on a 4×4 h-BN monolayer in d^8-electronic configuration for spin-orbit coupling strength (λ_{SO}) and magnetic field applied perpendicular to the h-BN plane. Bottom panels, (C) and (D), show the expectation values $\langle L_z \rangle$ (dashed lines and $\langle S_z \rangle$ (solid lines) for the three lower energy states corresponding to the effective $S = 1$ anisotropic spin. Black colour is used for the ground state, red for first excited state and green for second excited state.

Appendix B

Fe on h-BN

In this appendix, we will study the Fe adatom on free standing h-BN.

B.1 Adsorption of Fe on h-BN

Fe on h-BN has 7 d-electrons with a small energy difference between the atop N and hollow adsorption sites.

B.1.1 Spin-polarized DFT and DFT+U calcualtions

We perform spin-polarized relaxation for both adsorption sites using the same parameters as for Co. In the case of Fe on atop N site, the adatom is placed 2.03 Å above the N atom, while on the hollow site it is placed 1.96 Å above the plane formed by first neighbour N atoms.

The spin-polarized calculations give the PDOS showed in fig. B.1. The energy integration of the PDOS curves onto $3d$ states of Fe up to the Fermi level gives around 6.8 electron in the d-shell of Fe for both adsorption sites, see table B.1, as expected 1 electron less than Co. This occupation corresponds to a spin $S = 3/2$ localized in the $3d$ shell of the Fe atom. Comparing the PDOS for Fe and Co, fig. B.1 and fig. 3.5, we notice that the component that is lost in the case of Fe, as it has 1 electron less in the d shell, is the minority spin d_{z^2} state.

The relatively sharp peaks that appear on the PDOS for both adsorption sites is consistent with a weak hybridization between the $3d$ atom states and the h-BN states, as it happened for Co. The hybridization of both adsorption sites is similar to the hybridization found for Co: on the atop N site, the d_{z^2} state of Fe is hybridized with the p_z state of N, while on the hollow site the d_{yz} and d_{xz} states hybridize with the p_z states of first N and B neighbours.

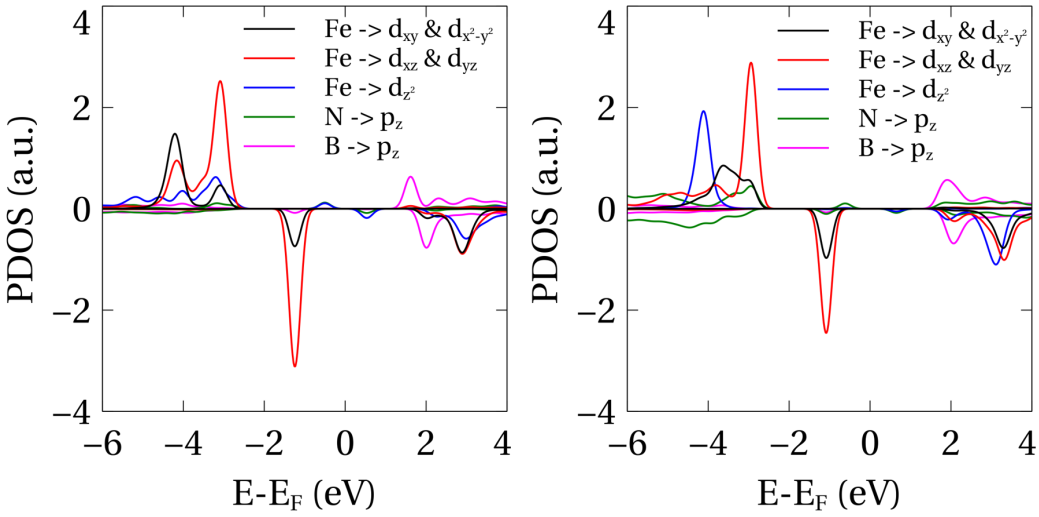

Figure B.1: Projected density of states (PDOS) onto $3d$ orbitals of Fe and p_z orbitals of first neighbour N and B atoms once for atop N (left) and once for hollow (right) adsorption sites, as obtained from the spin-polarized calculations. Positive values correspond to majority-spin and negative values to minority-spin.

Moreover, we performed DFT+U calculations for both adsorption sites with the same parameters used for Co and obtained that the total energy difference is 151.4 meV in favour of the atop N site. As it happened for Co, we are in the weak chemisorption regime, and it is difficult to determine accurately the adsorption site due to the crucial role that Van der Waals forces are playing at this regime.

B.1.2 DFT+SOC calculations

We perform DFT+SOC calculations of the Fe adatom using the same parameters as for the Co.

Table B.1: Populations and spin polarization of Fe orbitals from spin-polarized DFT+U calculations.

	Total	$4s$	$3d$
Total charge	7.70	0.89	6.81
Spin up	5.78	0.86	4.92
Spin down	1.92	0.03	1.89
Polarization	3.86	0.83	3.03

Table B.2: Summary of calculated spin-moment (m_S), orbital-moment (m_L) and zero-field splitting (ZFS) of Fe atoms on a h-BN monolayer obtained from DFT calculations including spin-orbit interaction. HA and EA stand for hard axis and easy axis, respectively.

Adsorption-site	m_S (μ_B)	m_L (μ_B)	ZFS (meV)
atop N	3.20	0.13	0.13 (HA)
hollow	3.20	0.11	0.48 (EA)

We find for the Fe the opposite behaviour than for the Co: while for Co relaxation results in atop N site, for Fe it gives hollow site. DFT+SOC calculations result on a change in the adsorption site for both adatoms. The Co prefers to adsorb on hollow site, while the Fe adsorbs on atop N site. The energy difference in the case of Fe is even smaller than for Co, 152 meV.

We also find that the character of the magnetic anisotropy is reversed, see table B.2. The spin-moment is the same for Fe on both adsorption sites, and they have similar orbital-moment, which is also quenched. However the ZFS splitting is completely different and it is reversed in comparison with Co.

B.1.3 Point charge model

We used for Co, we performed multiplet calculations using a point charge model derived from DFT to obtain the crystal field. Notice that, for Fe adatom we will not use the MLWF to obtain the crystal field, as the results obtained for Co using this approach are not decisive. In the case of Fe, there is one electron less in the d-shell than in the case of Co, therefore we describe the interacting $N_e = 7$ electrons at the d-shell of Fe by the Hamiltonian, eq. (2.70).

We used the atomic values of the spin-orbit coupling ($\xi_{Fe} = 50.1\ meV$[89]) and expectation values $\langle r^2 \rangle$ and $\langle r^4 \rangle$. The distances and charges are given in table B.3.

Results of these multiplet calculations with the effective multiorbital model for Fe on pristine h-BN on both adsorption sites are shown on fig. B.2. Left panels show results for atop N adsorption site and right panels for hollow site. According to Hund rules, an atom with an atomic $3d^7$ electronic configuration has the total angular momentum and spin quantum numbers of $L = 3$ and $S = 3/2$, as we obtain in our multiplet calculations. The ground state multiplet, whit degeneracy $(2L + 1)(2S + 1) = 28$, is split by the crys-

Table B.3: Position and charges of the point charges used to calculate the crystal field contribution in the multiorbital Hubbard model for Fe adatom.

Hollow site				Atom	Atop N site			
x (Å)	y (Å)	z (Å)	q (e)		x (Å)	y (Å)	z (Å)	q (e)
1.23	0.71	−1.99	−0.50	N	0.00	0.00	−2.00	−1.50
−1.23	0.71	−1.99	−0.50	N	–	–	–	–
0.00	−1.42	−1.99	−0.50	N	–	–	–	–
0.00	1.42	−1.99	0.50	B	1.42	0.00	−2.00	0.50
1.23	−0.71	−1.99	0.50	B	−0.71	1.22	−2.00	0.50
−1.23	−0.71	−1.99	0.50	B	−0.71	−1.22	−2.00	0.50

tal field leading a cuadruplet ground state, as it corresponds to $S = 3/2$. Then, the spin-orbit coupling induces a different splitting of the cuadruplet into two doublets for both adsorption sites. For the atop N site, the high spin doublet corresponds to the ground state, while for the hollow site the low spin doublet is the ground state. These doublets are then split by the external magnetic field.

The zero-field-splitting is significantly different for both sites. In the case of the hollow site, similarly to the Co, the ZFS is in the range of few meV. Contrarily, in the case of the atop N site, the ZFS is around 40 meV, which is higher than for Co. As mentioned before, for the atop N site, the lowest doublet is formed by the high spin doublet $S_z = \pm 3/2$, while the excited state corresponds to the low spin doublet $S_z = \pm 1/2$. This is an indicator of an out-of-plane easy axis in the case of the atop N. The situation is reversed for the hollow adsorption site, where an out-of-plane hard axis is found, as the ground state is the low spin doublet, $S_z \approx \pm 1/2$, and the excited state is the high spin doublet, $S_z \approx \pm 3/2$.

From the point of the orbital moment, we see a similar behaviour than for Co, the atop N site shows a significantly larger orbital moment than the hollow site due to the N atom below, which creates a large and almost perfect crystal field. On the contrary, the hollow site has a much lower point symmetry leading to a quenching of spin and orbital moments along the direction of the field.

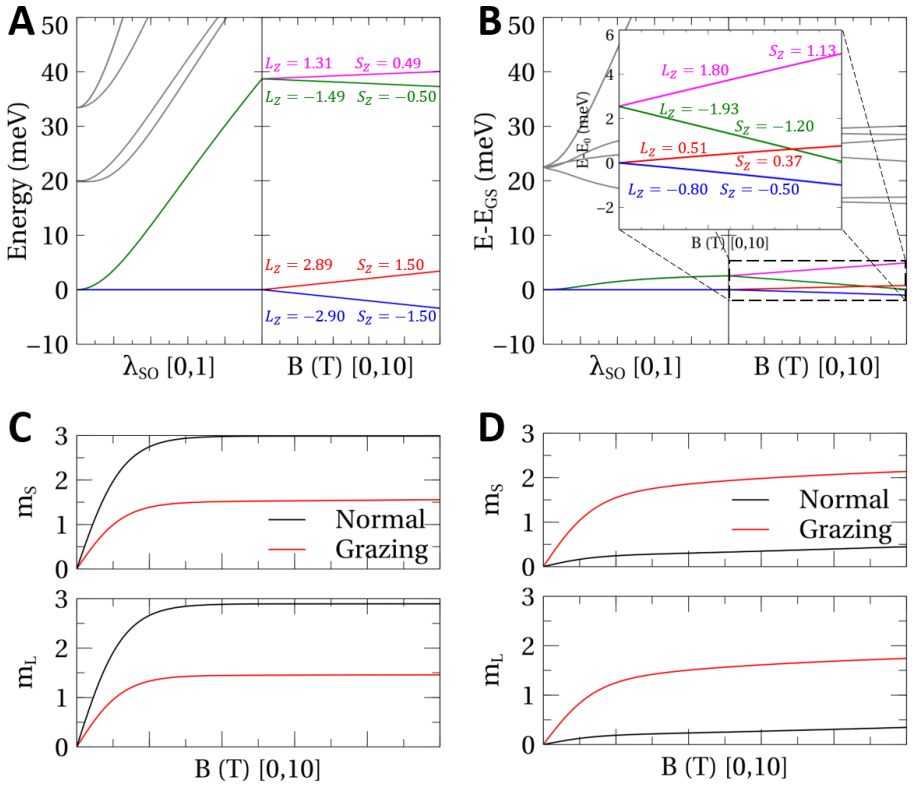

Figure B.2: (A) and (B) Multiplet energy spectra E_n versus spin-orbit coupling strength λ_{SO} and magnetic field along the out-of-plane direction for Fe adsorbed on atop N and on hollow sites of h-BN, respectively. For the spin-orbit coupling strength the energy of the ground state was taken as the reference energy, while for the magnetic field the energy of the ground state at zero magnetic field. The solid blue, red, green and purple lines correspond to the lowest four energy states, respectively, corresponding to the effective $S = 3/2$ anisotropic spin, while the light grey lines correspond to higher energy states (not considered in the discussion). The labels correspond to the spin S_Z and orbital L_Z moments at $B = 6.8\ T$. The inset in (B) is a zoom to the interested energy range. (c) and (d) Average spin m_S (top) and orbital m_L (bottom) angular momenta in the direction of the applied B field normal and grazing directions at $T = 2.5\ K$.

Bibliography

[1] David Reinsel, John Gantz, and John Rydning. Data Age 2025: The Evolution of Data to Life-Critical. *IDC White Paper; Sponsored by Seagate*, (April):1–25, 2017.

[2] Taeyoung Choi. Studies of single atom magnets via scanning tunneling microscopy. *Journal of Magnetism and Magnetic Materials*, 481:150–155, jul 2019.

[3] Sebastian Loth, Susanne Baumann, Christopher P Lutz, D M Eigler, and Andreas J Heinrich. Bistability in Atomic-Scale Antiferromagnets. *Science*, 335(6065):196–199, jan 2012.

[4] Alexander Ako Khajetoorians, Benjamin Baxevanis, Christoph Hübner, Tobias Schlenk, Stefan Krause, Tim Oliver Wehling, Samir Lounis, Alexander Lichtenstein, Daniela Pfannkuche, Jens Wiebe, and Roland Wiesendanger. Current-Driven Spin Dynamics of Artificially Constructed Quantum Magnets. *Science*, 339(6115):55–59, jan 2013.

[5] M Steinbrecher, A Sonntag, M. dos Santos Dias, M Bouhassoune, S Lounis, J Wiebe, R Wiesendanger, and A A Khajetoorians. Absence of a spin-signature from a single Ho adatom as probed by spin-sensitive tunneling. *Nature Communications*, 7(1):10454, apr 2016.

[6] Fabian D Natterer, Kai Yang, William Paul, Philip Willke, Taeyoung Choi, Thomas Greber, Andreas J Heinrich, and Christopher P Lutz. Reading and writing single-atom magnets. *Nature*, 543(7644):226–228, mar 2017.

[7] Ileana G. Rau, Susanne Baumann, Stefano Rusponi, Fabio Donati, Sebastian Stepanow, Luca Gragnaniello, Jan Dreiser, Cinthia Piamonteze, Frithjof Nolting, Shruba Gangopadhyay, Oliver R. Albertini, Roger M. Macfarlane, Christopher P. Lutz, Barbara A. Jones, Pietro Gambardella, Andreas J. Heinrich, and Harald Brune. Reaching the

magnetic anisotropy limit of a 3d metal atom. *Science*, 344:988–992, 2014.

[8] F. Donati, S. Rusponi, S. Stepanow, C. Wäckerlin, A. Singha, L. Persichetti, R. Baltic, K. Diller, F. Patthey, E. Fernandes, J. Dreiser, Z. Sljivancanin, K. Kummer, C. Nistor, P. Gambardella, and H. Brune. Magnetic remanence in single atoms. *Science*, 352(6283):318–321, apr 2016.

[9] P. Gambardella, A. Dallmeyer, K. Maiti, M. C. Malagoli, W. Eberhardt, K. Kern, and C. Carbone. Ferromagnetism in one-dimensional monatomic metal chains. *Nature*, 416(6878):301–304, mar 2002.

[10] P. Gambardella, S. Rusponi, M. Veronese, S. S. Dhesi, C. Grazioli, A. Dallmeyer, I. Cabria, R. Zeller, P. H. Dederichs, K. Kern, C. Carbone, and H. Brune. Giant Magnetic Anisotropy of Single Cobalt Atoms and Nanoparticles. *Science*, 300(5622):1130–1133, may 2003.

[11] Focko Meier, Lihui Zhou, Jens Wiebe, and Roland Wiesendanger. Revealing Magnetic Interactions from Single-Atom Magnetization Curves. *Science*, 320(82):6, 2008.

[12] Alexander Cyril Hewson. *The Kondo Problem to Heavy Fermions*. Cambridge University Press, Cambridge, UK, 1997.

[13] S Baumann, F Donati, S Stepanow, S Rusponi, W Paul, S Gangopadhyay, I G Rau, G E Pacchioni, L Gragnaniello, M Pivetta, J Dreiser, C Piamonteze, C P Lutz, R M Macfarlane, B A Jones, P Gambardella, A J Heinrich, and H Brune. Origin of Perpendicular Magnetic Anisotropy and Large Orbital Moment in Fe Atoms on MgO. *Physical Review Letters*, 115(23), 2015.

[14] William Paul, Kai Yang, Susanne Baumann, Niklas Romming, Taeyoung Choi, Christopher P Lutz, and Andreas J Heinrich. Control of the millisecond spin lifetime of an electrically probed atom. *Nature Physics*, 13(4):403–407, 2017.

[15] F Donati, Q Dubout, G. Autès, F Patthey, F Calleja, P Gambardella, O V Yazyev, and H Brune. Magnetic moment and anisotropy of individual Co atoms on graphene. *Physical Review Letters*, 111(23), 2013.

[16] F Donati, L Gragnaniello, A Cavallin, F.D. Natterer, Q Dubout, M Pivetta, F Patthey, J Dreiser, C Piamonteze, S Rusponi, and

H Brune. Tailoring the Magnetism of Co Atoms on Graphene through Substrate Hybridization. *Physical Review Letters*, 113(17):1–6, 2014.

[17] Romana Baltic, Marina Pivetta, Fabio Donati, Christian Wäckerlin, Aparajita Singha, Jan Dreiser, Stefano Rusponi, and Harald Brune. Superlattice of Single Atom Magnets on Graphene. *Nano Letters*, 16(12):7610–7615, 2016.

[18] Fabian Donat Natterer, François Patthey, and Harald Brune. Ring State for Single Transition Metal Atoms on Boron Nitride on Rh(111). *Physical Review Letters*, 109(6):066101, aug 2012.

[19] Peter Jacobson, Tobias Herden, Matthias Muenks, Gennadii Laskin, Oleg Brovko, Valeri Stepanyuk, Markus Ternes, and Klaus Kern. Quantum engineering of spin and anisotropy in magnetic molecular junctions. *Nature Communications*, 6:8536, 2015.

[20] B T Thole, Paolo Carra, F Sette, and G Van Der Laan. X-ray circular dichroism as a probe of orbital magnetization. *Physical Review Letters*, 68(12):1943–1946, 1992.

[21] Paolo Carra, B T Thole, Massimo Altarelli, and X. D. Wang. X-ray magnetic circular and local magnetic fields. *Phys. Rev. Lett.*, 70(694), 1993.

[22] A J Heinrich, J A Gupta, C P Lutz, and D M Eigler. Single-Atom Spin-Flip Spectroscopy. *Science*, 306(5695):466–469, 2004.

[23] Susanne Baumann, William Paul, Taeyoung Choi, Christopher P. Lutz, Arzhang Ardavan, and Andreas J. Heinrich. Electron paramagnetic resonance of individual atoms on a surface. *Science*, 350(6259):417–420, 2015.

[24] Cyrus F. Hirjibehedin, Chiung-Yuan Lin, Alexander F. Otte, Markus Ternes, Christopher P. Lutz, Barbara A. Jones, and Andreas J. Heinrich. Large Magnetic Anisotropy of a Single Atomic Spin Embedded in a Surface Molecular Network. *Science*, 317(5842):1199–1203, 2007.

[25] Alexander F Otte, Markus Ternes, Kirsten von Bergmann, Sebastian Loth, Harald Brune, Christopher P Lutz, Cyrus F Hirjibehedin, and Andreas J Heinrich. The role of magnetic anisotropy in the Kondo effect. *Nature Phys.*, 4:847–850, 2008.

[26] Piotr Błoński, Anne Lehnert, Samuel Dennler, Stefano Rusponi, Markus Etzkorn, Géraud Moulas, Peter Bencok, Pietro Gambardella, Harald Brune, and Jürgen Hafner. Magnetocrystalline anisotropy energy of Co and Fe adatoms on the (111) surfaces of Pd and Rh. *Physical Review B*, 81(10):104426, mar 2010.

[27] S K Panda, I. Di Marco, O Grånäs, O Eriksson, and J Fransson. Electronic and magnetic properties of single Fe atoms on a CuN surface: Effects of electron correlations. *Physical Review B*, 93(14):140101, apr 2016.

[28] L Peters, I. Di Marco, O Grånäs, E. Şaşıoğlu, A Altun, S Rossen, C Friedrich, S Blügel, M I Katsnelson, A Kirilyuk, and O Eriksson. Correlation effects and orbital magnetism of Co clusters. *Physical Review B*, 93(22):224428, jun 2016.

[29] Alejandro Ferrón, Jose Luis Lado, and Joaquín Fernández-Rossier. Electronic properties of transition metal atoms on Cu$_2$N/Cu(100). *Physical Review B*, 92(17):174407, 2015.

[30] A. Ferrón, F. Delgado, and J. Fernández-Rossier. Derivation of the spin Hamiltonians for Fe in MgO. *New Journal of Physics*, 17(3):033020, 2015.

[31] William Shockley. On the surface states associated with a periodic potential. *Physical Review*, 56(4):317–323, 1939.

[32] Igor Tamm. On the possible bound states of electrons on a crystal surface. *Phys. Z. Sowjetunion*, 1:733–735, 1932.

[33] N. Fischer, S. Schuppler, Th Fauster, and W. Steinmann. Coverage-dependent electronic structure of Na on Cu(111). *Surface Science*, 314(1):89–96, 1994.

[34] M. Bauer, S. Pawlik, and M. Aeschlimann. Resonance lifetime and energy of an excited Cs state on Cu(111). *Physical Review B - Condensed Matter and Materials Physics*, 55(15):10040–10043, 1997.

[35] G. P. Brivio, G. Butti, S. Caravati, G. Fratesi, and M. I. Trioni. Theoretical approaches in adsorption: Alkali adatom investigations. *Journal of Physics Condensed Matter*, 19(30), 2007.

[36] N. Gonzalez-Lakunza, I. Fernández-Torrente, K. J. Franke, N. Lorente, A. Arnau, and J. I. Pascual. Formation of dispersive hybrid bands at an organic-metal interface. *Physical Review Letters*, 100(15):1–4, 2008.

[37] Greg Pawin, Kin L. Wong, Ki Young Kwon, and Ludwig Bartels. A homomolecular porous network at a Cu(111) surface. *Science*, 313(5789):961–962, 2006.

[38] Ignacio Piquero-Zulaica, Jorge Lobo-Checa, Ali Sadeghi, Zakaria M.Abd El-Fattah, Chikahiko Mitsui, Toshihiro Okamoto, Rémy Pawlak, Tobias Meier, Andrés Arnau, J. Enrique Ortega, Jun Takeya, Stefan Goedecker, Ernst Meyer, and Shigeki Kawai. Precise engineering of quantum dot array coupling through their barrier widths. *Nature Communications*, 8(1):787, 2017.

[39] Manfred Matena, Jonas Björk, Markus Wahl, Tien Lin Lee, Jörg Zegenhagen, Lutz H. Gade, Thomas A. Jung, Mats Persson, and Meike Stöhr. On-surface synthesis of a two-dimensional porous coordination network: Unraveling adsorbate interactions. *Physical Review B - Condensed Matter and Materials Physics*, 90(12):1–8, 2014.

[40] Lei Dong, Zi'Ang A. Gao, and Nian Lin. Self-assembly of metal–organic coordination structures on surfaces. *Progress in Surface Science*, 91(3):101–135, 2016.

[41] Jorge Lobo-Checa, Manfred Matena, Kathrin Müller, Jan Hugo Dil, Fabian Meier, Lutz H. Gade, Thomas A. Jung, and Meike Stöhr. Band formation from coupled quantum dots formed by a nanoporous network on a copper surface. *Science*, 325(5938):300–303, 2009.

[42] Shiyong Wang, Weihua Wang, Liang Z Tan, Xing Guang Li, Zilang Shi, Guowen Kuang, Pei Nian Liu, Steven G Louie, and Nian Lin. Tuning two-dimensional band structure of Cu(111) surface-state electrons that interplay with artificial supramolecular architectures. *Physical Review B*, 88(24):245430, dec 2013.

[43] Nora González Lacunza. *Study of the geometry and electronic structure of self-assembled monolayers on the au(111) surface*. PhD thesis, UPV/EHU, 2009.

[44] G Kresse and J Hafner. Ab initio molecular dynamics for liquid metals. *Journal of Non-Crystalline Solids*, 156-158(PART 2):956–960, may 1993.

[45] G. Kresse and J. Furthmüller. Efficiency of ab-initio total energy calculations for metals and semiconductors using a plane-wave basis set. *Computational Materials Science*, 6(1):15–50, jul 1996.

[46] G Kresse and J. Furthmüller. Efficient iterative schemes for ab initio total-energy calculations using a plane-wave basis set. *Physical Review B*, 54(16):11169–11186, oct 1996.

[47] Arash A. Mostofi, Jonathan R. Yates, Giovanni Pizzi, Young Su Lee, Ivo Souza, David Vanderbilt, and Nicola Marzari. An updated version of wannier90: A tool for obtaining maximally-localised Wannier functions. *Computer Physics Communications*, 185(8):2309–2310, 2014.

[48] M Born and R J Oppenheimer. On the quantum theory of molecules (English translation). *Annalen der Physik*, 457(1927):1–32, 1927.

[49] P. Hohenberg and W. Kohn. Inhomogeneous electron gas. *Phys. Rev.*, 136:B864–B871, Nov 1964.

[50] W. Kohn and L. J. Sham. Self-consistent equations including exchange and correlation effects. *Physical Review*, 140(4A), 1965.

[51] D. M. Ceperley and B. J. Alder. Ground state of the electron gas by a stochastic method. *Phys. Rev. Lett.*, 45:566–569, Aug 1980.

[52] J. P. Perdew and Alex Zunger. Self-interaction correction to density-functional approximations for many-electron systems. *Physical Review B*, 23(10):5048–5079, 1981.

[53] John P. Perdew, Kieron Burke, and Matthias Ernzerhof. Generalized gradient approximation made simple. *Phys. Rev. Lett.*, 77:3865–3868, Oct 1996.

[54] Elliott H. Lieb and Stephen Oxford. Improved lower bound on the indirect coulomb energy. *International Journal of Quantum Chemistry*, 19(3):427–439, 1981.

[55] B. Hammer, L. B. Hansen, and J. K. Nørskov. Improved adsorption energetics within density-functional theory using revised perdew-burke-ernzerhof functionals. *Phys. Rev. B*, 59:7413–7421, Mar 1999.

[56] M. Dion, H. Rydberg, E. Schröder, D C Langreth, and B I Lundqvist. Van der Waals density functional for general geometries. *Physical Review Letters*, 92(24):22–25, 2004.

[57] Jianmin Tao, John P Perdew, Viktor N. Staroverov, and Gustavo E. Scuseria. Climbing the density functional ladder: Nonempirical meta–generalized gradient approximation designed for molecules and solids. *Physical Review Letters*, 91(14):3–6, 2003.

[58] Stefan Grimme. Semiempirical GGA-Type Density Functional Constructed with a Long-Range Dispersion Correction. *Journal of Computational Chemistry*, 27(15):1787–1799, 2006.

[59] Roberto Peverati and Donald G Truhlar. Quest for a universal density functional: The accuracy of density functionals across a broad spectrum of databases in chemistry and physics, 2014.

[60] Felix Bloch. Über die Quantenmechanik der Elektronen in Kristallgittern. (August):1–46, 2005.

[61] G. Kresse and D. Joubert. From ultrasoft pseudopotentials to the projector augmented-wave method. *Physical Review B*, 59(3):1758–1775, 1999.

[62] D. R. Hamann, M. Schlüter, and C. Chiang. Norm-Conserving Pseudopotentials. *Physical Review Letters*, 43(20):1494–1497, 1979.

[63] N Troullier and Jose Lurs Martins. Efficient pseudopotentials for plane-wave calculations. *Physical Review B*, 43(3):1993, 1991.

[64] Kari Laasonen, Roberto Car, Changyol Lee, and David Vanderbilt. Implementation of ultrasoft pseudopotentials in ab initio molecular dynamics. *Phys. Rev. B*, 43(8):6796–6799, 1991.

[65] P.E. Blöchl. Projector-Augmented Plane-Wave Method. *Physical Review B*, 50(24):17953–17979, 1994.

[66] Gregory H. Wannier. The structure of electronic excitation levels in insulating crystals. *Physical Review*, 52(3):191–197, 1937.

[67] Nicola Marzari and David Vanderbilt. Maximally localized generalized Wannier functions for composite energy bands. *Physical Review B - Condensed Matter and Materials Physics*, 56(20):12847–12865, 1997.

[68] Ivo Souza, Nicola Marzari, and David Vanderbilt. Maximally-localized Wannier functions for entangled energy bands. *Physical Review B*, 65:1–13, 2001.

[69] E. I. Blount. Bloch Electrons in a Magnetic Field. *PHYSICAL REVIEW*, 126(5), 1962.

[70] Arash A. Mostofi, Jonathan R. Yates, Young Su Lee, Ivo Souza, David Vanderbilt, and Nicola Marzari. wannier90: A tool for obtaining maximally-localised Wannier functions. *Computer Physics Communications*, 178(9):685–699, may 2008.

[71] Gianluca Panati and Adriano Pisante. Bloch Bundles, Marzari-Vanderbilt Functional and Maximally Localized Wannier Functions. *Communications in Mathematical Physics*, 322(3):835–875, 2013.

[72] Stephen J. Gustafson and Israel Michael Sigal. *Perturbation Theory: Feshbach-Schur Method*, pages 107–125. Springer Berlin Heidelberg, Berlin, Heidelberg, 2011.

[73] J. E. Lennard-Jones. The electronic structure of some diatomic molecules. *Trans. Faraday Soc.*, 25:668–686, 1929.

[74] J Hubbard and Proc R Soc Lond A. Electron correlations in narrow energy bands. *Proceedings of the Royal Society of London. Series A. Mathematical and Physical Sciences*, 276(1365):238–257, nov 1963.

[75] J Hubbard and Proc R Soc Lond A. Electron correlations in narrow energy bands. II. The degenerate band case. *Proceedings of the Royal Society of London. Series A. Mathematical and Physical Sciences*, 277(1369):237–259, jan 1964.

[76] J Hubbard and Proc R Soc Lond A. Electron correlations in narrow energy bands III. An improved solution. *Proceedings of the Royal Society of London. Series A. Mathematical and Physical Sciences*, 281(1386):401–419, sep 1964.

[77] J Hubbard and Proc R Soc Lond A. Electron correlations in narrow energy bands - IV. The atomic representation. *Proceedings of the Royal Society of London. Series A. Mathematical and Physical Sciences*, 285(1403):542–560, may 1965.

[78] J Hubbard and Proc R Soc Lond A. Electron correlations in narrow energy bands V. A perturbation expansion about the atomic limit. *Proceedings of the Royal Society of London. Series A. Mathematical and Physical Sciences*, 296(1444):82–99, jan 1967.

[79] J Hubbard and Proc R Soc Lond A. Electron correlations in narrow energy bands VI. The connexion with many-body perturbation theory. *Proceedings of the Royal Society of London. Series A. Mathematical and Physical Sciences*, 296(1444):100–112, jan 1967.

[80] Willi Auwärter. Hexagonal boron nitride monolayers on metal supports: Versatile templates for atoms, molecules and nanostructures. *Surface Science Reports*, 2018.

[81] Lu Hua Li and Ying Chen. Atomically Thin Boron Nitride: Unique Properties and Applications. *Advanced Functional Materials*, 26(16):2594–2608, apr 2016.

[82] Kenji Watanabe, Takashi Taniguchi, and Hisao Kanda. Direct-bandgap properties and evidence for ultraviolet lasing of hexagonal boron nitride single crystal. *Nature Materials*, 3(6):404–409, 2004.

[83] G. Cassabois, P. Valvin, and B. Gil. Hexagonal boron nitride is an indirect bandgap semiconductor. *Nature Photonics*, 10(4):262–266, 2016.

[84] X Blase, Angel Rubio, Steven G Louie, and Marvin L Cohen. Quasiparticle band structure of bulk hexagonal boron nitride and related systems. *Physical Review B*, 51(11):6868–6875, mar 1995.

[85] A. Bhattacharya, S. Bhattacharya, and G. P. Das. Band gap engineering by functionalization of BN sheet. *Physical Review B*, 85(3):035415, jan 2012.

[86] M. Corso, W. Auwärter, M. Muntwiler, A. Tamai, T Greber, and J Osterwalder. Boron Nitride Nanomesh. *Science*, 303(5655):217–220, jan 2004.

[87] Yun Peng Wang and Hai Ping Cheng. First-principles simulations of a graphene-based field-effect transistor. *Physical Review B - Condensed Matter and Materials Physics*, 91(24):1–6, 2015.

[88] Oleg V. Yazyev and Alfredo Pasquarello. Metal adatoms on graphene and hexagonal boron nitride: Towards rational design of self-assembly templates. *Phys. Rev. B*, 82:045407, Jul 2010.

[89] A. Abragam and B. Bleaney. *Electron Paramagnetic Resonance of Transition Ions*. 1970.

[90] M. Etzkorn, C. F. Hirjibehedin, A. Lehnert, S. Ouazi, S. Rusponi, S. Stepanow, P. Gambardella, C. Tieg, P. Thakur, A. I. Lichtenstein, A. B. Shick, S. Loth, A. J. Heinrich, and H. Brune. Comparing XMCD and DFT with STM spin excitation spectroscopy for Fe and Co adatoms on Cu2 N/Cu(100). *Physical Review B - Condensed Matter and Materials Physics*, 92(18):184406, 2015.

[91] Matthias Muenks, Peter Jacobson, Markus Ternes, and Klaus Kern. Correlation-driven transport asymmetries through coupled spins in a tunnel junction. *Nature Communications*, 8(1):14119, apr 2017.

[92] L Camilli, E. Sutter, and P Sutter. Growth of two-dimensional materials on non-catalytic substrates: H-BN/Au(111). *2D Materials*, 1(2):025003, aug 2014.

[93] Robert Laskowski, Peter Blaha, and Karlheinz Schwarz. Bonding of hexagonal BN to transition metal surfaces: An ab initio density-functional theory study. *Physical Review B*, 78(4):045409, jul 2008.

[94] Milan P Allan, Simon Berner, Martina Corso, Thomas Greber, and Jürg Osterwalder. Tunable self-assembly of one-dimensional nanostructures with orthogonal directions. *Nanoscale Research Letters*, 2(2):94–99, feb 2007.

[95] Yue Qi, Zhepeng Zhang, Bing Deng, Xiebo Zhou, Qiucheng Li, Min Hong, Yuanchang Li, Zhongfan Liu, and Yanfeng Zhang. Irreparable Defects Produced by the Patching of h-BN Frontiers on Strongly Interacting Re(0001) and Their Electronic Properties. *Journal of the American Chemical Society*, 139(16):5849–5856, apr 2017.

[96] Fabian Schulz, Robert Drost, Sampsa K. Hämäläinen, Thomas Demonchaux, Ari P. Seitsonen, and Peter Liljeroth. Epitaxial hexagonal boron nitride on Ir(111): A work function template. *Physical Review B - Condensed Matter and Materials Physics*, 89(23):235429, 2014.

[97] Andrii Goriachko, Yunbin He, Marcus Knapp, Herbert Over, Martina Corso, Thomas Brugger, Simon Berner, Juerg Osterwalder, and Thomas Greber. Self-assembly of a hexagonal boron nitride nanomesh on Ru(0001). *Langmuir*, 23(6):2928–2931, 2007.

[98] Eli Stavitski and Frank M.F. de Groot. The CTM4XAS program for EELS and XAS spectral shape analysis of transition metal L edges. *Micron*, 41(7):687–694, oct 2010.

[99] A Uldry, F Vernay, and B Delley. Systematic computation of crystal-field multiplets for x-ray core spectroscopies. *Physical Review B*, 85(12):125133, mar 2012.

[100] Iker Gallardo, Andres Arnau, Fernando Delgado, Romana Baltic, Aparajita Singha, Fabio Donati, Christian Wäckerlin, Jan Dreiser, Stefano Rusponi, and Harald Brune. Large effect of metal substrate on magnetic anisotropy of Co on hexagonal boron nitride. *New Journal of Physics*, 21(7):073053, jul 2019.

[101] Frank de Groot. High-Resolution X-ray Emission and X-ray Absorption Spectroscopy. *Chemical Reviews*, 101(6):1779–1808, jun 2001.

[102] Cinthia Piamonteze, Uwe Flechsig, Stefano Rusponi, Jan Dreiser, Jakoba Heidler, Marcus Schmidt, Reto Wetter, Marco Calvi, Thomas Schmidt, Helena Pruchova, Juraj Krempasky, Christoph Quitmann, Harald Brune, and Frithjof Nolting. Synchrotron Radiation X-Treme beamline at SLS: X-ray magnetic circular and linear dichroism at high field and low temperature. 19:661–674, 2012.

[103] P Gambardella, S S Dhesi, S Gardonio, C Grazioli, C Carbone, and P Ohresser. Localized Magnetic States of Fe, Co, and Ni Impurities on Alkali Metal Films. *Physical Review Letters*, 88(4):4, jan 2002.

[104] Giulia Avvisati, Pierluigi Gargiani, Pierluigi Mondelli, Francesco Presel, Luca Bignardi, Alessandro Baraldi, and Maria Grazia Betti. Metal phthalocyanines interaction with Co mediated by a moiré graphene superlattice. *Journal of Chemical Physics*, 150(5):054704, feb 2019.

[105] Joachim Stöhr and Hans Christoph Siegmann. *Magnetism*, volume 152. Springer Berlin Heidelberg, Berlin, Heidelberg, 2006.

[106] Patrick Bruno. Tight-binding approach to the orbital magnetic moment and magneto crystalline anisotropy. *Physical Review B*, 39(1):865, 1989.

[107] Gerrit van der Laan. Microscopic origin of magnetocrystalline anisotropy in transition metal thin films. *Journal of Physics: Condensed Matter*, 10(14):3239–3253, apr 1998.

[108] B Wortmann, D. van Vörden, P Graf, R Robles, P Abufager, N Lorente, C A Bobisch, and R. Möller. Reversible 2D Phase Transition Driven By an Electric Field: Visualization and Control on the Atomic Scale. *Nano Letters*, 16(1):528–533, jan 2016.

[109] Ignacio Piquero-zulaica, Jun Li, Zakaria M Abd El-fattah, Leonid Solianyk, Iker Gallardo, Leticia Monjas, Anna K H Hirsch, Andres Arnau, J Enrique Ortega, and Meike St. Tunable energy and mass renormalization from homothetic Quantum dot arrays. *Submitted*, pages 1–6, 2019.

[110] F. Klappenberger, D. Kühne, W. Krenner, I. Silanes, A. Arnau, F. J. García De Abajo, S. Klyatskaya, M. Ruben, and J. V. Barth. Tunable quantum dot arrays formed from self-assembled metal-organic networks. *Physical Review Letters*, 106(2):1–4, 2011.

[111] E. Bertel and N. Memmel. Promotors, poisons and surfactants: Electronic effects of surface doping on metals. *Applied Physics A: Materials Science and Processing*, 63(6):523–531, 1996.

[112] F. Forster, A. Bendounan, J. Ziroff, and F. Reinert. Systematic studies on surface modifications by ARUPS on Shockley-type surface states. *Surface Science*, 600(18):3870–3874, 2006.

[113] Miguel Ruiz-Osés, Dimas G. de Oteyza, Isabel Fernández-Torrente, Nora Gonzalez-Lakunza, Phillipp M. Schmidt-Weber, Thorsten Kampen, Karsten Horn, André Gourdon, Andrés Arnau, and J. Enrique Ortega. Non-Covalent Interactions in Supramolecular Assemblies Investigated with Electron Spectroscopies. *ChemPhysChem*, 10(6):896–900, 2009.

[114] Yan Ling Zhao, Weihua Wang, Fei Qi, Jian Fu Li, Guowen Kuang, Rui Qin Zhang, Nian Lin, and Michel A. Van Hove. Donor/acceptor properties of aromatic molecules in complex metal-molecule interfaces. *Langmuir*, 33(2):451–458, 2017.

[115] Qiang Sun, Liangliang Cai, Honghong Ma, Chunxue Yuan, and Wei Xu. Dehalogenative Homocoupling of Terminal Alkynyl Bromides on Au(111): Incorporation of Acetylenic Scaffolding into Surface Nanostructures. *ACS Nano*, 10(7):7023–7030, 2016.

[116] Ignacio Piquero-Zulaica, Zakaria Mohammed Abd El-Fattah, Olha Popova, Shigeki Kawai, Sylwia Nowakowska, Manfred Matena, Mihaela Enache, Meike Stöhr, Antonio Tejeda, Armina Taleb-Ibrahimi, Ernst Meyer, J Enrique Ortega, Lutz H Gade, Thomas A Jung, and Jorge Lobo-Checa. Effective determination of surface potential landscapes from metal-organic nanoporous network overlayers. *New Journal of Physics*, apr 2019.

[117] Sylwia Nowakowska, Aneliia Wäckerlin, Ignacio Piquero-Zulaica, Jan Nowakowski, Shigeki Kawai, Christian Wäckerlin, Manfred Matena, Thomas Nijs, Shadi Fatayer, Olha Popova, Aisha Ahsan, S. Fatemeh Mousavi, Toni Ivas, Ernst Meyer, Meike Stöhr, J. Enrique Ortega, Jonas Björk, Lutz H. Gade, Jorge Lobo-Checa, and Thomas A. Jung. Configuring electronic states in an atomically precise array of quantum boxes. *Small*, 12(28):3757–3763, 2016.